

THESIS

METHOD FOR CREATING FUNCTIONALLY GRADED MATERIALS WITH SPARK
PLASMA SINTERING AND A CONTINUOUS MACHINE FOR FUTURE SCALABILITY

Submitted by

Paul S. Colasuonno

Department of Mechanical Engineering

In partial fulfillment of the requirements

For the Degree of Master of Science

Colorado State University

Fort Collins, Colorado

Fall 2017

Master's Committee:

Advisor: Susan James

Kaka Ma

James Nielson

Copyright by Paul S. Colasuonno 2017

All Rights Reserved

ABSTRACT

METHOD FOR CREATING FUNCTIONALLY GRADED MATERIALS WITH SPARK PLASMA SINTERING AND A CONTINUOUS MACHINE FOR FUTURE SCALABILITY

This work develops a quantitative process to sinter functionally graded materials (FGMs) to specific porosity gradients using Spark Plasma Sintering (SPS). The powder densification in SPS is modeled using the Master Sintering Curve (MSC) calculated from shrinkage due to three different heating rates. The meaning of the apparent sintering activation energy, Q_{MSC} , is discussed along with the MSC's applicability to SPS. The MSC is adjusted for the additional sintering that occurs during cooling, such that porous materials can be produced by interrupting the heating schedule. The temperature in the powder is then spatially resolved by a constructed thermal-electric FEA model. Tooling is designed to apply a steady state temperature gradient ($50^{\circ}C/mm$) on zirconia (+3% mol yttria) powder. The MSC, coupled to the thermal-electric model, is used to spatially predict densification in a temperature gradient. Resulting FGM microstructures and grain size distributions are discussed.

Design problems found while attempting to scale the FGMs process to larger diameters are quantified. As an alternative to traditional SPS batch processes, a Continuous Electric Field Assisted Sintering (CEFAS) machine is developed to address these practical limitations from a new direction. The proof of concept CEFAS machine uses Joule heated rollers to continuously heat, compress, and extrude material under conditions analogous to SPS. Design considerations, lessons learned, and control variables for future iteration CEFAS machines are illustrated.

ACKNOWLEDGEMENTS

Initially the aim of this project as defined by Dr. Troy Holland was to develop a method, using a standard SPS machine, to sinter large diameter tiles in a temperature gradient such that the hot side would reach 100% density and the cold side would maintain open porosity. The key issue in this design problem was to increase the sample diameter while maintaining a constant radial temperature. Along side lab member Corson Cramer, careful powder densification measurements were collected for calculations.

The enormous task of grain size analysis would not have been possible if not for the huge effort from Corson and many undergraduate volunteers who gave hundreds of hours working over polishing wheels and computer screens. We also really appreciate the helpfulness and friendliness of the CIF staff.

During the development of large diameter SPS tooling we found diminished returns from exponentially more complicated tooling. Dr. Holland pitched the idea of a continuous EFAS machine consisting of Joule heated graphite hot rollers. Derek Young and myself worked over the summer of 2016 to design and manufacture the device using as little resources as possible, often reclaiming scrap metal buried outside the facility. Many thanks to him for his assistance during the long days and nights in the machine shop. Images of the design iteration can be seen in appendix C.

Special thanks to Dr. Susan James who recently stepped in as my advisor and helped me complete this thesis. And finally, thanks to my family and friends for standing by me during this process!

TABLE OF CONTENTS

ABSTRACT	ii
ACKNOWLEDGEMENTS	iii
LIST OF FIGURES	v
LIST OF SYMBOLS	vi
LIST OF ACRONYMS	vii
Chapter 1 Background Information	1
1.1 Sintering	1
1.1.1 General diffusion	2
1.1.2 Diffusion mechanisms in sintering	3
1.2 Master Sintering Curve	8
1.3 Spark Plasma Sintering	12
Chapter 2 Modeling the SPS process	17
2.1 Thermal modeling	17
2.2 Densification modeling	19
2.2.1 Master sintering curve	21
2.2.2 Sources of error in the MSC calculation	23
2.3 Conclusions and Future Work	33
Chapter 3 Manufacturing Functionally graded materials with SPS	35
3.1 Methods	35
3.1.1 Isothermal samples	36
3.1.2 Temperature measurement	36
3.1.3 SPS tooling for controllable thermal gradients	39
3.1.4 SEM procedure and grain size analysis	42
3.2 Results and Discussion	43
3.3 Conclusions and Future work	48
Chapter 4 Scalability of the EFAS process	49
4.1 Scaling up standard SPS tooling	49
4.1.1 Joule heating in large conductors	49
4.1.2 Methods to improve temperature homogeneity	54
4.2 Continuous EFAS machine	59
4.2.1 CEFAS machine design details	61
4.2.2 Critical components	67
4.3 Conclusion and future improvements	70
Bibliography	72
Appendix A Master sintering curve MATLAB script	78

Appendix B	Thermocouple measurement	86
Appendix C	CEFAS design	90
C.1	CEFAS thermal modeling	90
C.2	CEFAS design iterations	92

LIST OF FIGURES

1.1	Sintering of a two particle system	1
1.2	Diffusion pathways in two particle system	4
1.3	Stages of sintering	5
1.4	Characteristic microstructure coarsening from surface diffusion during stage I sintering	6
1.5	Facets on the surface of an Al_2O_3 grain after free sintering in air.	6
1.6	Master Sintering Curve	10
1.7	Pressure assisted master sintering surface	11
1.8	Cross section of typical SPS tooling graphite stack	13
1.9	Temperature distribution in standard SPS die under nominal conditions	14
1.10	SPS grain size relative to sample without an applied electric field	15
2.1	Thermal expansion background subtraction	20
2.2	MSC activation energy error minimization	22
2.3	The Master Sintering Curve	22
2.4	Densification versus time overlaid on MSC density model	23
2.5	Normalized difference error between curves at each density	24
2.6	MRS for MSC calculated with different density ranges	25
2.7	Interrupted Heating schedule with predicted cooling	27
2.8	MSC densification curve adjusted for cooling	29
2.9	Densification curves with interruption MSC prediction	30
2.10	Measured temperature compared to generated temperature	31
2.11	MSC density prediction with two similar heating schedules	32
2.12	Change in MSC density prediction with $Q_{MSC} \pm 5kJ/mol$	33
3.1	Welded type-C thermocouple	37
3.2	Type-C thermocouple voltage versus temperature	38
3.3	Research sized axial thermal gradient tooling	40
3.4	Current density inside SOD tooling	41
3.5	SOD punch height dimension	41
3.6	Photo of SOD punch during sintering	42
3.7	Temperature gradient versus SOD height	42
3.8	Three circle method used to calculate grain size	43
3.9	FGM cross section prepared for SEM grain size analysis	44
3.10	SOD punch current density and temperature model	44
3.11	Temperature and heating rate of five points inside the FGM during sintering	45
3.12	The MSC model of densification in a temperature gradient	46
3.13	SEM micrographs of FGM sintered at 31.8 MPa	47
3.14	SEM micrographs of FGM sintered at 63.6 MPa	47
3.15	Grain size distribution in FGM	47
4.1	Joule heating versus cross sectional area drawing	50

4.2	Joule heating versus cross sectional area average temperature plot	51
4.3	Joule heating versus cross sectional area temperature distribution	52
4.4	Example of non-radially symmetric tooling	53
4.5	Temperature distribution on square sample	54
4.6	High aspect ratio SPS die	56
4.7	SPS die radiation insulation	57
4.8	Large diameter SPS tooling	57
4.9	COMSOL model of large sample and without radiation shielding	58
4.10	CEFAS assembled on table top	59
4.11	Powder pellet heated by the CEFAS machine	60
4.12	Final CAD model of the CEFAS machine	60
4.13	CEFAS roller cross section	62
4.14	Assembled top roller	64
4.15	Assembled bottom roller	65
4.16	Current pathway in SPS graphite	66
4.17	Current pathway in CEFAS graphite	66
4.18	CEFAS roller wheel	68
4.19	SPS tooling for CEFAS wheel	69
B.1	SOD punch thermocouple placement options	87
B.2	Radial thermocouple drill jig	88
B.3	Radial thermocouple hole temperature effect	88
B.4	SPS vacuum chamber	89
C.1	CEFAS simplified CAD isometric view	91
C.2	simplified CAD model used for CEFAS thermal analysis	91
C.3	CEFAS design v.1.II from June 6, 2016	92
C.4	CEFAS design v.1.III from June 12, 2016	92
C.5	CEFAS design v.2 from June 14, 2016	93
C.6	CEFAS design v.5 from June 28, 2016	93
C.7	CEFAS design v.8 from July 13, 2016	94
C.8	CEFAS design v.9 from July 13, 2016	94
C.9	CEFAS design v.10 from July 18, 2016	95
C.10	CEFAS design v.16 from August 17, 2016	95
C.11	CEFAS design v.21 from November 17, 2016	96
C.12	CEFAS design v.25 from December 27, 2016	97

LIST OF SYMBOLS

φ	Concentration
J	Flux, rate of flow per unit area
D	Diffusion rate
D_o	Diffusion coefficient
Q	Activation energy in units of kJ/mol
R	Gas constant in units of $JK^{-1}mol^{-1}$
σ	Surface stress due to particle curvature
γ	Surface free energy
SD	Surface diffusion
VD	Volume diffusion
GD	Grain boundary diffusion
k	Boltzmann constant in units of JK^{-1}
ρ	relative density [%]
ρ_g	Relative density of powder prior to sintering (green)
ρ_f	Relative density of powder after sintering
Ω	Atomic volume
Γ	Scaling coefficient associated with geometry [1]
G	average grain diameter
Q_{MSC}	Apparent sintering activation energy
$\Theta(t, T)$	Temperature and time integral of Master Sintering Curve
$\phi(\rho)$	Sintering stress intensification factor due to uniaxial loading
p_a	Pressure due to uniaxial applied load
$K_{p,I,d}$	PID control loop equation coefficients
$disp_i$	instantaneous displacement recorded by SPS machine
Q_{conv}	Heat transferred per unit time due to convection
h	Heat transfer coefficient from flowing cooling water to steel electrode
Q_{rad}	Heat transferred per unit time due to radiation
ϵ	Emissivity of a material
ς	Stefan-Boltzmann constant
c_p	Heat capacity of a material
k	Thermal conductivity of a material
\vec{J}	Vector field of current density within a conductor
κ	electrical conductivity

LIST OF ACRONYMS

3YTZ	3% mol yttria-stabilized zirconia
CAD	Computer Aided Design
CEFAS	Continuous Electric Field Assisted Sintering
CIF	Central Instruments Facility
CJC	Cold Junction Compensator
EFAS	Electric Field Assisted Sintering
FGM	Functionally Graded Material
ID	Inner Diameter
OD	Outer Diameter
PID	Proportion-Integral-Derivative feedback controller
MSC	Master Sintering Curve
MRS	Mean Residual Square in context of MSC
SEM	Scanning Electron Microscope
SOD	Simulated Offset Distance punch
SPS	Spark Plasma Sintering

Chapter 1

Background Information

The densification of particles to strengthen a conglomerate by heating has been done for thousands of years to produce pottery and bricks. Sintering is the process of transforming a powder into a solid body using heat. Solid state diffusion allows materials with very high melting temperatures to reach a full density below their melting point and retain small grain sizes. The application of sintered parts to modern engineering practices and problems allows the field to advance. Research and development of sintering processes aim to produce materials faster, more controllably, and with superior properties.

1.1 Sintering

A simple illustration of the sintering process is shown in figure 1.1 where two initially spherical particles move together and become one volume:

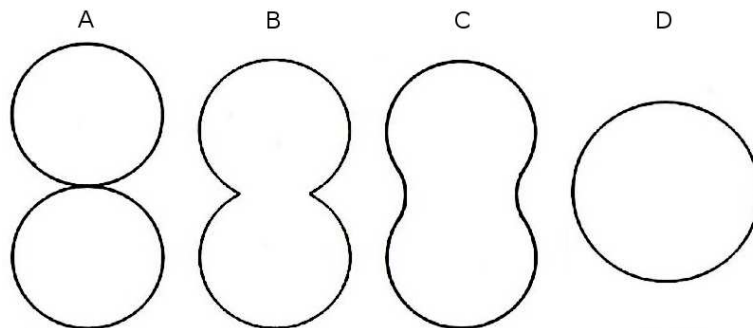


Figure 1.1: Sintering in a two particle system. A) Initial loose powder, very small neck between particles B) early stages of neck formation C) intermediate stage of neck formation D) Fully sintered particle [2]

The solid state diffusion of atoms brings the particle centers closer together. In a large array of particles, the surface area is reduced along with the volume of pores.

1.1.1 General diffusion

The diffusion equation can be derived from conservation of mass. The change in concentration φ with time is equal to the flux of material, J , flowing in and out of that volume:

$$\frac{\partial \varphi}{\partial t} = \nabla \cdot J \quad (1.1)$$

Fick's first law models the natural flux of a species due to a variable concentration. The magnitude of the flux is linearly proportional to the concentration gradient and is scaled by the diffusion rate D :

$$J = -D\nabla\varphi \quad (1.2)$$

Combining these two equations leads to the general diffusion equation:

$$\frac{\partial \varphi}{\partial t} = \nabla \cdot [-D\nabla\varphi] \quad (1.3)$$

In one dimension:

$$\frac{d\varphi}{dt} = -D \frac{d^2\varphi}{dx^2} \quad (1.4)$$

The diffusion coefficient is a function of temperature and can be modeled by the Arrhenius equation:

$$D = D_o \exp\left(-\frac{Q}{RT}\right) \quad (1.5)$$

Where D_o is a coefficient, Q is the activation energy, and R is the gas constant.

1.1.2 Diffusion mechanisms in sintering

Powders are inherently in an unstable state. Generally, the reduction of surface free energy (by eliminating pores) provides the driving force for densification. All surfaces have a free energy associated with their radius of curvature. The equilibrium condition for a particle is given by the energy balance:

$$\sigma dV + \gamma dA = 0 \quad (1.6)$$

where σ is the surface stress due to the curvature and γ is the surface energy. Assuming the particle is a sphere, the differentials dA and dV in terms of the radius r of the sphere are:

$$dA = 8\pi r dr \quad (1.7)$$

$$dV = 4\pi r^2 dr$$

combining these equations:

$$\sigma = \gamma \frac{8\pi r dr}{4\pi r^2 dr} = \gamma \frac{2}{r} \quad (1.8)$$

And the principal curvatures r_1 and r_2 that define a 3D surface:

$$\sigma = \gamma \left(\frac{1}{r_1} + \frac{1}{r_2} \right) \quad (1.9)$$

When the powder is heated to high temperatures, the system is allowed significant atomic motion. Mass is rearranged in order to reduce the free surface energy due to this curvature.

Mass transport pathways are shown in figure 1.2 and table 1.1

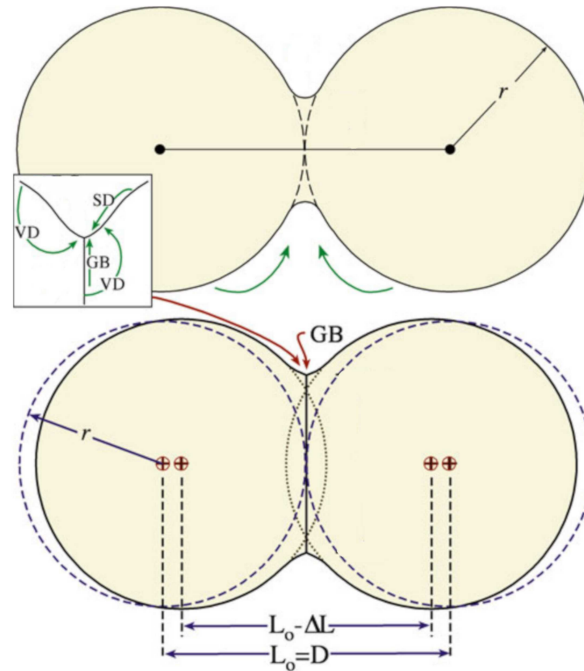


Figure 1.2: Sintering of two sphere model showing mass diffusion pathways to the neck leading to densification [3]

Table 1.1: Diffusion pathways during sintering leading to densification

<i>Mechanism</i>	<i>Transport path</i>	<i>Source</i>
SD	Surface diffusion	Surface
VD	Volume diffusion	Surface
GD	Grain boundary diffusion	Grain boundary
VD	Volume diffusion	Grain boundary

Sintering shrinkage appears as a sigmoidal curve that can be broken up into three density ranges, ρ , each associated with a specific microstructure. The densification curves shown in figure 2.4 illustrates typical behavior.

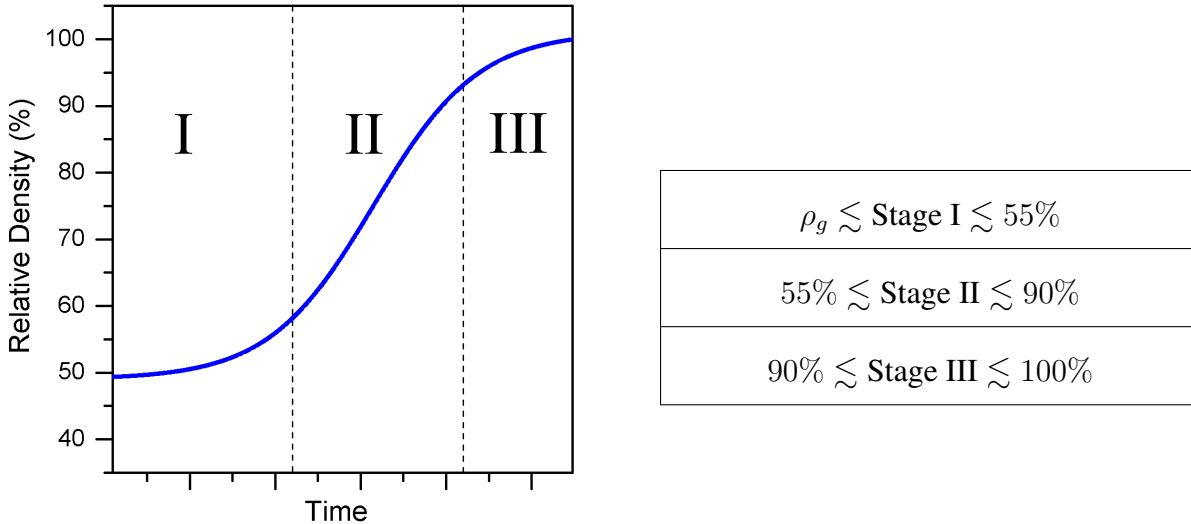


Figure 1.3: The stages of sintering. Stage II is roughly defined as the linear section of the sigmoidal densification curve.

Surface diffusion

Stage I sintering is characterized by rapid growth of inter-particle necks. The macroscopic shrinkage of the sample during stage I is negligible. Surface diffusion is the primary mass transport mechanism at low temperatures [4]. Microstructures held at stage I temperatures long enough will coarsen as shown in figure 1.4. The curvature in the powder body is reduced without densification. Surface diffusion (as well as evaporation-condensation) therefore competes against densifying mechanisms to reduce the surface free energy due to curvature.

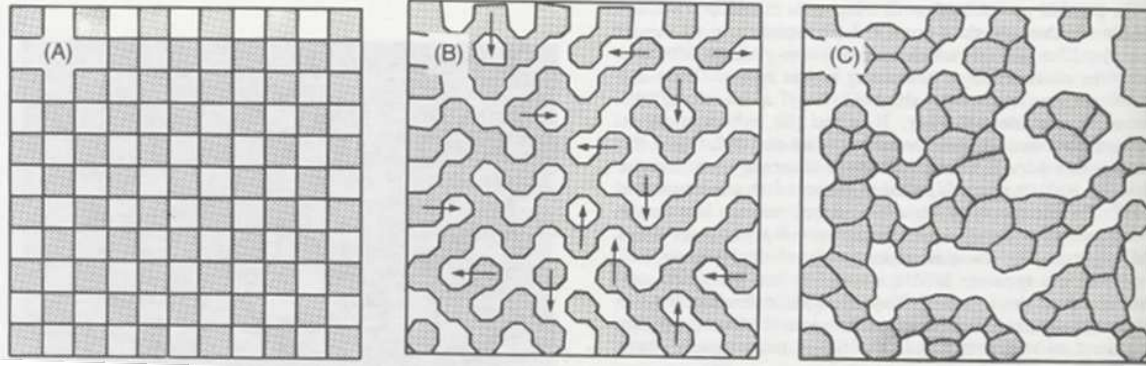


Figure 1.4: Reduction of surface curvature in a microstructure coarsening due to surface diffusion [5]

The crystalline nature of materials can often be seen by the formation of facets on the grain surface. Figure 1.5 shows facets on an Al_2O_3 grain after extended time spent at stage I temperatures.

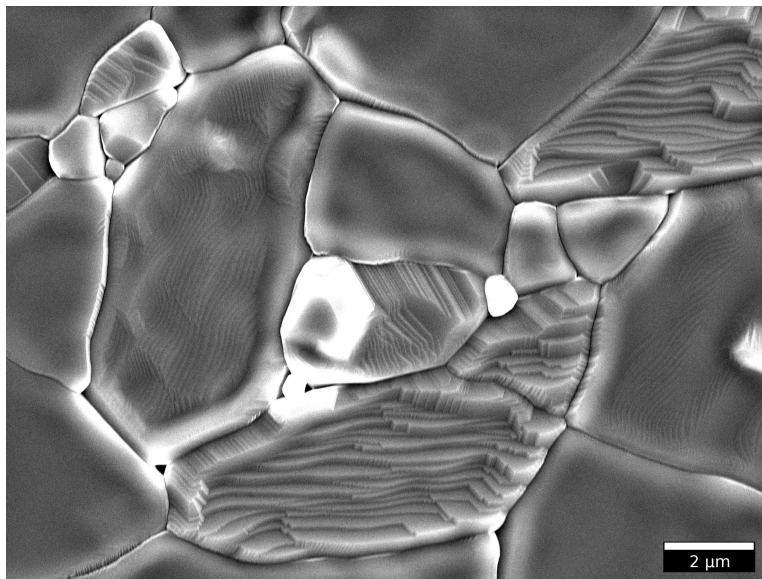


Figure 1.5: Facets on the surface of an Al_2O_3 grain after free sintering in air.

Volume diffusion

Stage II sintering is characterized by the middle (linear) section of the sigmoidal densification curve. Volume diffusion and grain boundary diffusion are primarily responsible for this densification.

Volume diffusion involves the motion of vacancies through the volume of the particle. The equilibrium concentration of vacancies increases with temperature. There are three main vacancy diffusion pathways through the volume of the grain that contribute to sintering. The vacancy flow (and atomic flow in the opposite direction) involves free surfaces, grain boundaries and dislocations.

Vacancies created on the neck surface at grain boundary move through the bulk volume then annihilate on the free surface. This is effectively surface transportation and does not contribute to densification.

Vacancies created on the neck surface move to and annihilate on the grain boundary. This deposits atoms on the grain boundary and allows the neck to grow, bringing the particle centers closer together [3]. Reference figure 1.2 to visualize the pathways atoms take due to this motion, note that vacancy motion is opposite the arrows in the figure. In materials that are compressed prior to densification (as in SPS and hot pressing) the dislocations due to plastic deformation can significantly contribute to densification early during sintering. The dislocations move to annihilate on the neck surface and densification occurs because the vacancy source is not a surface.

Grain boundary diffusion

Mass flows along the grain boundary and is redeposited at the neck surface. The atoms brought to neck surface are then redistributed around the particles by surface diffusion. Grain boundaries

form between the individual particles due to misaligned crystal structures. As the surface curvature is reduced at higher densities, grain boundary equilibrium becomes important.

Combined stage sintering model

Researchers Hansen, et al., developed the "combined stage-sintering model" which equates the measured densification to the contribution of volume and grain boundary diffusion [1]:

$$-\frac{1}{L} \frac{dL}{dt} = \frac{\gamma\Omega}{kT} \left(\frac{\Gamma_V D_V}{G^3} + \frac{\Gamma_B D_B}{G^4} \right) \quad (1.10)$$

Where the normalized instantaneous linear shrinkage, $\frac{1}{L} \frac{dL}{dt}$, is proportional to the grain size G of the particles, D_V , D_B are the diffusion rates, Γ_V , Γ_B are geometric scaling terms associated with volume and grain boundary diffusion respectively. Ω is the atomic volume, k is the Boltzmann constant.

For isotropic shrinkage, the linear shrinkage rate can be converted to densification by:

$$-\frac{1}{L} \frac{dL}{dt} = \frac{d\rho}{3\rho dt} \quad (1.11)$$

1.2 Master Sintering Curve

Combing the diffusion terms, D_V and D_B , in equation 1.10 to a single Arrhenius equation, the densification rate becomes:

$$\frac{d\rho}{3\rho dt} = \frac{\gamma\Omega \Gamma(\rho) D_o}{kT G(\rho)^n} \exp\left(-\frac{Q_{MSC}}{RT}\right) \quad (1.12)$$

With this assumption, the densification occurs due a single transport mechanism associated with an activation energy Q_{MSC} which is defined as the *apparent sintering activation energy*. The exponent n is associated with either volume or grain boundary diffusion. This assumes that G and λ are only functions of density. Equation 1.12 can be rearranged and integrated:

$$\int_0^t \frac{1}{T} \exp\left(-\frac{Q_{MSC}}{RT}\right) dt = \frac{k}{\gamma\Omega D_0} \int_{\rho_0}^{\rho} \frac{G(\rho)^n}{3\rho\Gamma(\rho)} d\rho \quad (1.13)$$

The right hand side of this equation includes all of the mass transport processes produced by the sintering environment. The left hand side is an easily computed integral of the heating schedule:

$$\Theta(t, T) \equiv \int_0^t \frac{1}{T} \exp\left(-\frac{Q_{MSC}}{RT}\right) dt \quad (1.14)$$

If a specific powder is sintered with several different heating schedules and the dominate mass transport mechanism remains constant, then the plot of each densification pathway and $\Theta(t, T)$ resolve to a single locus defined as the Master Sintering Curve (MSC) shown in figure 1.6 [6]. The MSC derivation assumes a single dominate densification mechanism and pressureless isotropic shrinkage.

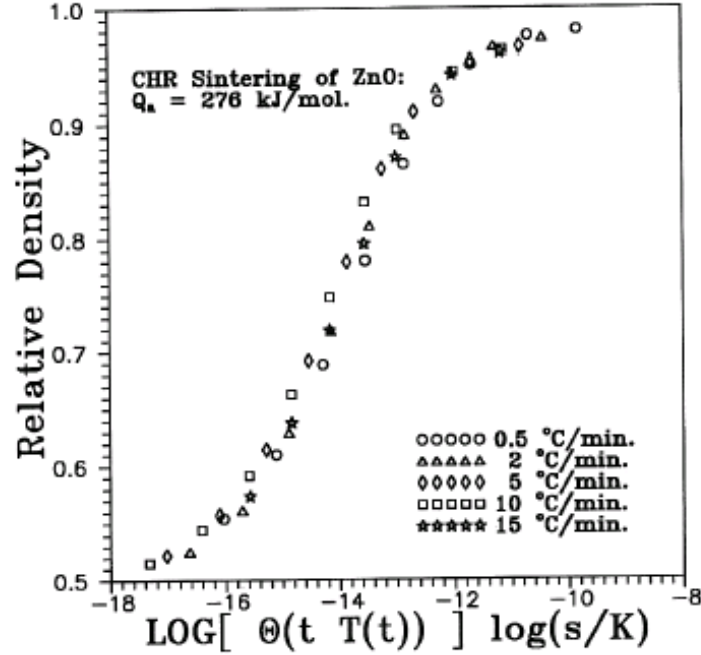


Figure 1.6: The Master Sintering Curve from five different thermal schedules [6]

Literature typically calculates the MSC using the shrinkage measured in $50\% < \rho < 90\%$. In a brute force calculation, the $\Theta(t, T)$ term is calculated for each heating schedule over a range of possible Q_{MSC} . The difference between the $\Theta(T(t))$ term at each density is summed and defined as *MRS*, Mean Residual Square:

$$MRS = \sqrt{\frac{1}{\rho_f - \rho_g} \int_{\rho_g}^{\rho_f} \frac{\sum_{i=1}^N (\Theta_i / \Theta_{avg} - 1)^2}{N} d\rho} \quad (1.15)$$

Where N is the number of heating schedules, Θ_i / Θ_{avg} is the ratio of that single heating schedule Θ to the average value of all Θ at that density.

The MRS minimum is shown graphically in figure 2.2 where Q_{MSC} produces the lowest *MRS*. This method is widely used in the literature as a useful tool to easily develop densification models from experimental data.

MSC with applied loads

While the MSC method was derived using equations of grain boundary and volume diffusion, ignoring plastic flow densification mechanisms, researchers showed that MSC method remains applicable in pressure assisted densification [7]. They sintered alumina using five different heating schedules at five different applied loads. They created a pressure-assisted master sintering surface which allowed them to predict density to 1% accuracy shown in figure 1.7.

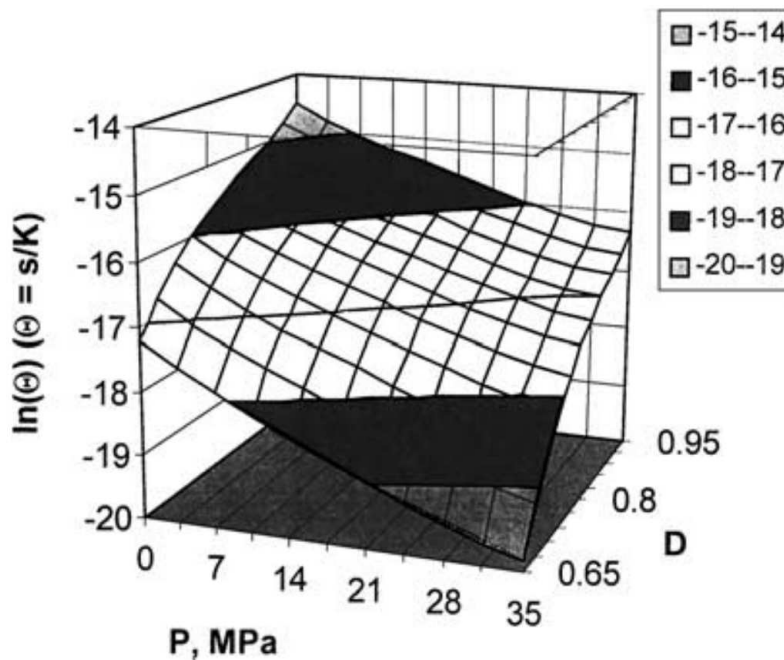


Figure 1.7: The pressure-assisted master sintering surface developed from five thermal schedules at a range of pressures applied pressured [7]

Guillon and Langer showed how equation 1.12 can be modified to include an applied pressure. They then used the pressure assisted MSC method to successfully model densification with an electric field [8].

The applied load can be larger than the sintering stress but not large enough to activate excessive plasticity. This means the dominant densification mechanism is a diffusional process. Volume

diffusion processes may increase the shrinkage rate because of an increased number of dislocations forming in the the volume of the particle. The dislocations form vacancies that diffuses to the grain boundary which causes shrinkage. The axial strain rate is then:

$$\frac{d\rho}{3\rho dt} = \frac{\gamma\Omega}{kT} \frac{\Gamma(\rho)D_o}{G(\rho)^n} \exp\left(-\frac{Q_{MSC}}{RT}\right) [\phi(\rho)p_a]^m \quad (1.16)$$

The terms in the square brackets include the effect of added pressure where ϕ is the stress intensification factor as function of density, p_a is the applied load, and m is a diffusion exponent (m=1) for grain boundary and volume diffusion. This equation is rearranged as before to:

$$\int_0^t \frac{1}{T} \exp\left(-\frac{Q_{MSC}}{RT}\right) dt = \frac{k}{3\gamma\Omega D_o p_a^m} \int_{\rho_0}^{\rho} \frac{G(\rho)^n}{\rho\Gamma(\rho)\phi(\rho)^m} d\rho \quad (1.17)$$

This pressure assisted MSC equation has the same $\Theta(t, T)$ term as before and is used in the same way. Their calculated MSC model used heating rates 35, 50, 100, 150 *K/min* on alumina with 50 MPa applied load. Their model was within 1% of a 75*K/min* heating rate sintered in the same way.

1.3 Spark Plasma Sintering

Spark Plasma Sintering (SPS) or Electric Field Assisted Sintering (EFAS) is a technique where powders are compressed by a uniaxial load inside resistively heated graphite tooling. The discharge of an electric current through the graphite allows very fast heating schedules compared to conventional hot-pressing or free sintering. Less time spent at low temperatures can reduce microstructural coarsening [9] and the applied electric field can lower the energy required for mass

transport [10]. A typical research size (20 mm diameter punch and die) SPS graphite tooling stack is shown in figure 1.8.

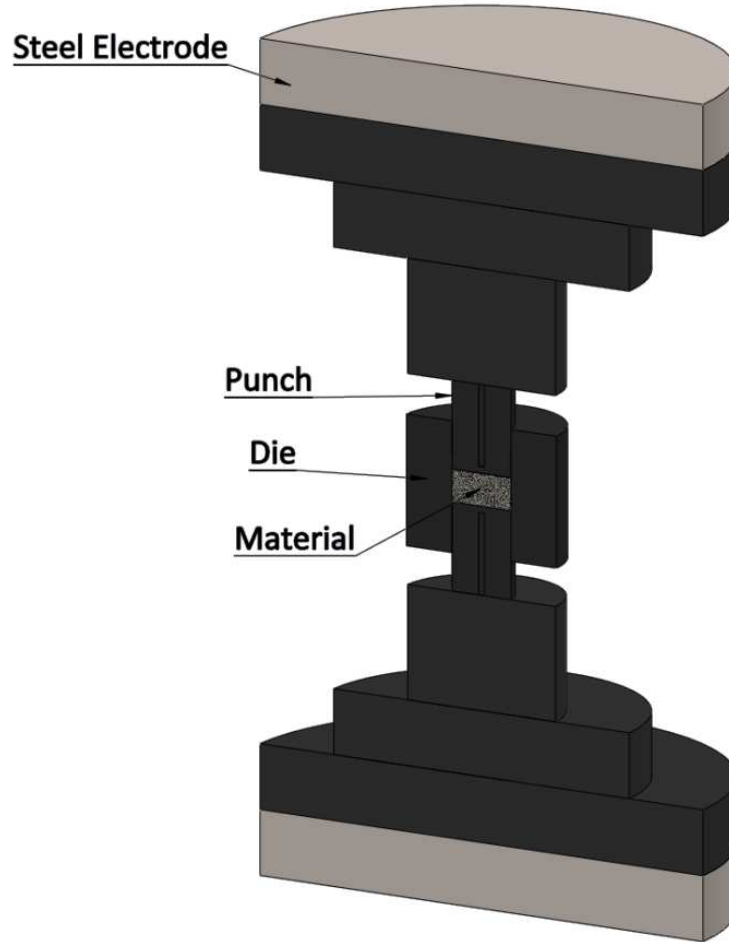


Figure 1.8: The cross-section of a typical SPS graphite stack and water cooled steel electrodes of sintering machine

The SPS samples used in this study are heated at $\sim 150^{\circ}\text{C}/\text{min}$ to a desired maximum temperature. The current $I(t)$ controlled by a thermocouple in a PID feedback loop:

$$I(t) = K_p(T_{PID}) + K_I \int_0^t T_{PID} dt + K_d \frac{d}{dt} T_{PID} \quad (1.18)$$

$$T_{PID} = T_{desired} - T_{measured}$$

The proportion-integral-derivative feedback loop equation is a function of T_{PID} , which is the difference between the desired temperature defined by the heating schedule and the measured temperature at the thermocouple probe. The coefficients K_P, K_I, K_D are numerical values that tune the response behavior.

Temperature measurement must be carefully considered in SPS. As shown by the temperature distribution on a cross-section of a standard die and punch in figure 1.9, the location of the temperature probe should be very near the sample to avoid erroneous measurements. Large temperature differences between the outside diameter surface and the powder body exists, as well as along the length of the punches.

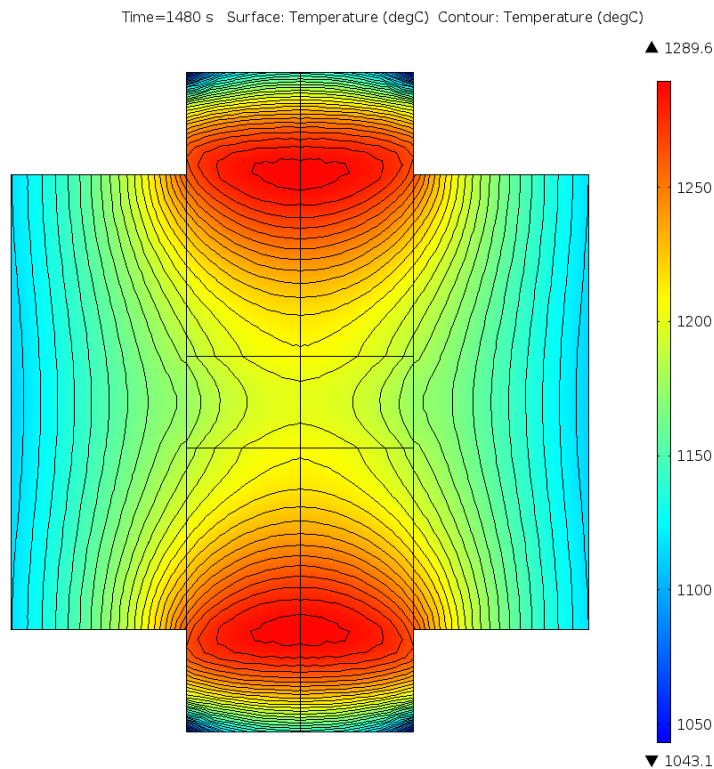


Figure 1.9: Temperature distribution in standard SPS die during heating with standard thermal boundary conditions mentioned in section 2.1

The current supplied by the SPS capacitor bank used in this study (Fuji-SPS Model 3.20) is a pulsed DC wave form. Electric fields induce interesting effects on ionic ceramic diffusion characteristics, and EFAS is a very active field of research to understand and measure the effects. In SPS, the application of an electric field from as low as 2 V/cm has been shown to significantly reduce grain growth in 3% yttria-stabilized zirconia (3Y TZ) [11]. Researchers made the 3Y TZ samples with 60 nm average grain size and 99% density. They annealed samples under at 1300°C for 10 hours under no voltage, 1.3 V/cm, 3.3 V/cm, 8.3 V/cm and 11.3 V/cm. The sample without an electric field reached an average grain size of $210 \pm 10 \text{ nm}$. The samples heated with an electric field had a 15% - 40% reduction in grain size as shown by figure 1.10.

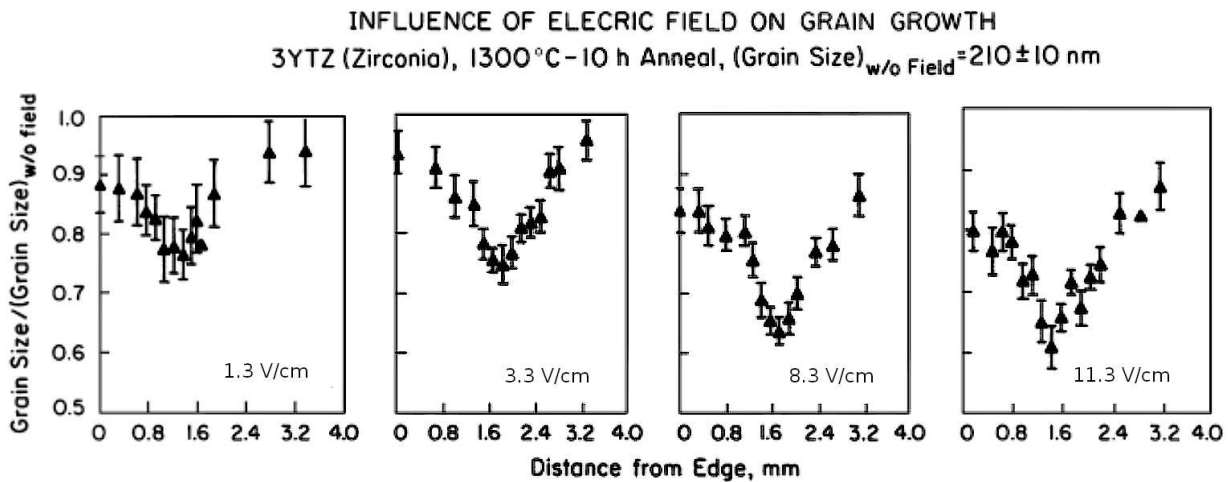


Figure 1.10: The grain size of samples annealed at high temperature with an electric field, relative to the grain size from a sample without an electric field. The field strength reported in bottom of each graph is valid at the grain size minimum. The field is variable across the sample due to the electrode configuration. The applied electric field is inversely proportional to grain size. [11]

The direction of the applied electric field has also been shown to influence the grain boundary migration [12]. Starting with $0.2 \mu\text{m}$ average size 99.99% pure Al_2O_3 powder, the researchers sintered and annealed the samples to a grain size of $170 \mu\text{m}$. They polished a surface with $1 \mu\text{m}$

diamond paste. Then the same powder was placed on the polished surface and hot-pressed to full density with a grain size of approximately $4\mu m$.

Samples were annealed at $1600^{\circ}C$ for 2 hours with no field, with a 200 V/cm field positive on the large grain side and positive on the small grain side. The grain migration from the original interface (visible by a planar array of pores) was $6\mu m$ with no field, $\sim 3 - 4\mu m$ with positive voltage on the large grain side, and $\sim 12 - 15\mu m$ with positive voltage on the small grain side.

Depending on the electric field direction, the diffusion coefficient of the rate limiting species can be increased significantly [13]. The enhanced diffusion rate of ionic ceramics due to an electric fields as well the capability of fast heating rates make electric field assisted sintering (EFAS) well apt to quickly sinter high temperature ceramics to full density with small grain sizes. Additionally, the reconfigurability of temperatures within EFAS tooling make it a promising method to create new and useful materials.

Chapter 2

Modeling the SPS process

The purpose of this study is to produce large temperature gradients on powders sintered in SPS and predict the resulting microstructure. The following section discusses the Master Sintering Curve (MSC) as a densification model. Once developed, the MSC can predict densification for the various heating schedules developed in a steady state temperature gradient.

2.1 Thermal modeling

COMSOL MultiPhysics 4.4 was used to calculate the temperature produced in graphite due to the applied current and thermal boundary conditions. SPS tooling is heated according to the user input heating schedule. A thermocouple measurement at a single point in the geometry is fed into a PID equation which controls the power. COMSOL can use this control to show transient hot spots that might only occur during the heating schedule. Details such as the temperature dependent material properties, heat transfer coefficients to the water cooled electrodes, and schemes to handle contact resistance are shown in literature references [14], [15], [16], [17], [18], [19]. Electrical contact resistance can have a large effect the temperature and electric field around the sample. High loads reduce horizontal contact resistance and tight machining tolerances can reduce the vertical resistance.

However in practice, graphite foil placed on the ID of the die improves the vertical contact resistance such that it can be ignored. The foil also prevents powder reactions with the graphite tooling. Punches are made to have a 0.1 mm slip fit with the die. Surface imperfections and

contact resistance may be the biggest obstacle to experimentally validating models to real data in SPS [20], [21], [22]. Our COMSOL model agrees well with trends seen in our SPS and it is an invaluable tool to design experiments.

Temperature dependent material properties used for graphite and zirconia:

Graphite

Thermal conductivity: $k(T) = 63 - 0.017 \cdot T$ (W/(m · K))

Specific heat: $C_p(T) = 310.5 + 1.7 \cdot T$ (J/(kg · K))

Electrical conductivity: $\kappa(T) = 1/((26 - 3 \cdot 10^{-2} \cdot T + 2 \cdot 10^{-5} \cdot T^2 - 6.4 \cdot 10^{-9} \cdot T^3 + 7.8 \cdot 10^{-13} \cdot T^4) \cdot 10^{-6})$ (S/m)

Zirconia

Thermal conductivity: $k(T) = -0.0008 \cdot T + 3.18$ W/(m · K)

Specific heat: $C_p = 0.01334 \cdot (T - 1400) + 615.5$ J/(kg · K)

Electrical conductivity: $\begin{cases} \kappa(T) = 10^{-9} & 273 < T < 1454 \\ \kappa(T) = 0.00107 \cdot (T - 1673) + 0.23421 & 1454 < T < 1871 \end{cases}$ (S/m)

To model the temperature in SPS tooling, the internal heat generation is solved for with respect to the conduction and radiation thermal boundary conditions. The heat equation says that the temperature change in an element is equal to the heat flux and the internal heat generation:

$$\rho c_p \frac{\partial \vec{T}}{\partial t} = \nabla \cdot (k \nabla \vec{T}) + \vec{J}^2 / \kappa \quad (2.1)$$

Where \vec{J}^2 / κ is the internal heat generation, \vec{J} is the spatial current density, k is the thermal conductivity, and c_p is the heat capacity. Most of the heat generated in the graphite is removed by the water cooled steel electrodes. This heat loss boundary condition is modeled with a convective heat flux:

$$Q_{conv} = hA\Delta T \quad (2.2)$$

where h is the convective heat transfer coefficient, A is the area of the steel electrode, and ΔT is the difference in temperature between the outside steel electrode surface and the $20^{\circ}C$ cooling water. Research groups with similar SPS machines use $h = 880W/mK$ [23].

A significant amount of heat generated is radiated to the SPS machine walls. Radiation heat transfer is modeled by:

$$Q_{rad} = \epsilon A \zeta (T_1^4 - T_2^4) \quad (2.3)$$

Where A is the area of the radiation surface (assuming no view factors), ϵ is the material emissivity, ζ is the Stefan-Boltzmann constant, T_1 and T_2 are radiating and absorbing surface temperature respectively. To simplify the modeling the machine walls are assumed to remain at the cooling water temperature.

2.2 Densification modeling

Collecting densification curves from SPS machines

To collect densification curves using SPS machines, the thermal expansion of the tooling and machine must be subtracted from powder shrinkage data as shown in figure 2.1. The tooling is loaded in the SPS machine and brought to thermal equilibrium with the cooling water (cycled for 12 hours prior to sintering). The heating schedule is run and the "sintered" displacement is collected (shown in black in figure 2.1). The sample and graphite tooling stays in the machine for another 12 hours to again reach equilibrium with the cooling water. The heating schedule is run a

second time and the measured displacement due to thermal expansion is collected and subtracted from the sintered displacement [24].

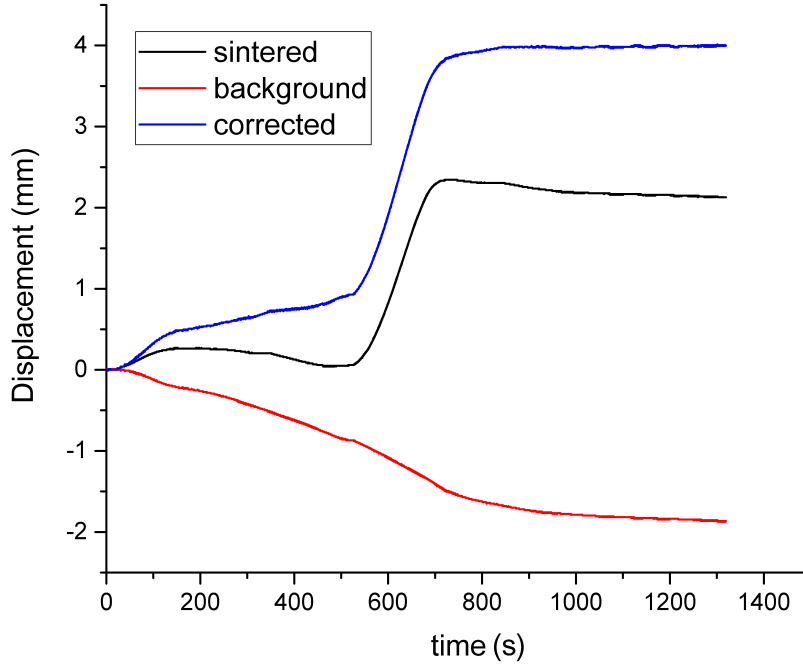


Figure 2.1: Characteristic displacement from thermal background subtraction

The density is a function of the final height of the sample, h_f , the final density of the sample ρ_f , the mass of the sample m and the cross sectional area of the punches A . The mass of the powder is $m = \rho Ah$. If the mass is conserved then the green density ρ_g can be equated to the final density with the equation:

$$\rho_g = \rho_f \frac{h_f}{h_f - disp_i} * 100\% \quad (2.4)$$

where $disp_i$ is the instantaneous displacement ($0mm < disp_i < \text{max displacement}$) subtracted from the maximum displacement.

This method assumes that the heating schedule is sufficient to fully sinter the sample, and no reactions or other process occur to change the mass. Only thermal expansion of the sintered body, graphite tooling, and rams can be reliably subtracted out. If thermal background subtractions are collected where samples don't reach 100% density then further sintering upon the second heating may add error to the calculations.

Furthermore, densification curves calculated in this manner are very sensitive to the applied load. When the SPS machine reaches an isothermal hold temperature the PID controller quickly reduces the electrical power. This change in power briefly reduces the applied load. Densification curves with an isothermal hold were found to not be useful for MSC calculations.

The three densification curves used in this work are from 5.7 g 3YTZ samples sintered with a 63.6 MPa applied load. Three different heating rates are used to bring the sample to full density without an isothermal hold: $100^{\circ}C/min$, $120^{\circ}C/min$, $140^{\circ}C/min$. Under these conditions the samples reached $\approx 97\%$ density at $1400^{\circ}C$, $1440^{\circ}C$, and $1490^{\circ}C$ respectively. The three curves are shown in figure 2.4.

2.2.1 Master sintering curve

The Master Sintering Curve (MSC) maps the densification paths associated with different heating schedules to a single logarithmic curve associated with Q_{MSC} . Densification curves as shown in section 2.2 can be collected from SPS machines, or more commonly (and accurately) a dilatometer measures displacement directly.

The $\Theta(t, T)$ term from equation 1.16 is calculated by a MATLAB script, shown in appendix A. The MRS is the integral sum of the normalized difference between $\Theta(t, T)$ curves at each density. The activation energy which sums the smallest MRS is Q_{MSC} .

The MATLAB script calculates the integral in equation 1.13 for each of Q_{MSC} and the error sum at density (equation 1.15). Once a range of apparent activation energies are calculated, the minimum value of Q_{MSC} is found as shown in figure 2.2 and all the densification curves converge on a single curve shown in figure 2.3

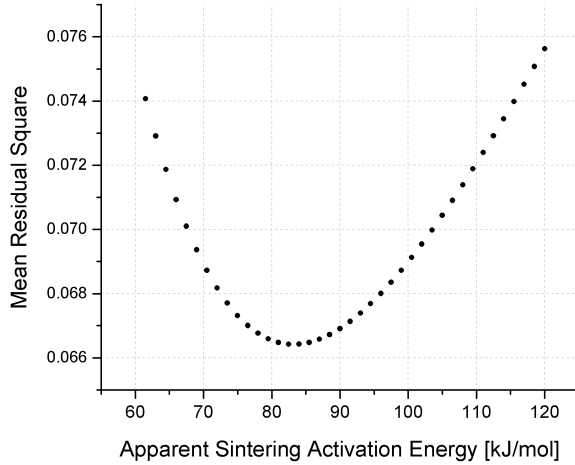


Figure 2.2: The apparent sintering activation energy, Q_{MSC} , is found by minimizing the MRS

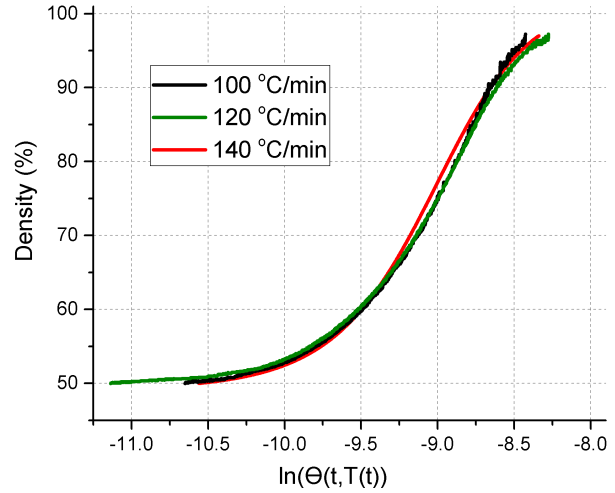


Figure 2.3: The Master Sintering Curve calculated over from 50% to 97% density where $Q_{MSC} = 84 \text{ kJ/mol}$

This MSC curve is calculated over the density range where stage II densification mechanisms are most dominant. Once the MSC is created, predicting the density for arbitrary heating schedules is straight forward. For clarity, symbols associated with the experimentally collected data have a subscript "msc" and symbols associated with *generated* densification curves using arbitrary heating schedules have "gen" as a subscript. The procedure to predict density from an MSC is:

1. Generate an arbitrary heating schedule as a function of time: $T_{gen}(t)$
2. Calculate $\Theta_{gen}(t, T)$ and match to values from $\Theta_{msc}(t, T)$
3. The index where $\Theta_{gen}(t, T) = \Theta_{msc}(t, T)$ is where $\rho_{gen} = \rho_{msc}$

The temperature and time values used to calculate the Q_{MSC} are input as arbitrary heating schedules and mapped to density in figure 2.4. The resulting fit shows that the value chosen here provides a very good densification model for this powder processed in this specific way.

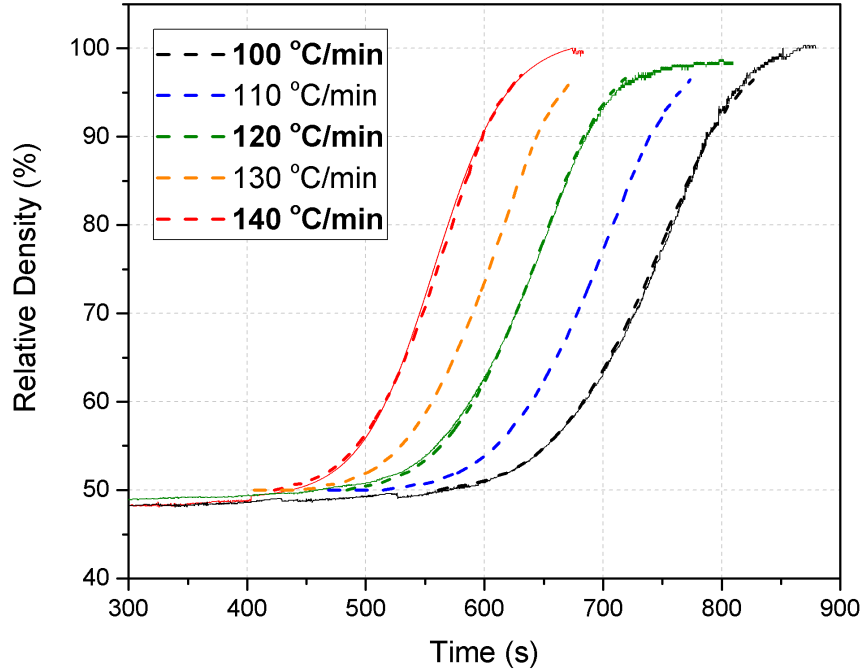


Figure 2.4: Densification versus time overlaid on the density model prediction. The solid lines are the experimentally collected densification curves. The dotted lines are generated densification curves using Q_{MSC} and theoretical heating rates

2.2.2 Sources of error in the MSC calculation

While MRS minimization shows the best fit among all tested Q_{MSC} it does not show where the error comes from. Knowing what the error is at each density for a single MSC can help while troubleshooting a model's accuracy. The pre-integral sum in equation 1.15 is a normalized difference that can compare the "closeness" between the curves at each density during each iteration of Q_{MSC}

$$\tau \equiv \frac{\sum_{i=1}^N (\Theta_i / \Theta_{avg} - 1)^2}{N} \quad (2.5)$$

The plot of τ versus ρ clearly shows the density region where the error is largest:

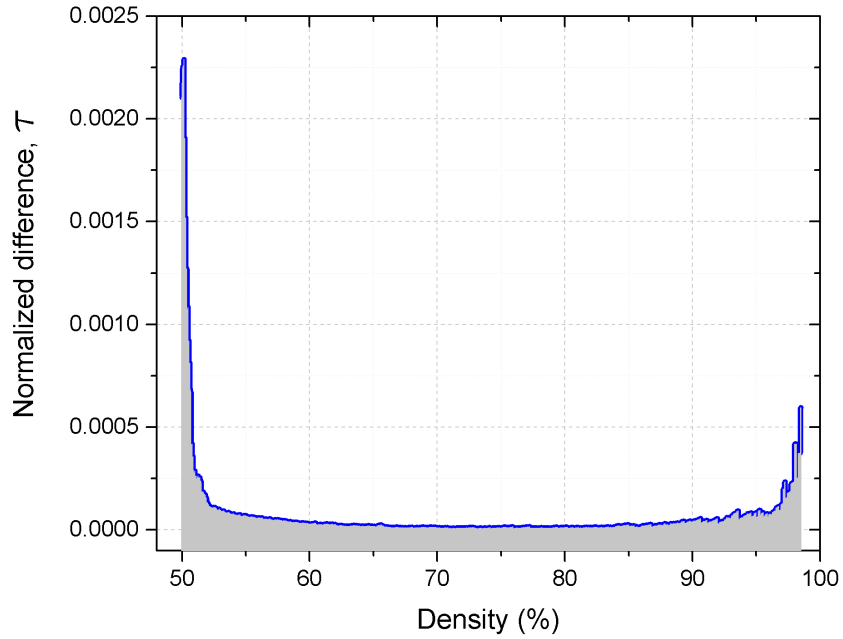


Figure 2.5: The normalized difference error τ shows the relatively large errors that may exist at the ends of the density range. Adjusting the MSC density range to avoid the large error accumulation may improve the MSC model

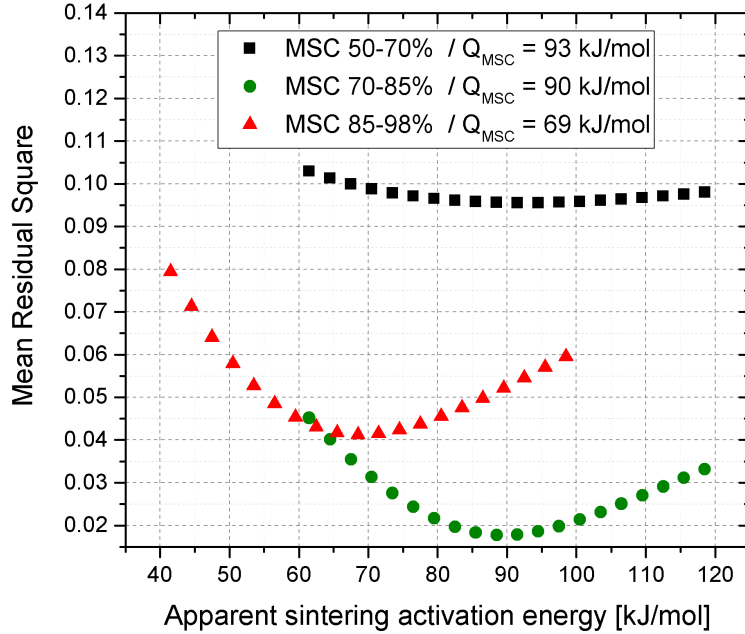


Figure 2.6: MRS minimization for the MSC calculated at various density ranges. Using several density ranges may erroneously suggest that the apparent sintering activation energy decreases as the density increases.

Figure 2.5 shows the area integrated over to calculate the MRS, clearly a poor choice of minimum and maximum densities can affect the summed value. The MRS best fit resulting Q_{MSC} value is shown in figure 2.6 when different density ranges are selected. Using several density ranges to accommodate poorly fitting data may erroneously show that the activation energy decreases over stage II. However, many researchers [25–29] find lower MRS values by breaking up the MSC density into two or more ranges. Using several density intervals may be appropriate if the primary densification mechanism changes throughout stage II. The term $\Theta(t, T)$ should either start at zero at the beginning of each density range, or it should be offset by the previous ranges' sum.

Influence of low temperatures on the MSC calculation

Recall that equation 1.13 to calculate $\Theta(t, T)$ is an integral of temperature from $t = 0$ to the time when the sample reaches the upper density limit. This means that $T(t)$ from $20^\circ C$ to the onset of stage I sintering at $\approx 1000^\circ C$ contributes to the integral sum. Though the integral sum is exponential with temperature, the time spent at low temperatures can influence the calculation. This is especially the case with fast overall sintering times. Samples in SPS often sinter through stage II density in seconds or minutes. This means the temperatures over which the MSC is valid are relatively small compared to the complete thermal history during heating and cooling.

The excess time spent at temperatures lower than that required for densification, such as the initial equalization of the controller PID temperature measurement, will change the integral sum of $\Theta(t, T)$ once stage II begins.

The low temperature data also is used to find the starting point of arbitrary heating schedules. Two densification curves collected in exactly the same way will be very different MSC values if one $\Theta(t, T)$ integral is started at $600^\circ C$ and the other at $20^\circ C$. This also means that MSC curves calculated between research groups may not be interchangeable because of different temperature measurement methods.

In order to use practical SPS data, and based on the assumptions made during the MSC derivation, time spent at low temperatures must be acknowledged and ignored. A low temperature limit where stage II mechanism begins should be explicitly defined prior to the calculation. The $\Theta(t, T)$ term is then:

$$\Theta(t, T) \equiv \int_{t_{min}}^{t_{max}} \frac{1}{T(t)} \exp\left(-\frac{Q_{MSC}}{RT(t)}\right) dt \quad (2.6)$$

where t_{min} is the time when the heating schedule reaches the lowest temperature at which volume and grain boundary diffusion are significant, t_{max} is the time at the maximum density. This is a one-to-one adjustment and will not shift $\ln(\Theta(t, T))$ if done equally to all heating schedules.

Cooling contribution to $\Theta(t, T)$

Interrupting the heating schedule to produce a specific porosity is not possible by direct comparison to the densification curves. After the SPS power is turned off, the sample continues to sinter while the material and surrounding tooling cools. For example a typical cooling profile, calculated from COMSOL for standard SPS geometry, is appended to a heating schedule shown in figure 2.7 and at an example interruption time. The heating rate is similar to that used for the middle densification curve shown in figure 2.4 which heats at $120^\circ C/min$. This example holds at $1450^\circ C$ for 10 minutes.

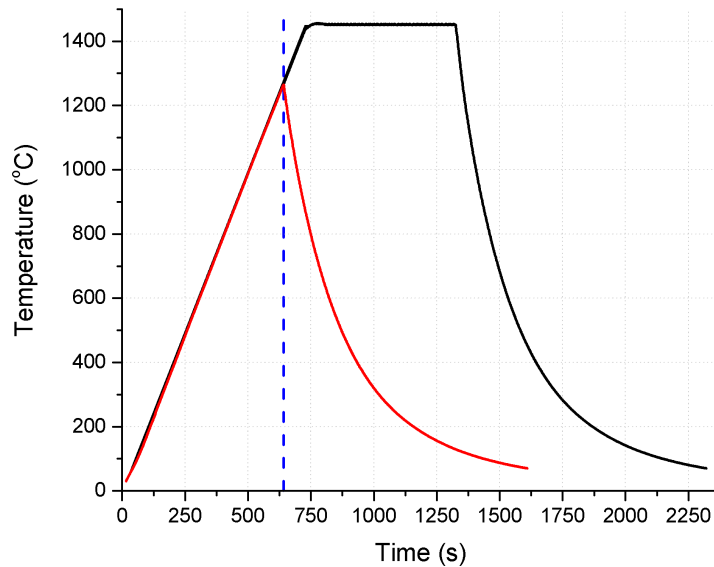


Figure 2.7: The heating schedule, $120^\circ C/min$ to $1450^\circ C$ with a 10 minute isothermal hold. The cooling profile starts at $t=1325$ s. The red line traces a possible interrupted heating schedule and resulting cooling profile

Since $\Theta(t, T)$ is an integral sum of temperature and time, the contribution during cooling should be accounted for. The area under the cooling curve is relatively similar to the area under the heating portion of this schedule. Naturally, we know that this material does not sinter below $900^{\circ}C$ so the cooling curve below this threshold temperature should not be included in the integral sum.

From the start of heating to when the SPS power is shut off at $t=640s$, the integral sum is:

$$\ln(\Theta_{heat}) = -9.0150 \quad [\ln(s/K)]$$

which corresponds to 75% density on the MSC.

The the integral sum from the start to when the sample cools below $900^{\circ}C$ is:

$$\ln(\Theta_{heat} + \Theta_{cool}) = -8.6731 \quad [\ln(s/K)]$$

which corresponds to 89.5% density on the MSC density! This large effect is due to the very small amount of sintering time relative to cooling, and the MSC calculation needs to be adjusted. These curves should show how to actually obtain the desired porosity, rather than the densification profile measured during heating only.

However, predicting the exact contribution during cooling can difficult because the cooling rate is specific to the heating schedule, tooling geometry, thermal contact resistance, radiation to the walls, convection to rams, the vacuum pressure, etc...

Fortunately, the cooling rate of a specific geometry is the same for that specific geometry heated to any *steady state* temperature. Steady state means that the heat generated in the system is equal to the heat leaving the system, so the steady state temperature essentially normalize the cooling rate.

This assumption may fail for fast heating rates when transient high temperature regions would diffuse away at isothermal holds. The difference is probably small, so the single cooling curve is used for this example. COMSOL generated cooling curves may be necessary for large geometries to verify this assumption.

The cooling profile shown in figure 2.7) was calculated with standard SPS geometry and boundary conditions. The $\ln(\Theta_{cool}(t, T))$ contribution to the MSC is calculated for every point in time along the predicted densification curve, and the MSC is adjusted.

Cooling contribution to the Θ_{msc} integral and resulting density is shown in figure 2.9. The adjusted densification profile that is shifted drastically to the left of the traditional MSC density prediction as well as the measured densification curve.

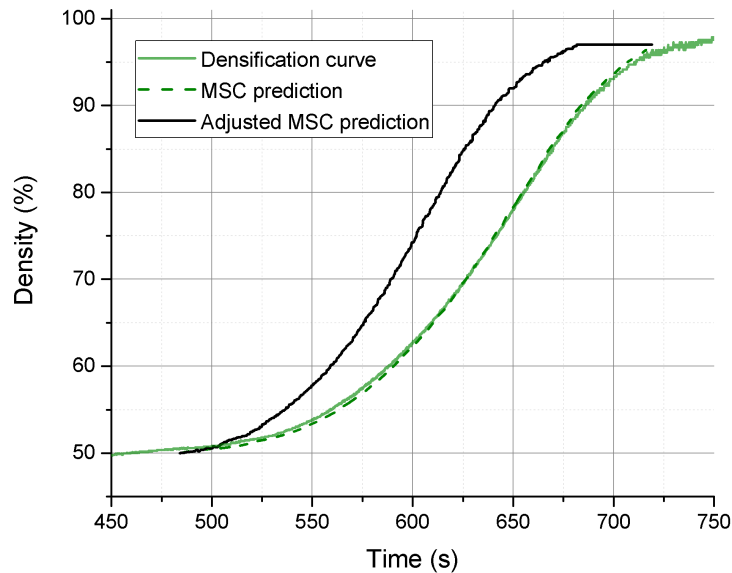


Figure 2.8: The adjusted densification curve takes the cooling rate into account. The heating schedule shown in figure 2.7 can be interrupted at any time shown here to produce a sample of specific porosity indicated by the black line.

This plot also shows that interrupting the heating schedule at $t=640s$ corresponds to 75% on the densification profile and 89.5% on the the adjusted MSC density prediction. This adjustment on the other two densification curves is shown below:

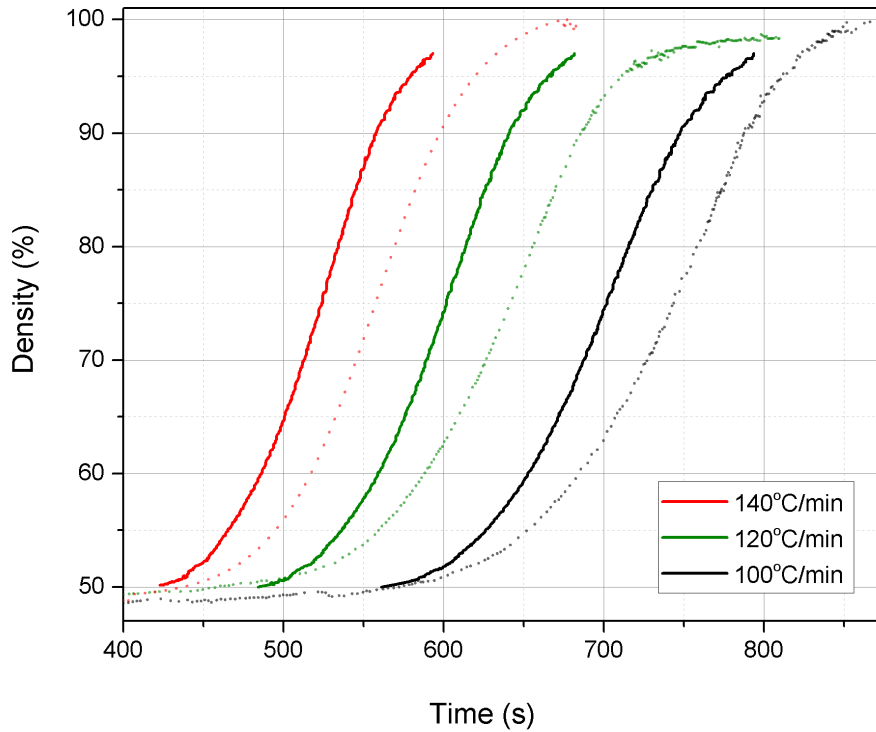


Figure 2.9: The interrupted heating schedule MSC density prediction (solid lines) overlaid on the measured densification curves(dotted lines). The solid lines are the density that would occur if the heating schedule was interrupted at that time.

Difference between actual and theoretical temperature

Recall that the predicted density overlaid on the graphs shown in figure 2.4 are calculated using the experimentally measured temperature and time. There is a slight difference between the theoretical heating schedule and the actual heating schedule produced and measured by the SPS machine. The difference between a measured and theoretical heating schedule is shown in figure 2.10:

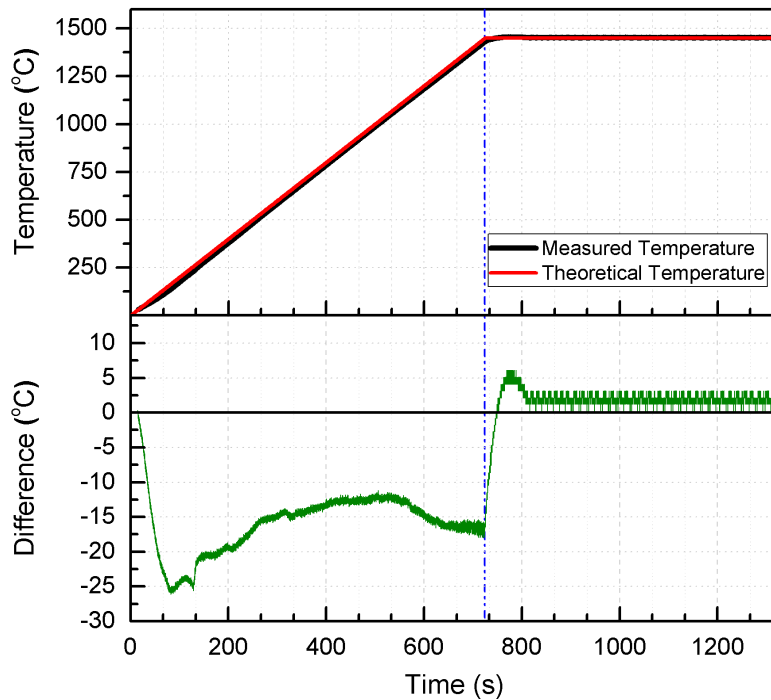


Figure 2.10: The measured temperature during the $120^{\circ}\text{C}/\text{min}$ heating rate to isothermal hold at 1450°C overlaid on the theoretical temperature. The vertical line represents the start of the isothermal hold.

The influence of the temperature difference between the two heating schedules is scaled logarithmically by the MSC, so the calculation is more affected as temperature increases. This could also be interpreted as a shifted start time. In this example 7.5 seconds corresponds to 15°C difference. The MSC density is predicted using these two heating schedules in figure 2.11. The difference of 15°C results in a 3.5% difference in the predicted density. This illustrates the need for precision when using densification curves to create materials with a specific porosity.

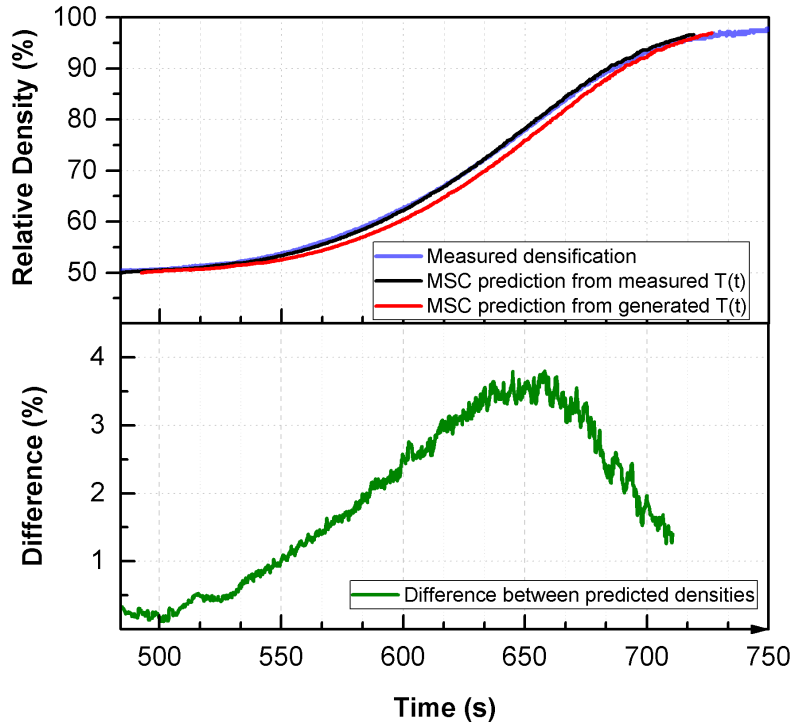


Figure 2.11: The MSC density prediction calculated from the measured temperature (black line) and the generated temperature (red line). The $120^{\circ}\text{C}/\text{min}$ densification curve is shown in blue. The maximum difference of $\approx 3.5\%$ density occurs at $t = 650\text{s}$ or $T \approx 1283^{\circ}\text{C}$ or $\rho \approx 78\%$ relative density.

Practically, slower heating schedules would allow more slop in the temperature to reach a desired density. However slow heating rates could also increase surface diffusion and deviate from the MSC model. Perhaps samples could be heated quickly to the temperature where stage II begins, and then slowly heated to the final porosity.

Value of Q_{MSC} and predicted density

Figure 2.12 shows how the density prediction changes with $\pm 5\text{kJ}/\text{mol}$ adjustments to the apparent sintering activation energy. Higher values of Q_{MSC} shift the predicted densification to lower temperatures. This means that the MSC would assign a quickly sintering powder a lower activation energy. Since SPS has some enhanced densification mechanisms as well as fast heating

rates, this may explain why the activation energies shown in this work are much lower than those calculated by tracing lattice diffusion in 3YTZ.

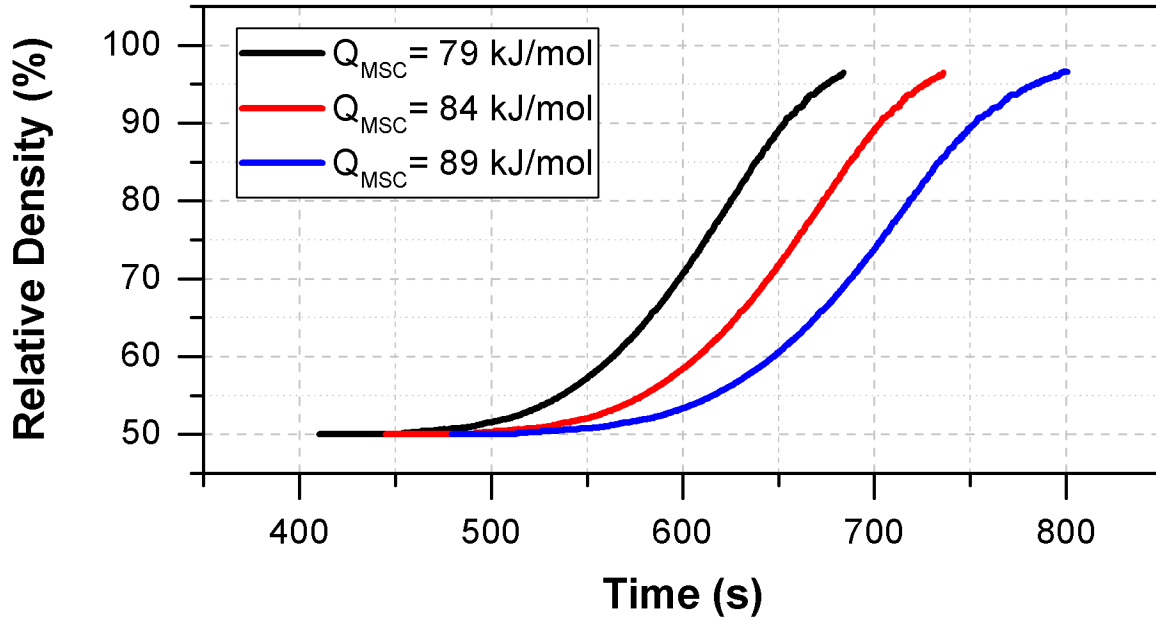


Figure 2.12: Change in MSC density prediction with $Q_{MSC} \pm 5kJ/mol$ on the heating schedule: $120^{\circ}C/min$ to $1450^{\circ}C$ with 10 minute hold. The higher values of Q_{MSC} shift the predicted densification to lower temperatures

The Arrhenius activation energy is essentially an experimentally measured parameter describing an irreversible processes sensitivity to temperature. The reaction (sintering in this case) is modeled using Q_{MSC} , which is a macroscopic sum of all the individual atomic motion pathways. Comparing $Q_{m_{sc}}$ to an activation energy measured differently would not be informative.

2.3 Conclusions and Future Work

Electric field assisted sintering is influenced by effects not included in the MSC derivation and is very sensitive to how the density is measured. Many works measure sintering shrinkage with a

dilatometer. More accurate instantaneous densification measurements could be useful to analyze MSC errors.

The range of heating schedules over which a single Q_{MSC} is calculated may model densification for much slower or much faster heating rates. The extent over which this model works has not been studied. Further research into this as well as other causes of error could help develop the method for more complex environments.

Also, samples must be kept to a small volume in order to reduce the temperature gradients in the powder [30]. This example showed a 3% density difference for $15^{\circ}C$. Large samples could have this temperature gradient even if the tooling is assumed to be isothermal. Materials sintered in temperature gradients modeled spatially could be compared to the predicted MSC densification in order to understand how the sintering is constrained.

Calculating densification curves in SPS is difficult due to the applied load changing in response to the rapid thermal expansion of the tooling during heating. Because of this, groups that calculate the MSC for SPS should clearly indicate the density ranges used and the minimum cut off temperature in order to be consistent. The extent of the cooling profile's contribution to sintering should be experimentally validated. Perhaps a consistent method for selecting the minimum temperature could help concretely define the transition between stage I and stage II, as well as produce models in literature that would be applicable more broadly.

Other early stage II transport mechanisms which lead to coarsening or densification such as surface diffusion, grain rotation and particle sliding are not captured by the MSC model [31] and could be investigated to find their full extent on the MSC model predictions. Since the MSC is essentially measuring an irreversible process's rate dependence on temperature, none of these effects may actually matter, even though they violate assumptions made during the derivation.

Chapter 3

Manufacturing Functionally graded materials with SPS

Functionally graded materials (FGMs) possess a gradient of properties that assist their function. This work aims to make FGMs with porosity gradients using EFAS methods. By sintering materials in designed temperature gradients along with the MSC density predictions, this work shows how to make arbitrarily graded materials.

This chapter describes how a powder was sintered in a designable temperature gradient along with a few results. The MSC paired with grain growth models can potentially illustrate the microstructure evolution during sintering.

3.1 Methods

Sintered zirconia + 3% mol yttria (3Y TZ) is a very common engineering ceramic due to its strength. Zirconia, or zirconium dioxide, ZrO_2 exists in a monoclinic crystal structure at room temperature and transitions to higher symmetry (higher density) structures at higher temperatures. Upon cooling after sintering however, the volume change from tetragonal to a monoclinic lattice induces large stresses that cause cracks. The addition of yttria stabilizes the zirconia in the tetragonal structure allowing the ceramic to exist in a "compressed" state at room temperature. Cracks that form in the material have sufficient energy (at the high curvature on the crack tip) to transition the crystal structure from the metastable tetragonal back to monoclinic. This phase transformation

toughening mechanism opposes crack growth and significantly improves the ceramic's fracture toughness.

The powder used in this study had an average diameter of 30 nm and supplied from TOSOH (TZ-3Y-E). Samples sintered for densification curves and grain growth analysis used 5.7g of powder in 20mm ID dies. The samples heated at $100^{\circ}\text{C}/\text{min}$ to 1200°C and held for 10 minutes reached 100% density with very little grain growth. The punches used with the 20mm ID dies were made with a 0.1 mm slip fit to allow for graphite foil on the die ID. Graphite foil prevents the powder from reacting with the tooling, decreases the punch / die sliding friction, improves the thermal and electrical conductivity between the interface, and increases tooling longevity.

3.1.1 Isothermal samples

The first step to sinter FGMs is to determine the requisite temperature conditions for the desired microstructures. Zirconia was found to reach full density at 31.8 MPa with a heating rate of $100^{\circ}\text{C}/\text{min}$ to 1200°C with a 10 minute isothermal hold. To characterize sintering behavior, 5.7 g samples were used for densification curves and grain size analysis, resulting in $\approx 3\text{mm}$ thickness. The heating schedules of the representative nodes were interrupted at $t=0, 5, 10$ minutes relative to the onset of 97% density [32]. Three samples from each interruption time were analyzed for a total of 27 samples. Every experiment was controlled by an axial type-C thermocouple within 2mm of the powder surface.

3.1.2 Temperature measurement

Temperature was measured with type-C thermocouples. The maximum temperature was limited to 1700°C to ensure the thermocouples remained reliable. Bare type-C wire (0.010" diameter

tungsten with W- 5% Rh and W- 23% Rh from Omega Engineering) was welded in an argon atmosphere using a plasma arc thermocouple welder. A typical type-C probe is shown in figure 3.1. The thermocouples were frequently compared to supplier calibrated type-K thermocouples up to their maximum operating temperature of 1370°C and with an optical pyrometer aimed to a point on heated graphite within 1mm of the probe tip.

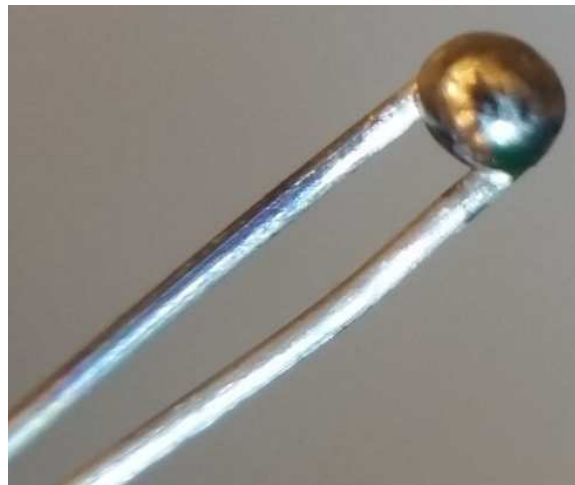


Figure 3.1: Welded type-C thermocouple

Thermocouples operate by the Seebeck coefficient where a small voltage is generated at the junction dissimilar metals. The measured voltage is a function of temperature at the thermocouple (TC) type-C probe (shown in figure 3.1) relative to the temperature at the thermocouple wire - measurement device metal junction. The voltage generated at the type-C probe tip is only known if the voltage at the TC wire to copper junction is known. Historically the TC wire - copper wire junction was submerged in an ice bath to maintain an exact temperature and thus voltage difference.

A cold junction compensator (CJC) will simulate the voltage at 0°C electronically and is safer to use in a lab environment. The CJC provides a stable voltage bias correlating to $\pm 0.25^{\circ}\text{C}$ at 25°C , $\pm 0.5^{\circ}\text{C}$ from 15°C to 35°C , and $\pm 0.75^{\circ}\text{C}$ at 10°C to 50°C . The lab was maintained close to 25°C

to reduce this error. The type-C TC wire route was: TC type-C wire → type-C TC extension wire → copper vacuum feed through → CJC → copper wire to DAQ.

The measured mV is converted to temperature with equation 3.1 created from data provided by Omega Engineering:

$$\begin{aligned} T = & 0.370098 + 73.1494 \cdot mV + (-3.62313) \cdot mV^2 + (0.337303) \cdot mV^3 \\ & + (-1.95236 \times 10^{-2}) \cdot mV^4 + (6.94508 \times 10^{-4}) \cdot mV^5 \\ & + (-1.32771 \times 10^{-5}) \cdot mV^6 + (1.05022 \times 10^{-7}) \cdot mV^7 \end{aligned} \quad (3.1)$$

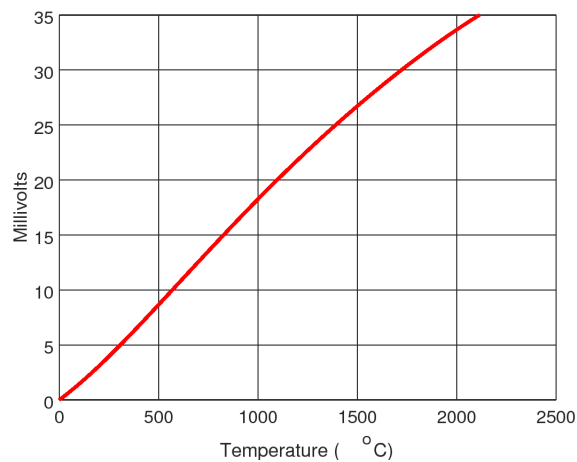


Figure 3.2: Type-C thermocouple voltage versus temperature

More information about the problems and solutions for SPS high temperature measurement is shown in appendix B

3.1.3 SPS tooling for controllable thermal gradients

The tooling used to study temperature gradients manipulates the regions and extent of Joule heating in the graphite in order to produce steady state axial gradients on the $\approx 10\text{mm}$ thick cylindrical sintered body. Three possible SPS tooling configurations which produce axial temperature gradients are shown in figure 3.3. The left most die has a tapered outside diameter which creates a locally high current density in the reduced section. This method produces relatively low axial temperature gradient $\approx 20^\circ\text{C}/\text{mm}$ compared to the next two configurations. The die shown in the middle configuration is offset from the top punch, creating extremely high current density on that side. While this method produces extremely high temperature gradients, it is not easily controllable and the compaction hoop stresses caused the dies to break relatively low applied loads.

The method shown on the right in figure 3.3 simulates the offset die's current pathway constriction (see figure 3.4) and centers the sample in the die which allows higher applied loads. The "hot punch" is isolated from the die by a nonconductive, high temperature ceramic (Al_2O_3) sleeve such that the temperature gradient is proportional to the surface area contacting the die. This tooling configuration called "Simulated Offset Die" (SOD) is used in this work.

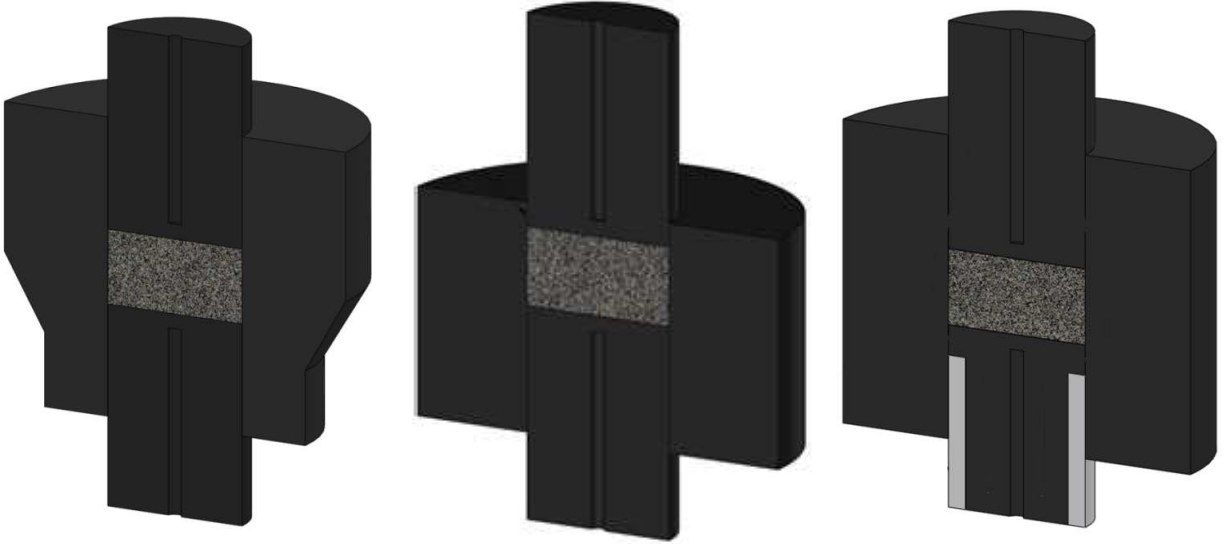


Figure 3.3: Tooling geometry used to produce controllable temperature gradients in 20mm inner diameter SPS tooling.

Each SOD punch is custom machined to fit the ID of the alumina sleeve, which helped maintain similar thermal conductivity between tests and simplified the thermal model. The SOD tooling creates a steady state temperature gradient shown in figure 3.6 and 3.10. The "height" dimension of a SOD punch is annotated in figure 3.5. The SOD punches are always the bottom punch in a standard SPS die and the bottom of the die is supported so only the top punch can move during densification. Temperatures on the hot side and the cold side were measured by type-C thermocouples in axial holes drilled to within 2mm of the powder surface (see figure B.1)

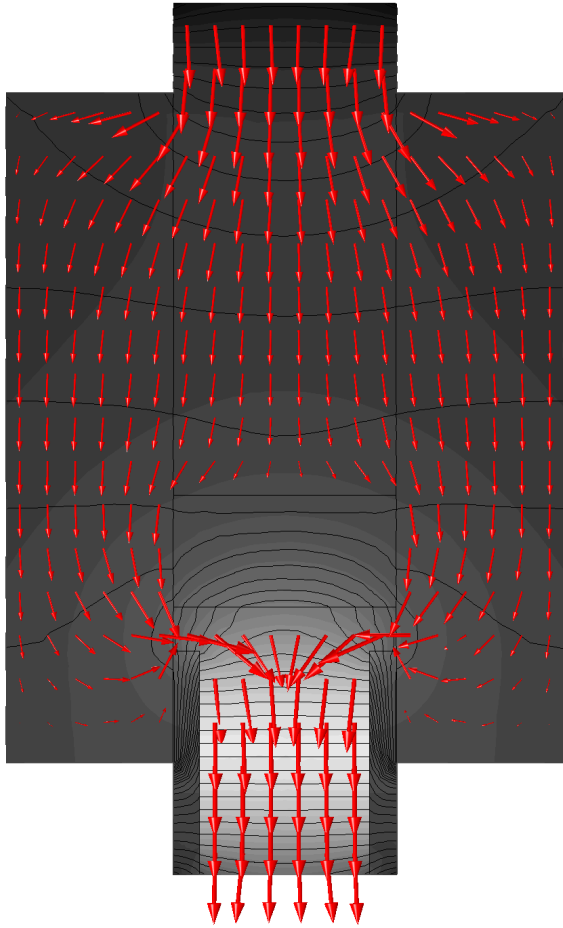


Figure 3.4: The current pathway and log normalized density arrows inside the standard SOD tooling sintering a nonconductive material

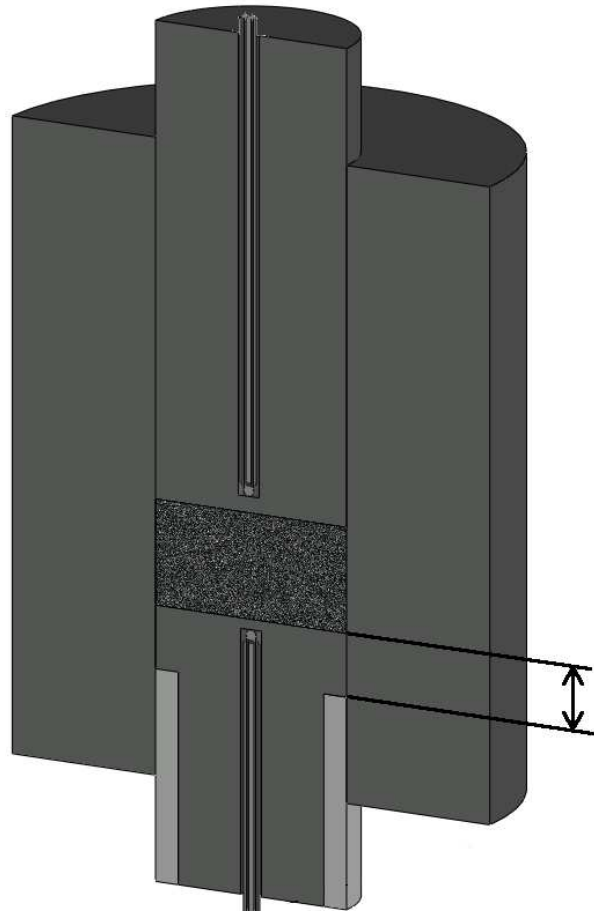


Figure 3.5: The dimensioned feature of SOD punches and the axial thermocouples used to measure the hot and cold side temperatures

SOD height and temperature gradient

The experimental temperature gradients produced by SOD punches of various heights are shown in figure 3.7. The 6mm SOD created $1200^{\circ}C$ on the cold side and $1700^{\circ}C$ on the hot side. The cold side gets colder as the SOD punch height decreases and the temperature gradient increases. All heating schedules were controlled by the thermocouple on the hot side in order to prevent temperature overshoot at the isothermal hold.



Figure 3.6: Visible temperature gradient on die heated with a 6mm SOD punch

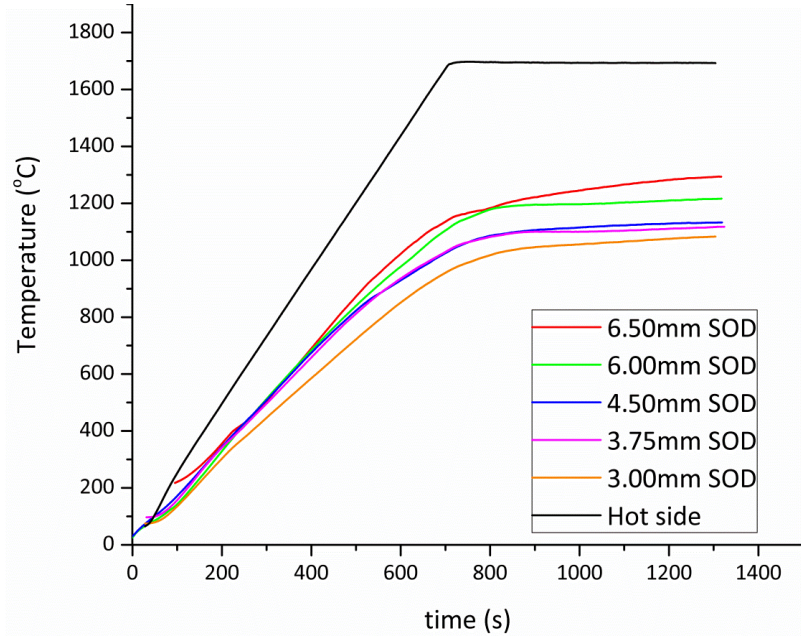


Figure 3.7: Resulting temperature gradients from various thickness SOD punches.

3.1.4 SEM procedure and grain size analysis

The sintered samples were sectioned and polished to 1μ diamond media on a plain-weave nylon fabric backed with silicon. The samples were cleaned with water, acetone, ethanol, and then thermally etched in air at $950^{\circ}C$ for one hour to relieve grain boundaries. The sectioned and polished FGM samples were loaded into the SEM and oriented so the grain size images were collected along the FGM centerline. Three images for grain size analysis were collected every 1mm along the height of the FGM sample.

The 3D average grain radius, r_{grain} was calculated from the 2D SEM micrographs using the three circle intercept method shown in figure 3.8. The circumference of the three concentric circles is converted from pixels to nm . The average radius of the grains is converted from the 2D representation by multiplying by 1.56 correction factor [33].

$$r_{grain} = \frac{\text{Number of intersections}}{\text{Sum of the circumference of three circles}} * 1.56 \quad (3.2)$$

All SEM micrographs used to calculate grain size were collected with a 10mm working distance at X15,000 magnification. Each image had at least 150 grain boundaries and circle intersections.

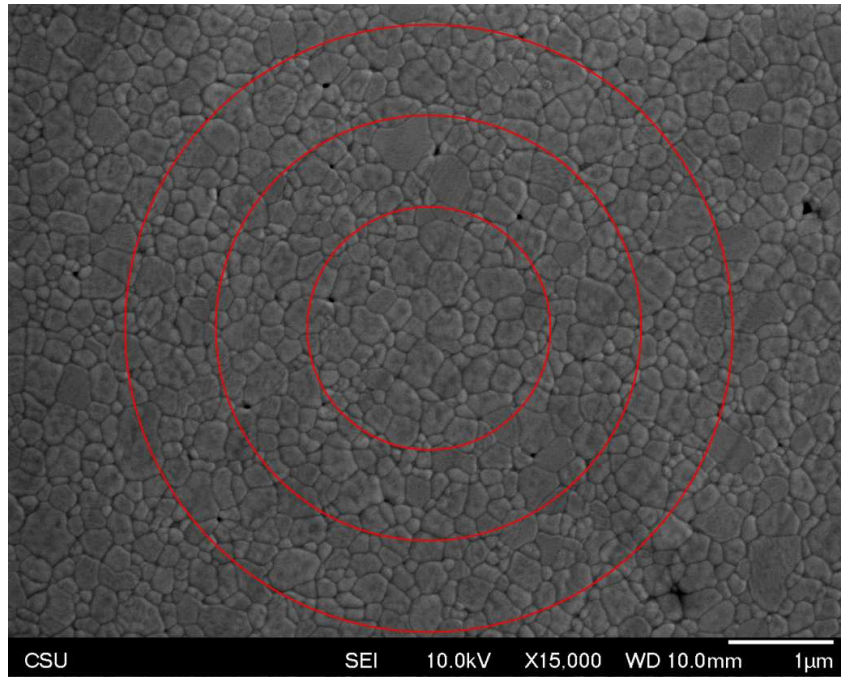


Figure 3.8: Grain size calculated by counting the number of times the red circles intersect with a grain boundary

3.2 Results and Discussion

The preliminary "isothermal samples" sintered to determine the minimum temperature and pressure conditions did not correlate to full density on the FGM sintered at the same pressure. The bulk FGM only reached $\approx 88\%$ relative density even though the cold side saw a heating schedule

of $100^{\circ}\text{C}/\text{min}$ to 1200°C with a 10 minute isothermal hold. The bulk FGM samples only reached full density (using the same conditions) with a 63.6 MPa applied load.

A picture of the cross section of the 88% dense FGM sintered with 31.8 MPa is shown in figure 3.9 after polishing. The shape of the dark region appears to match the isothermal contours shown in figure 3.9, indicating that the COMSOL models are at least relatively predictive to the physics in the SPS tooling. The dark region (from the hot side) may correspond to oxygen vacancies in the lattice, as researchers have shown that increased vacancies form at higher sintering temperatures [34] in this material, especially in graphitic environments. The whole FGM returned to a dull yellow color after the thermal etch procedure, indicating that elevated temperatures in air allowed the oxygen vacancies to anneal out. The microstructure on the cold side, middle, and hot side are shown in figure 3.13



Figure 3.9: FGM cross section prepared for SEM grain size analysis. The hot side was heated to 1700°C and held for 10 minutes. The shape of the dark color region is similar to the isothermal lines shown in the COMSOL model

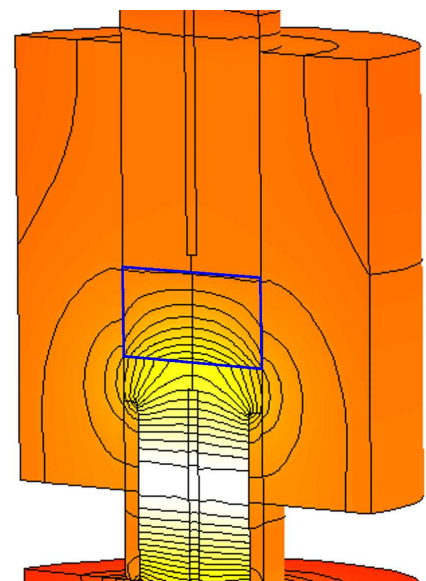


Figure 3.10: Steady state temperature gradient from a 6mm SOD punch. The 10mm tall x 20mm diameter sample is outlined in blue

Figure 3.11 shows the heating rates of points in the FGM calculated in the COMSOL model. The FGM temperature is controlled by a thermocouple on the hot side and follows the same schedule as the experiment. All points other than the hot side have a non-constant heating rate as they reach steady state.

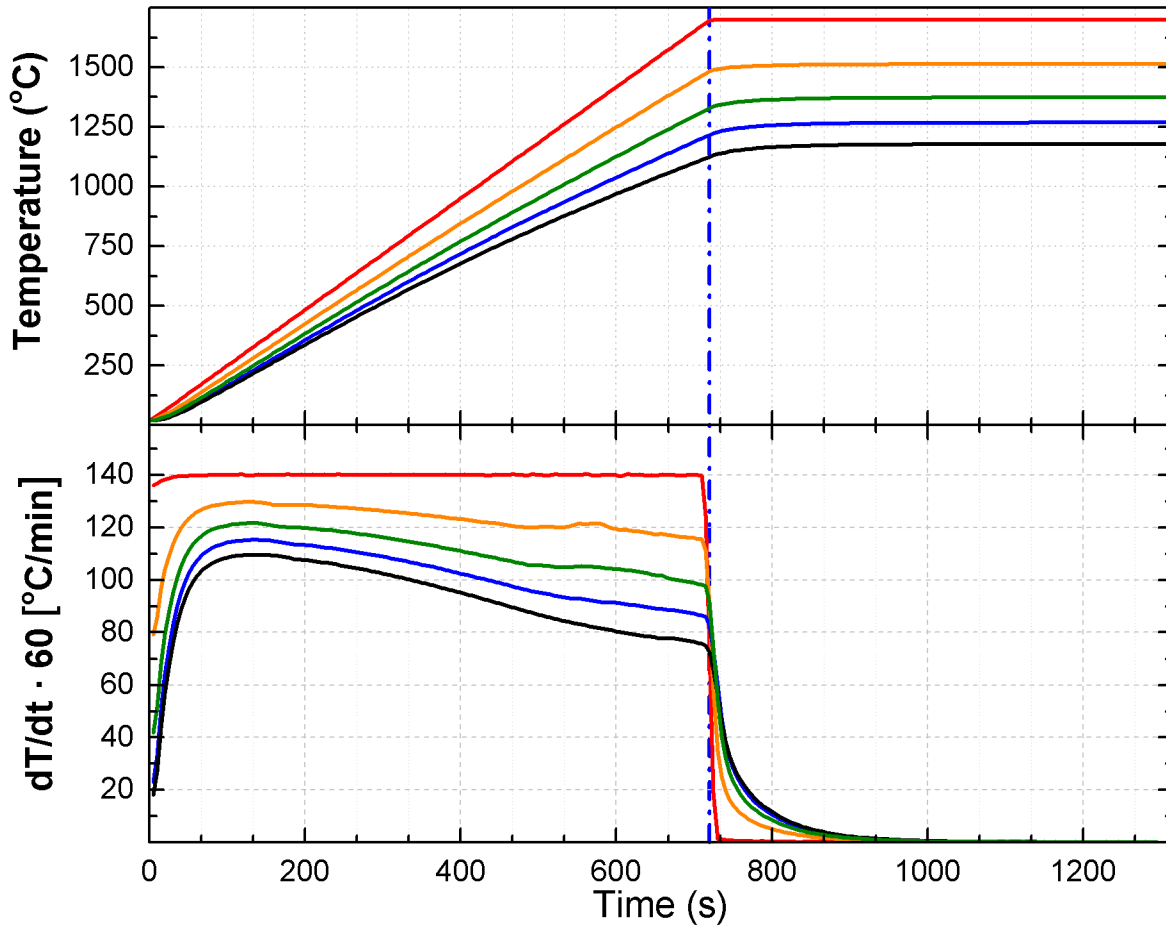


Figure 3.11: The temperature and heating rate of five points inside the FGM during sintering. These COMSOL generated heating schedules can be used to create MSC density predictions to produce porous FGMs by interrupting the heating schedule

Figure 3.12 visualizes the microstructural evolution during sintering in a temperature gradient. The plot the MSC density prediction due to the temperature data from figure 3.11 as well as the

interrupted schedule density prediction. These FGMs are sintered in tooling very similar to the isothermal "standard" SPS tooling, so the cooling curve shown in figure 2.7 is still valid.

The MSC, where $Q_{MSC} = 84kJ/mol$ calculated over $50\% < \rho < 97\%$ using a low temperature cut off of $900^{\circ}C$, is used to predict the densification of the five nodes inside the FGM:

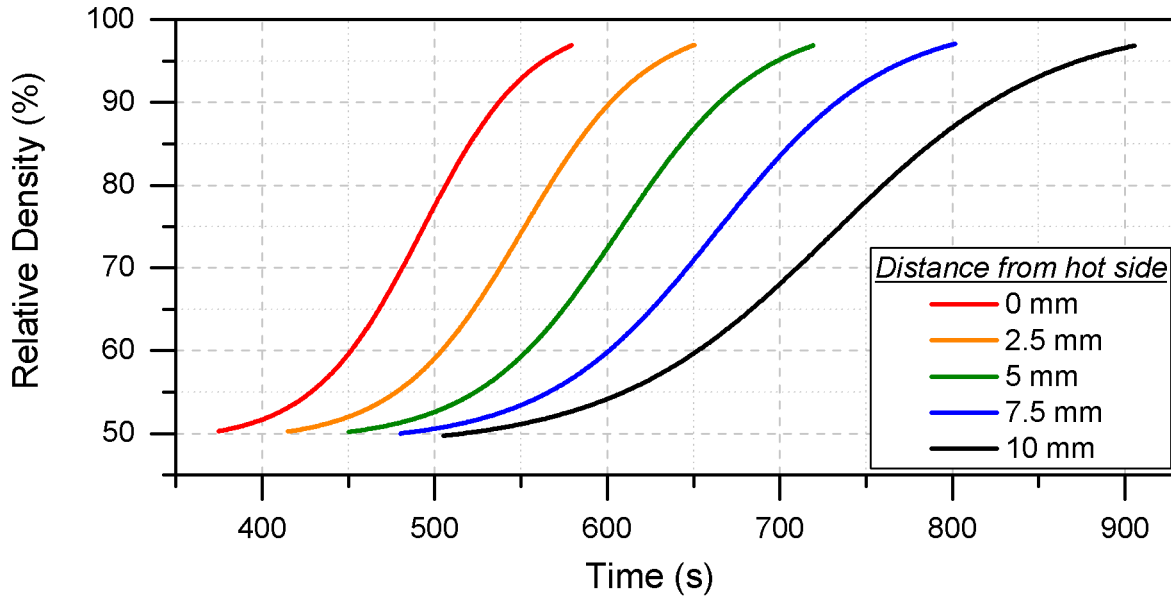


Figure 3.12: The MSC model of densification in a temperature gradient adjusted with the cooling $\Theta_{cooling}(t, T)$ contribution if the heating schedule is interrupted at any time
 MSC calculation data: $Q_{MSC} = 84kJ/mol$, $50\% < \rho < 97\%$, $T_{min\ cutoff} = 900^{\circ}C$

Processes created with this type of calculation could very quickly determine the requirements for an application specific density gradient.

The microstructure of the sample sintered with 31.8 MPa is shown in figure 3.13. The fully dense microstructure of the hot and cold side of an FGM sintered with 63.6 MPa are shown in figure 3.14. The grain size distribution along the length of the two FGMs are shown in figure 3.15. The hot side grains in the 31.8 MPa sample grew to almost double that of the 63.3 MPa sample.

Pinning of the grain growth may indicate that high applied loads can change the diffusion at the grain boundaries, which may influence the MSC calculation.

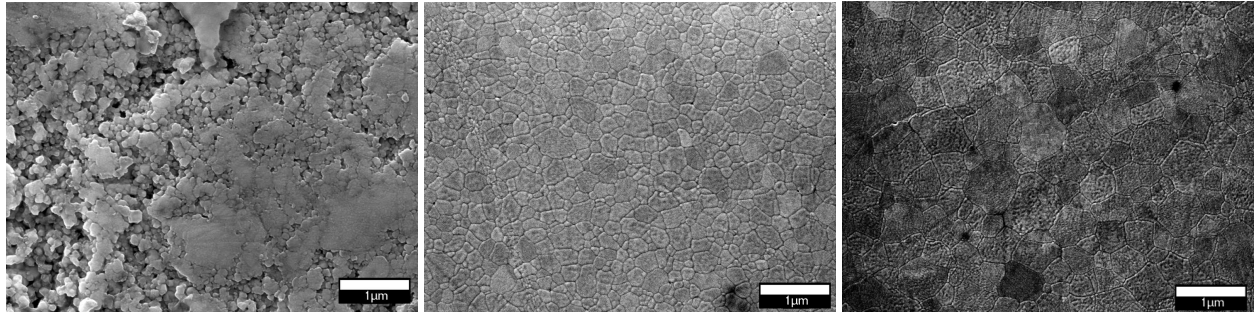


Figure 3.13: SEM micrographs of cold side (left), middle, and hot side (right) of the FGM sintered with 31.8 MPa

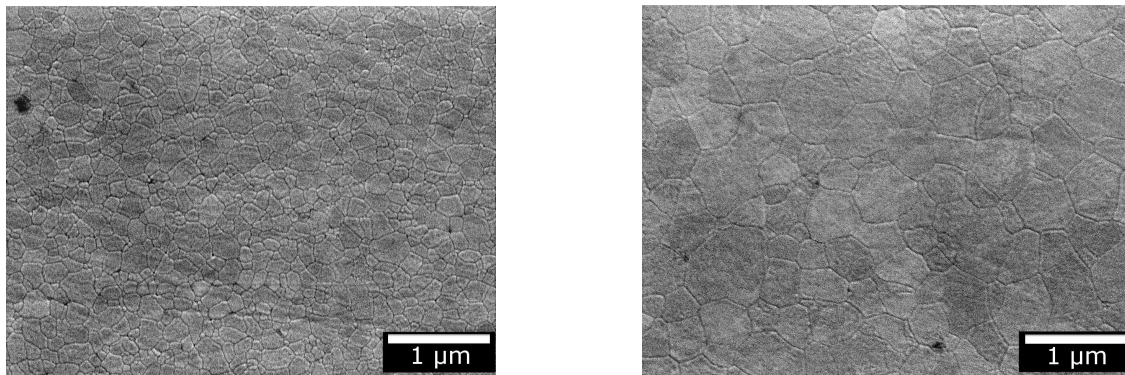


Figure 3.14: SEM micrographs of cold side (left) and hot side (right) of the FGM sintered with 63.6 MPa

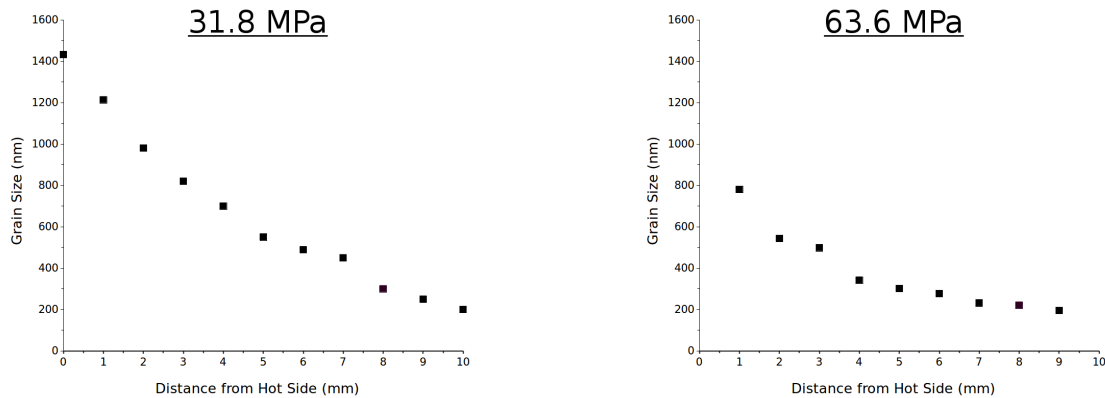


Figure 3.15: Grain size distribution along axis of FGMs sintered with two different pressures. The grain size on the hot side is almost doubled in the low pressure FGM

3.3 Conclusions and Future work

This preliminary work shows a method to manufacture materials with desired microstructural gradients using the MSC prediction and thermal modeling. The MSC shows that the densification of this powder is very sensitive to the heating schedule. Transient temperature gradients due to low thermal conductivity of many materials (and porosity) may introduce unquantified error. The simplified thermal model assumes the sample is always 10mm thick, which is actually never the case unless $\rho = 100\%$. If the thermal model could incorporate the MSC prediction, the displacement of the tooling and an adaptive mesh would be more accurate. Further investigations should study the mechanism inhibiting grain growth and densification in the 31.8. MPa sample compared to 63.6 MPa sample.

Further work should sinter materials with porosity gradients using the SOD method to validate the $\Theta_{cool}(t, T)$ contribution. Application specific materials could be developed using this work if the geometry is appropriate for SPS. Validation of the MSC over a wide range of heating schedules would inform the MSC model and error analysis.

Chapter 4

Scalability of the EFAS process

The initial goal of this project was to develop a method to sinter large diameter samples in large temperature gradients. Studies have shown that a 10mm thick plate of boron carbide is a very effective ballistic material. Researchers have melted aluminum into the porous side of FGM boron carbide to create a cohesive aluminum backing. Large diameter samples could then be cohesively bonded to other structures and serve as a lightweight armor. However, increasing SPS sample diameters while maintaining very high temperatures (2100°C for fully dense boron carbide) and an axial temperature gradient is very difficult.

4.1 Scaling up standard SPS tooling

A significant amount of time was devoted to understanding the way internal heat generation works and how to engineer scalable graphite tooling. Observations and COMSOL models below describe some of the difficulties in scaling the SPS process.

4.1.1 Joule heating in large conductors

In one dimension, the electrical power P dissipated in a wire of length L and cross sectional area A is $P = IV = I^2R$ where the resistance R is $R = L/\kappa A$ and κ is the electrical conductivity of the wire material [S/m]. In three dimensions, the heat equation says that the temperature change in an element is equal to the heat flux and the internal heat generation:

$$\rho c_p \frac{\partial \vec{T}}{\partial t} = \nabla \cdot (k \nabla \vec{T}) + \vec{J}^2 / \kappa \quad (4.1)$$

Where \vec{J}^2 / κ is the internal heat generation, \vec{J} is the spatial current density, k is the thermal conductivity, and c_p is the heat capacity. Typically, Joule heat (e.g. resistive heating or ohmic heating) is focused on small diameter wires used in ovens or heaters. The large cross section of SPS tooling is a unique application of Joule heat.

Instinctively, we think the temperature generated in large conductors is essentially dependent upon the cross sectional area normal to the current flow. However, this is not an accurate understanding. Figure 4.1 illustrates a graphite rod with reduced cross sectional area on both ends.

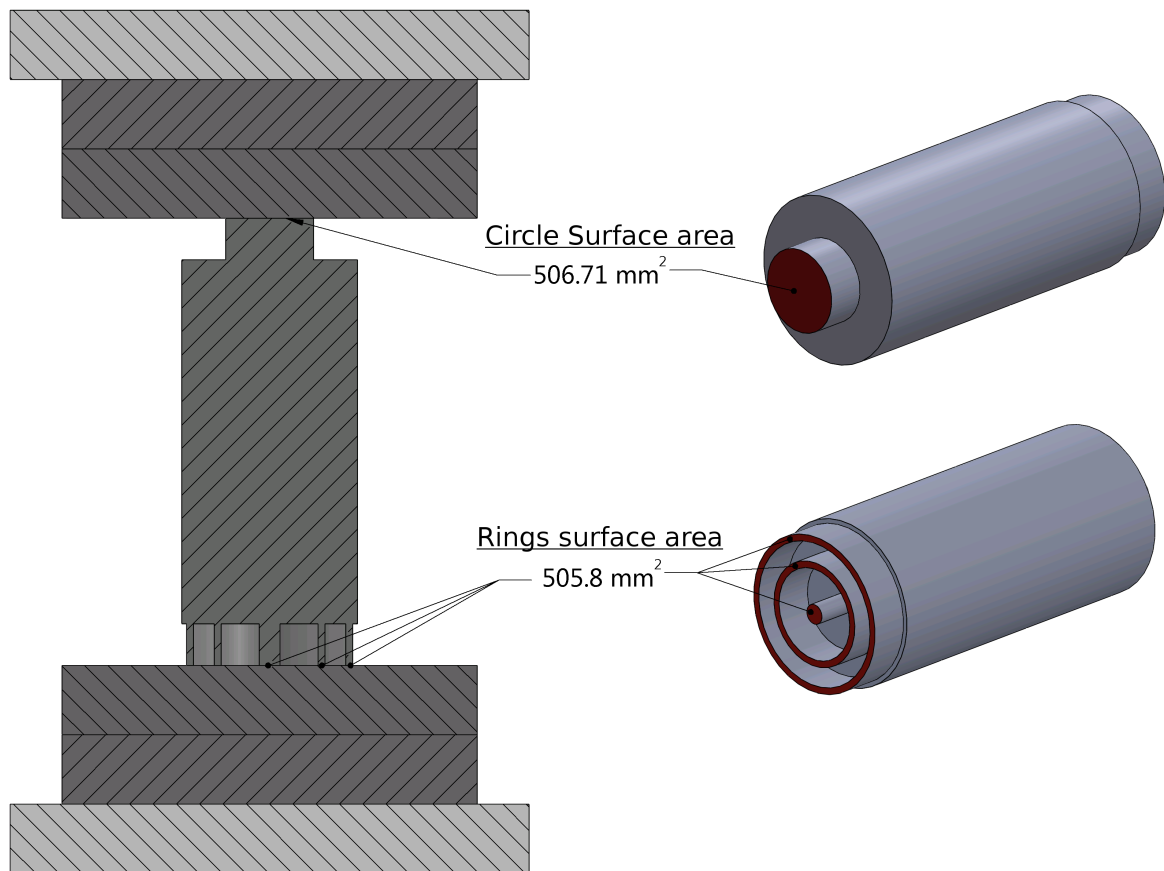


Figure 4.1: Graphite components (dark gray) between electrodes (light gray) in an SPS stack. The reduced surface area (and volume) on both ends of the long cylinder are the same.

The long cylinder is pressed between two graphite spacers in an otherwise standard SPS stack. This geometry is heated by 100 A for 1000s to reach quasi-equilibrium and the average temperature on the two surfaces is plotted in figure 4.2

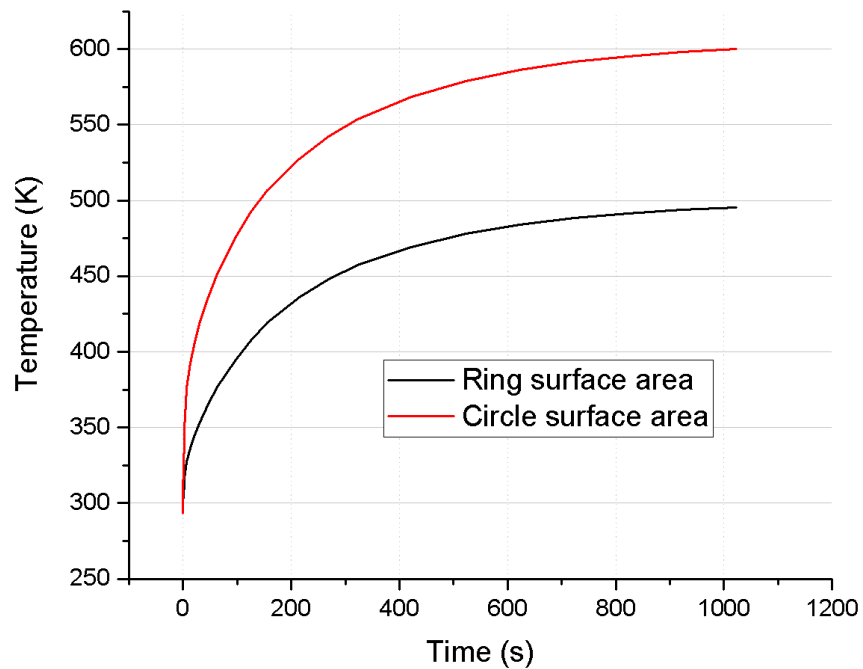


Figure 4.2: The average temperature on surfaces shown in figure 4.1 after constant current heating for 1000s

While the current density of the 2D slice [A/m^2] on the two areas are the same yet the ring surface is $100^{\circ}C$ cooler than the circle area. The temperature distribution of the two sections from the COMSOL model is also shown in figure 4.3.

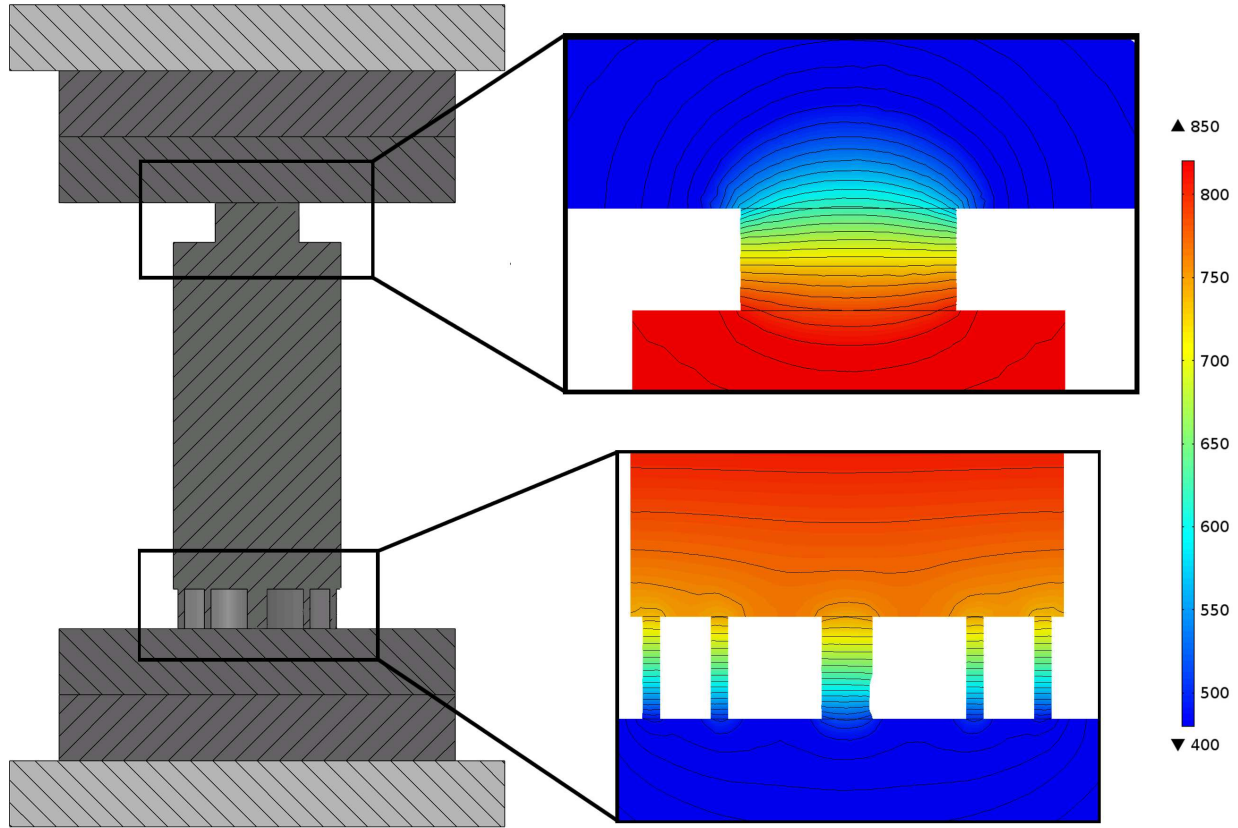


Figure 4.3: The temperature distribution (in K) after constant current heating for 1000s.

The phenomenon affects scalability in SPS. Similar ring surface designs have been published in literature to help "spread out" the temperature on large diameter samples [35], but the maximum temperature is greatly reduced compared to a single cylindrical surface area.

The steady state temperature in an infinitesimal element is dependent on the internal heat generation and flow in and out. The heat flow leaving the element is larger when the surrounding material is cooler. Dividing the volume in small rings over which current can flow reduces the maximum possible temperature.

Non-radially symmetric tooling

Other practical limitations to SPS manufacturing is the radially symmetric nature of Joule heating. All of the tooling used in this work has been axially symmetric, but not all applications are so convenient.

For example, figure 4.4 shows a 75 mm x 75 mm x 10 mm thick sample in graphite tooling. The square punches compress the sample into a square hole cut in a die. Figure 4.5 shows the temperature gradient on this geometry heated by 4000A for $t=1000s$ until steady state. The cooler area in the corners of the sample must be reduced by modification to the graphite, otherwise the inhomogeneity will prevent SPS from sintering a homogeneous material.

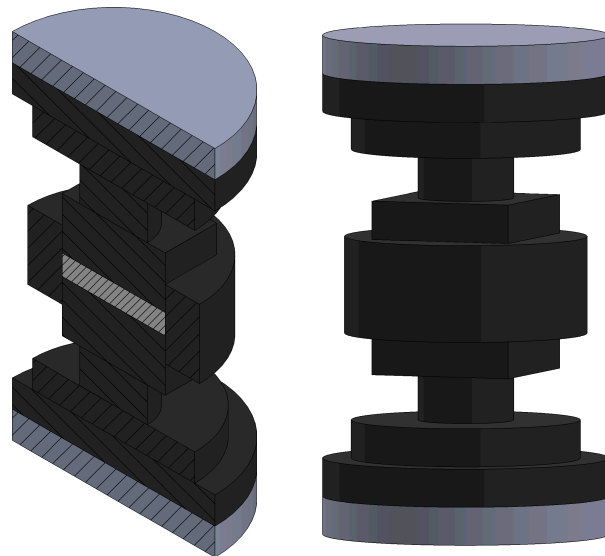


Figure 4.4: Example of non-radially symmetric tooling to sinter 12 mm thick square sample 75 mm x 75 mm. The punches are 38mm tall, the die is 127 mm diameter

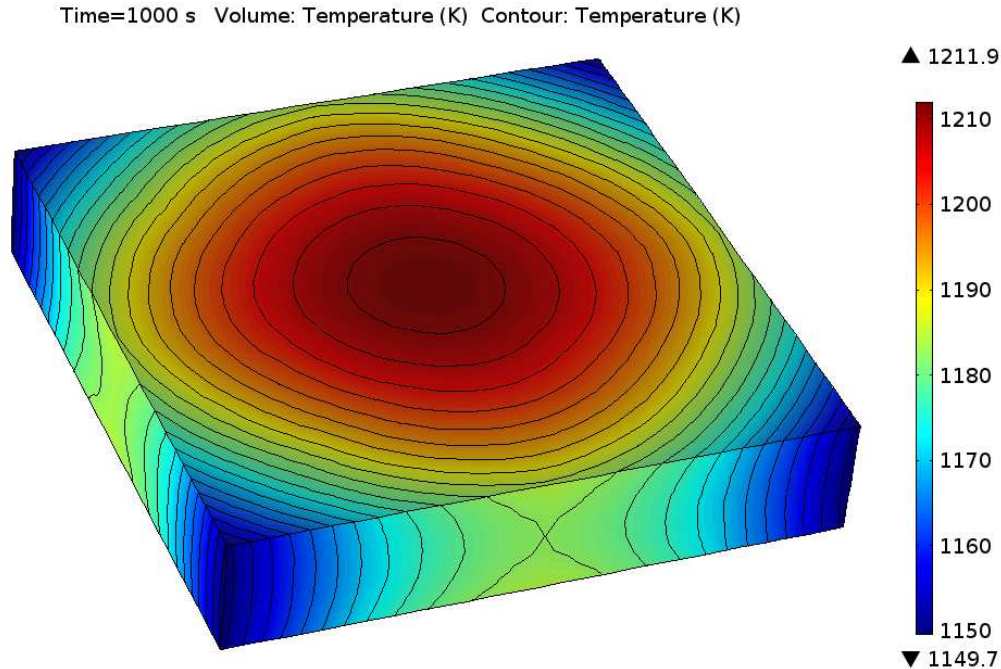


Figure 4.5: The temperature distribution on 75 mm x 75 mm x 12 mm thick square sample after constant 4000 A for 1000s. Note the colder temperatures on the corners of the sample. The radial temperature distribution is approximately 60°C and $T_{max} = 1211\text{K}$

4.1.2 Methods to improve temperature homogeneity

The thermal gradients that develop in SPS are mainly due to the current density and the thermal boundary conditions on the graphite tooling. COMSOL models show the heating and cooling rates, as well as the steady state condition. Heat primarily conducts to the water cooled steel electrodes or radiates to the water cooled SPS chamber walls.

Isolating sample from water cooled electrodes

The most significant heat flow away from the sample is toward the water cooled electrodes. This flux creates axial temperature gradients on the sample and reduces the maximum attainable temperature.

The standard SPS stack shown in figure 1.8 creates a hot spot in the volume of the punch that extends outside of the die. In large diameter samples, the volume of the punch extended outside of the die might be too large to generate adequate heat. The addition of small diameter "hot spacers" between the graphite plates generates large amounts of heat that both flows into the die and to the water cooled electrodes.

In high aspect ratio samples, the die and punches must be long enough to move the sample away from their axial temperature gradient. The 75 mm tall sample shown in figure 4.6 illustrates this effect. The die and lower punch are fixed while the top punch displaces during sintering. The sample is located far away from the hot spot so it will sinter in a relatively isothermal region. This can be seen visually in the picture in figure 4.6 where the color of the die is relatively uniform at the location of the thermocouple, which is centered on the sample.

The 75 mm tall sample had to be compressed and sintered to 60% density before the tooling shown here could fit between the SPS rams, which had a 300 mm maximum opening. Samples longer than 75 mm are not easily sintered even with large (83 kW) SPS machines.

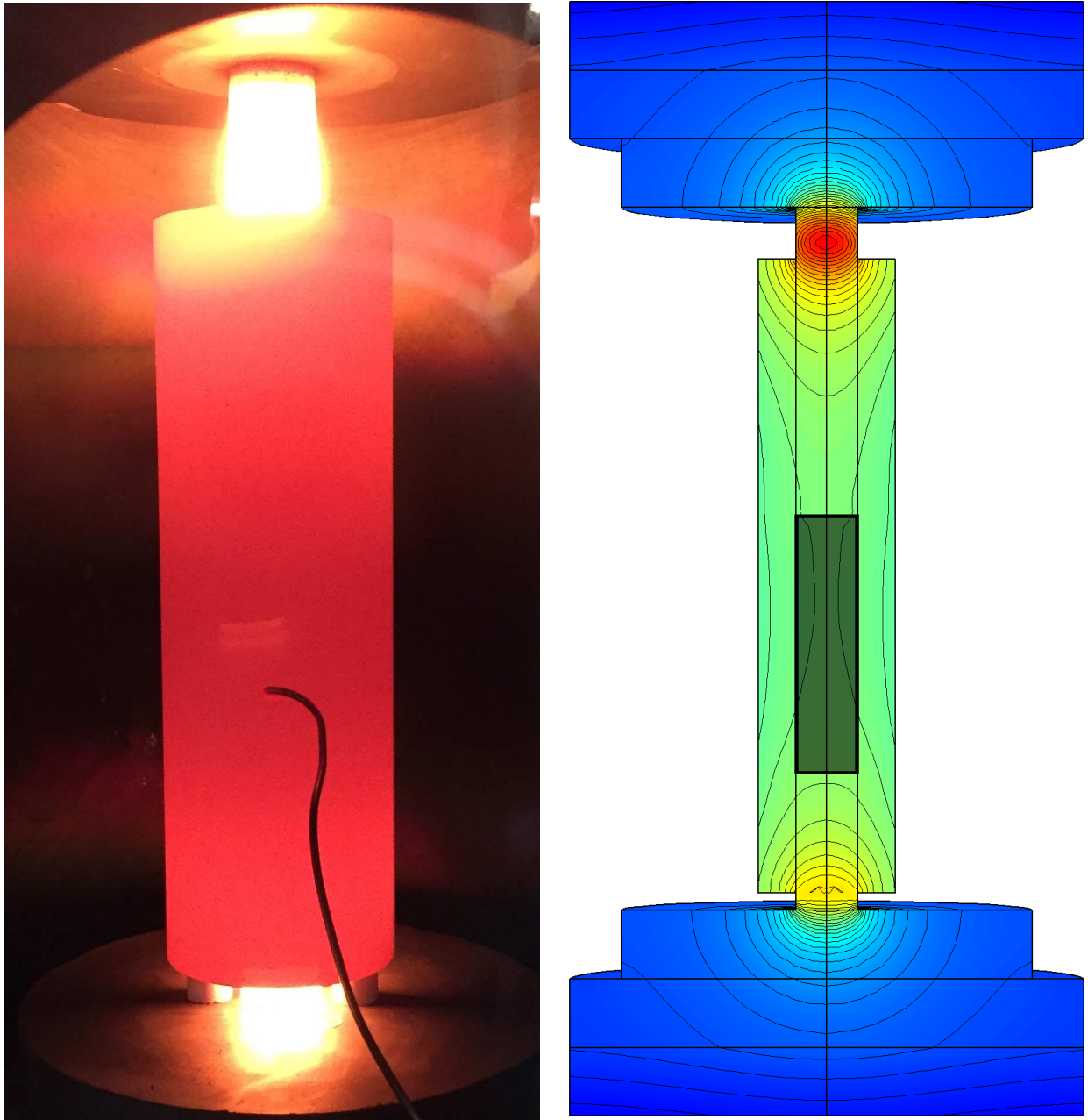


Figure 4.6: The SPS tooling of a high aspect ratio sample geometry. The COMSOL model on the right shows the sample location in the gray box as well as large diameter graphite spacers not seen in the picture on the left.

Radiation shielding

Much of the temperature distribution on the surface of the sample in figure 4.5 is due to radiation losses. The percentage of total energy lost by radiation to the SPS chamber walls be-

comes larger as the sintering temperature increases. Graphite is nearly a perfect black body emitter ($\epsilon = 0.99$), so reducing this mode of heat transfer can lower the power requirements significantly while also decreasing damage to the machine.

In an inert atmosphere, graphite felt works well as a high temperature radiation shield, as shown in figure 4.7. The felt is approximately 5 mm thick and remains well below visible temperature (600°C for a dull red color) for the duration of sintering occurring at 1300°C in a 100 mm diameter die. In this example a 25 mm diameter x 25 mm deep cylinder of material is removed from the punches to increase the heat produced.

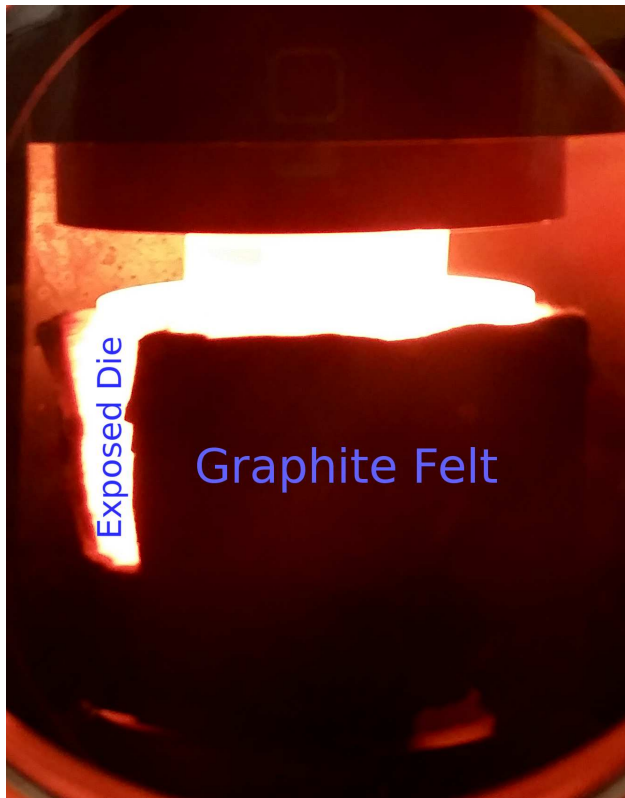


Figure 4.7: Graphite felt wrapped around die prevents radial radiation losses to the cool machine walls. This drastically reduces temperature gradients along radius of large samples

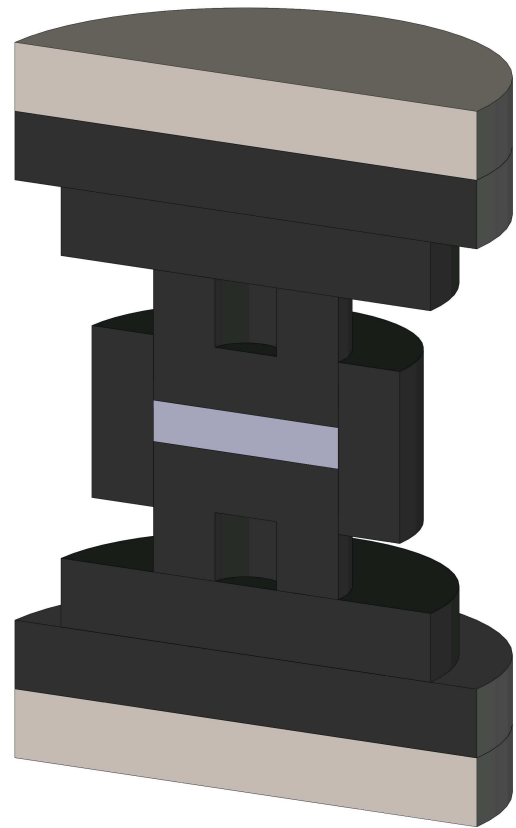


Figure 4.8: CAD model of SPS tooling. The punches have material removed to improve temperature distribution and reduce power requirement

The steady state temperature in this large diameter graphite tooling is shown in figure 4.8 with and without radiation shielding. The samples are heated with 4000 A for 1000s. The color scale is synchronized between the two models. The radiation shielding increases the maximum temperature on the sample by $200^{\circ}C$

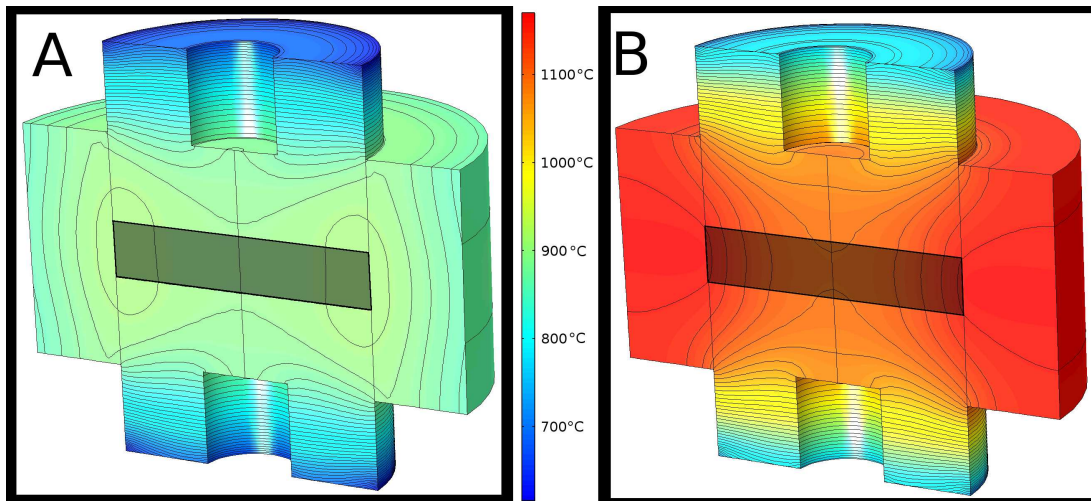


Figure 4.9: Temperature distribution on large diameter tooling with and without radiation shielding. The tooling with no radiation shielding (A) reaches a maximum temperature of $T = 907^{\circ}C$. Under the same conditions, the geometry with radiation shielding (B) reaches a maximum temperature of $T = 1170^{\circ}C$. The sample is shown by the shaded box

4.2 Continuous EFAS machine

SPS tooling scalability issues are difficult to design around and the complicated graphite designs can be very expensive. To attack the scalability problems of electric field assisted sintering from a new direction, a proof of concept Continuous-EFAS (CEFAS) machine was developed. The priority of this first iteration CEFAS machine is to develop a scalable EFAS technique with the potential to manufacture materials much faster than SPS batch processing. The preliminary design is not necessarily limited by the same fundamental scalability problems associated with SPS machines.

Graphite wheels are locally heated nearest powder body and continuously turn to heat, sinter, and extrude material. The electric field on the material is similar to SPS tooling and the materials should densify quickly using the enhanced EFAS mechanisms. The material fed into the machine is compressed to a thickness set by the fixed gap between the rollers. Figures 4.10, 4.11, 4.12 show the final design.



Figure 4.10: The CEFAS assembled on a table top. Most of the parts are recycled from past projects

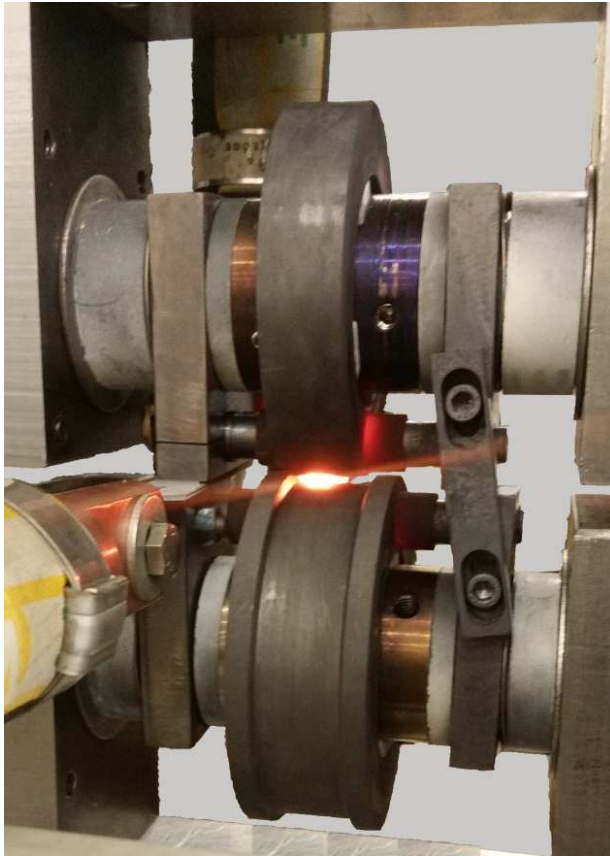


Figure 4.11: Powder pellet heated by the CEFAS machine

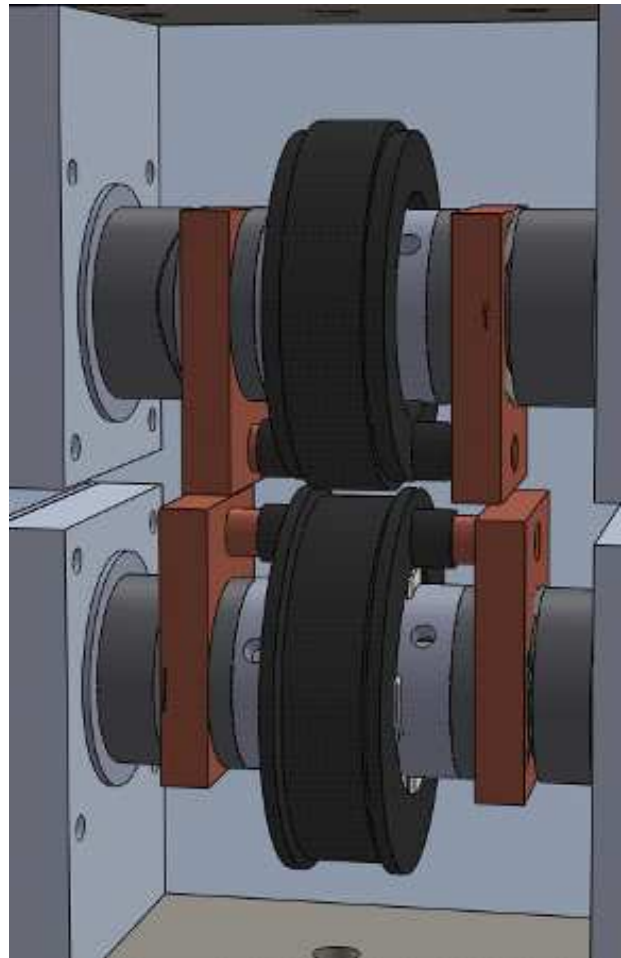


Figure 4.12: Final CAD model of the CEFAS machine

Theoretical output of CEFAS machine

The 96.5 mm diameter counter rotating wheels are powered by two motors at 10 rpm with a 60:1 gear reduction. This combination theoretically extrudes material continuously at 50.5 mm per minute. If the wheels were spaced 1.5 mm apart and the material fed in is 20 mm wide then machine could extrude $1515mm^3$ of sintered material every minute and $90900mm^3$ per hour.

For comparison, the example tooling shown in figure 4.4 reaches temperature after 1000s at 2000 A. Based on the thermal boundary conditions used in that model, the sample is cool enough

to safely remove from the machine (at or below $200^{\circ}C$) after $\approx 2000s$ due to its large size. If several sets of tooling are available and loaded very quickly then the volumetric output per hour is $69677mm^3$

To increase the volumetric output, the width and diameter of the wheels can be increased while maintaining the same thickness of graphite. The thickness of the wheel can remain constant because the alumina hub supports the load and the graphite is only in compression. To increase the size of an SPS die, the wall thickness must also increase with larger diameter samples.

4.2.1 CEFAS machine design details

Some frame components used in this design were recycled from past attempts and thus constrained the design. The overall width of the machine was limited by the aluminum frame blocks which were already machined to fit the frame rails. The labs available power supply was capable of 20 V at 500 A.

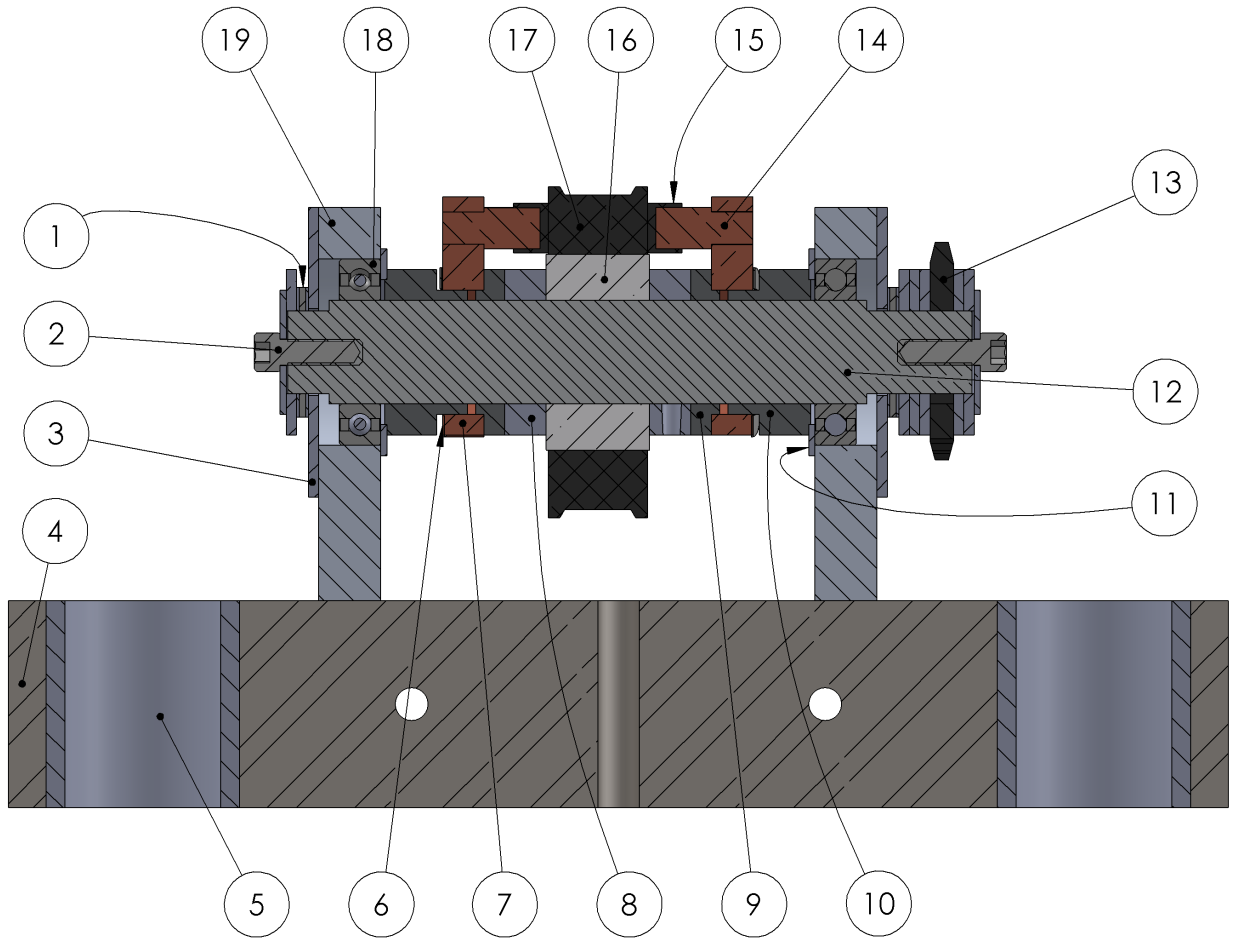


Figure 4.13: CEFAS roller cross section with identified components. The top and bottom axle assemblies are identical other than the roller wheel profile. Bubble numbers start near the top left and continue counter clockwise

Table 4.1: CEFAS axle assembly parts list

<i>Number</i>	<i>Part Name</i>	<i>Qty</i>	<i>Description</i>
1	Thrust bearing	x4	Supports load in axle direction
2	Tension screw	x4	Compresses axle assembly
3	Thrust plate	x4	Supports thrust bearing
4	Frame block	x2	Recycled aluminum block
5	Frame sleeve	x4	Adapters for recycled frame block
6	Wave spring	x4	Compresses electrode caps to wheel surface
7	Bus block	x4	Copper electrode bus bar
8	Drive dog	x4	Applies torque to alumina hub
9	Inner electrode collar	x4	Supports bus block
10	Outer electrode collar	x4	Supports bus block and wave spring
11	Thrust washer	x4	supports outer electrode collar
12	Axle	x2	Transmits torque from sprocket to drive dogs
13	Sprocket	x2	Transmits torque from motors to axle
14	Bus bar	x4	Copper extension from bus block to electrode cap
15	Electrode cap	x4	Graphite electrode cap to reduce contact wear
16	Alumina hub	x2	Transmits torque from drive dog to wheel
17	Roller wheel	x2	Graphite rollers
18	Radial bearing	x4	Transmits force from extruding material to frame
19	Bearing block	x4	Robust design aligns assembly and dissipates heat

The top and bottom axle assemblies are symmetrical. The Tension screws compressed the entire assembly together. The Thrust bearings (#1) help the assembly rotate when the wave springs are compressed. The Thrust washers (#11) are used in place of bearings due to the high temperatures expected on the inside of the bearing blocks during operation. They were coated with an aerosol boron nitride spray which acts as a high temperature lubricant.

Pin holes on the Frame block (#4) and Bearing blocks (#18) align and locate the axle assembly. The Wave spring (#6) are compressed to and press the Electrode cap (#15) to the roller wheels.

The sintered Alumina hubs (#16) have profiles sintered into them which mate to the steel Drive dogs (#8). The orientation of the profiles on both sides of the hubs was unknown until after sintering, so in order to transmit torque to both sides of the roller wheel. One Drive dog was keyed to the axle and the other was attached fixed to the axle with conical set screws. The Sprocket (#13) was also keyed to the axle.

The graphite Electrode caps (#15) are used to reduce wear compared to a copper-graphite sliding contact. The Bus bar (#14) length is controlled by the Inner electrode collar geometry to have a tight fit.

The Bus blocks were kept parallel by a non-conductive shim placed between them during operation. A flexible copper wire bridged the circuit from the lower Bus block to the upper Bus block.

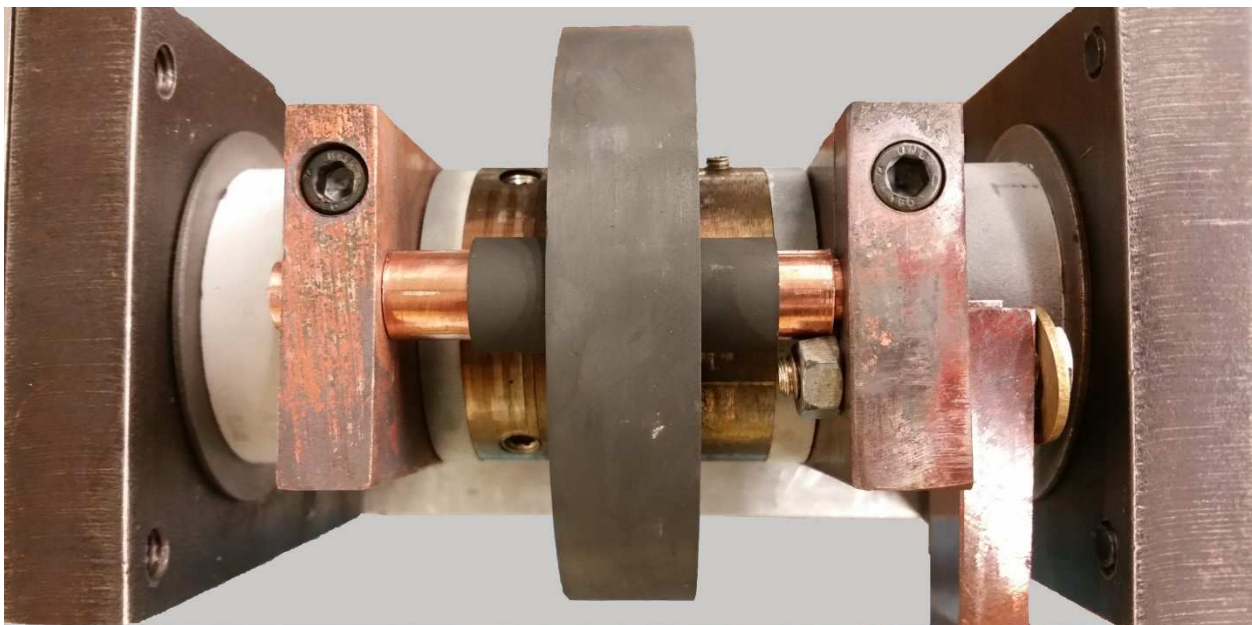


Figure 4.14: Assembled top roller

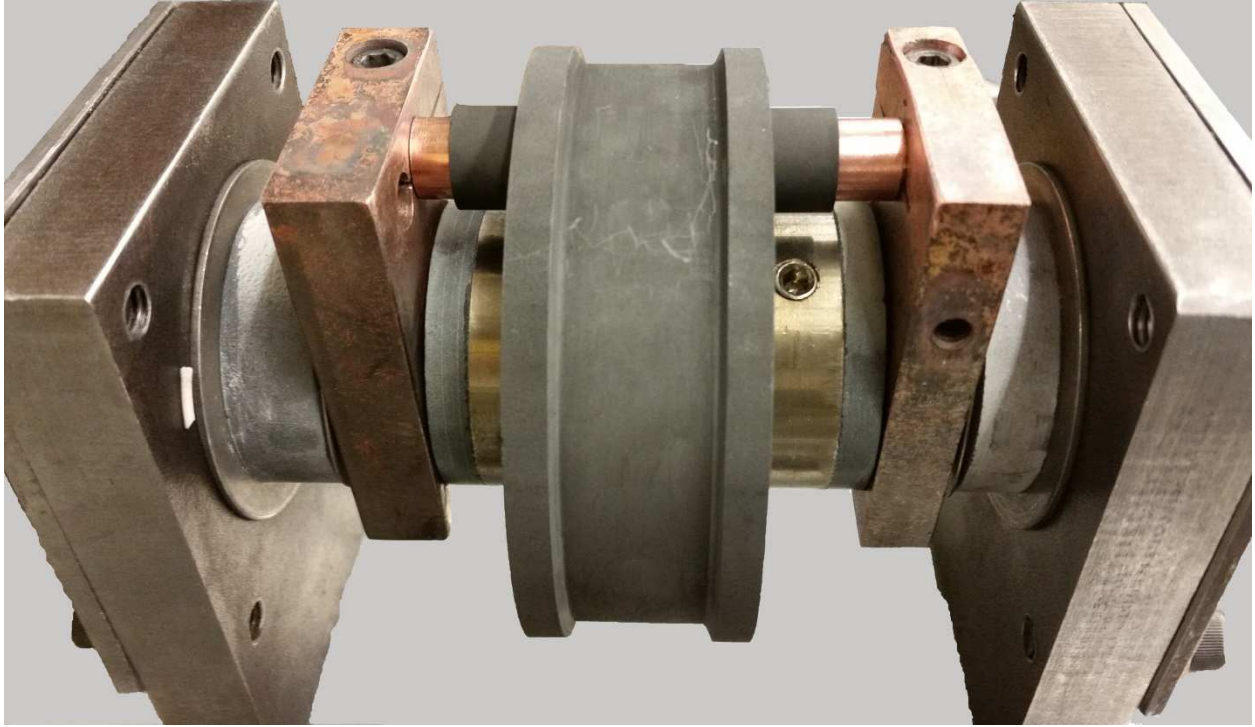


Figure 4.15: Assembled bottom roller

Current pathway

This configuration of CEFAS machine is very dependent on the electrical conductivity of the extruded material. As a comparison, the current pathway for conductive and nonconductive powders in SPS and CEFAS is shown figures 4.16 and 4.17. The red arrows are scaled relative to current density in each individual image. The gray scale represents temperature distribution. Alumina (*nonconductive*) material properties ($\approx 10^6 \Omega m$) used in the left column and steel (*conductive*) properties ($\approx 10^{-8} \Omega m$) in the right column.

The nonconductive powders produce a uniform temperature distribution on the CEFAS rollers as shown by the essentially symmetric current density plot. Alternatively, conductive powders introduce a short circuit pathway where all the current goes through the sample.

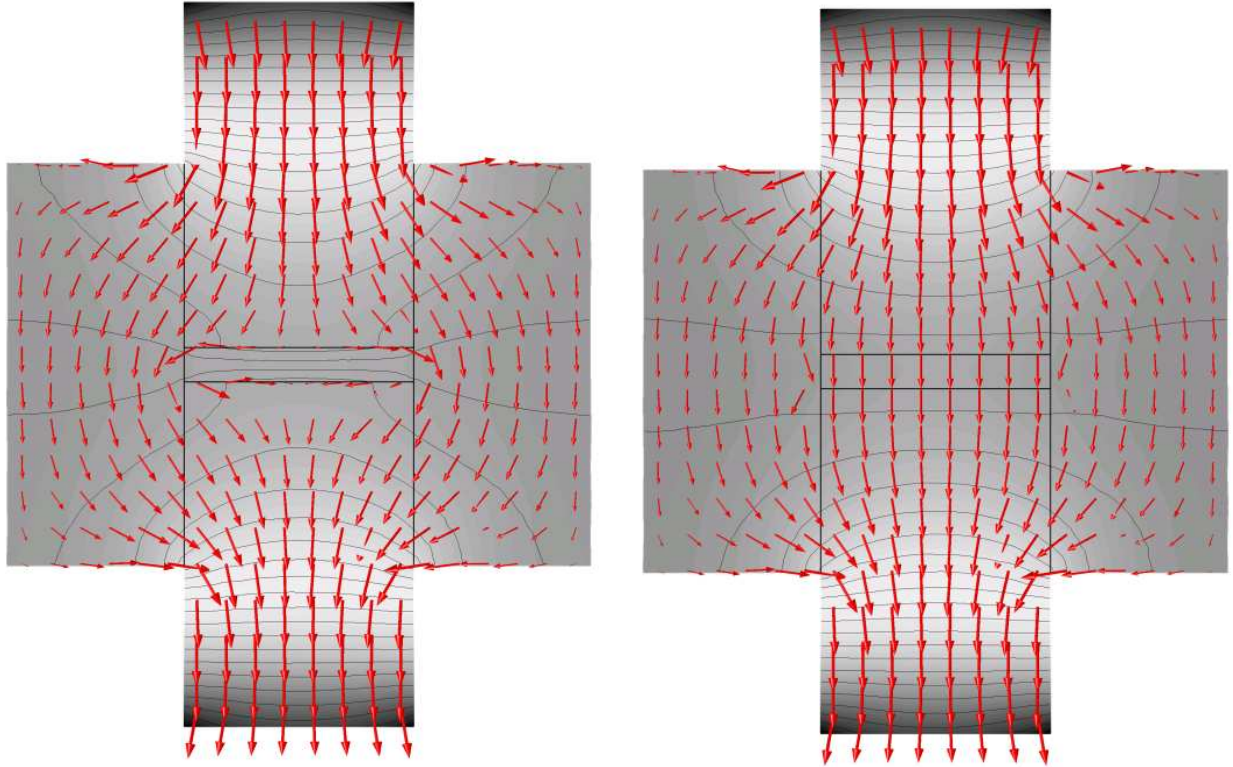


Figure 4.16: Difference in current flux through standard SPS die and punch with nonconductive (right) and conductive (left) material

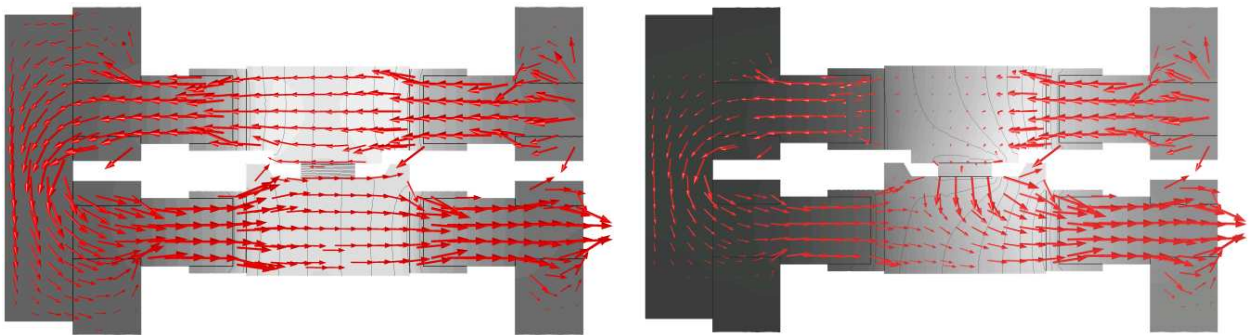


Figure 4.17: Difference in current flux through CEFAS rollers with nonconductive (right) and conductive (left) material. Notice the significant change in current pathway when the material is conductive

The electrode configuration of this CEFAS machine was thought to more closely resemble the SPS configuration. When the rollers were heated to steady state at $\approx 400A$ there was a 1 V

difference between the wheels. If the rollers are set 1.5mm apart from each other then a 6.6 V/cm electric field is produced over the material, which has been shown to enhance densification.

4.2.2 Critical components

Graphite rollers

Isolating the electrical power from the rest of the machine was a primary design consideration. The CEFAS machine design pivoted around how the wheels could be Joule heated while electrically isolated from the supporting steel axle and torque transmission. The final design was made to support extrusion pressures, withstand high temperatures, transmit torque, and fit into the modular axle assembly. The rollers also can be easily removed and replaced.

The wheels were made from a SPS die in a processing step using the tooling shown in figure 4.19. To electrically isolate the Joule heated graphite from the machine alumina powder was sintered as a hub. Alumina is extremely non conductive and capable of high temperatures. The hub was sintered to 93% density which helped reduce thermal conductivity while maintaining strength.

There is a slight difference in thermal expansion between alumina ($\sim 8.1 \cdot 10^{-6}/K$) and graphite ($\sim 7.8 \cdot 10^{-6}/K$). To prevent the sintered alumina from separating from the graphite after cooling, grooves were cut in the ID of the die such that powder would infill during sintering. The tooling was slowly cooled by manually reducing power to the SPS machine over the course of several hours to prevent thermal stresses from cracking the slightly porous alumina.

The die was then machined to the desired thickness and diameter, and a groove was added to the lower roller. The SPS die with the sintered hub is shown in figure 4.18.

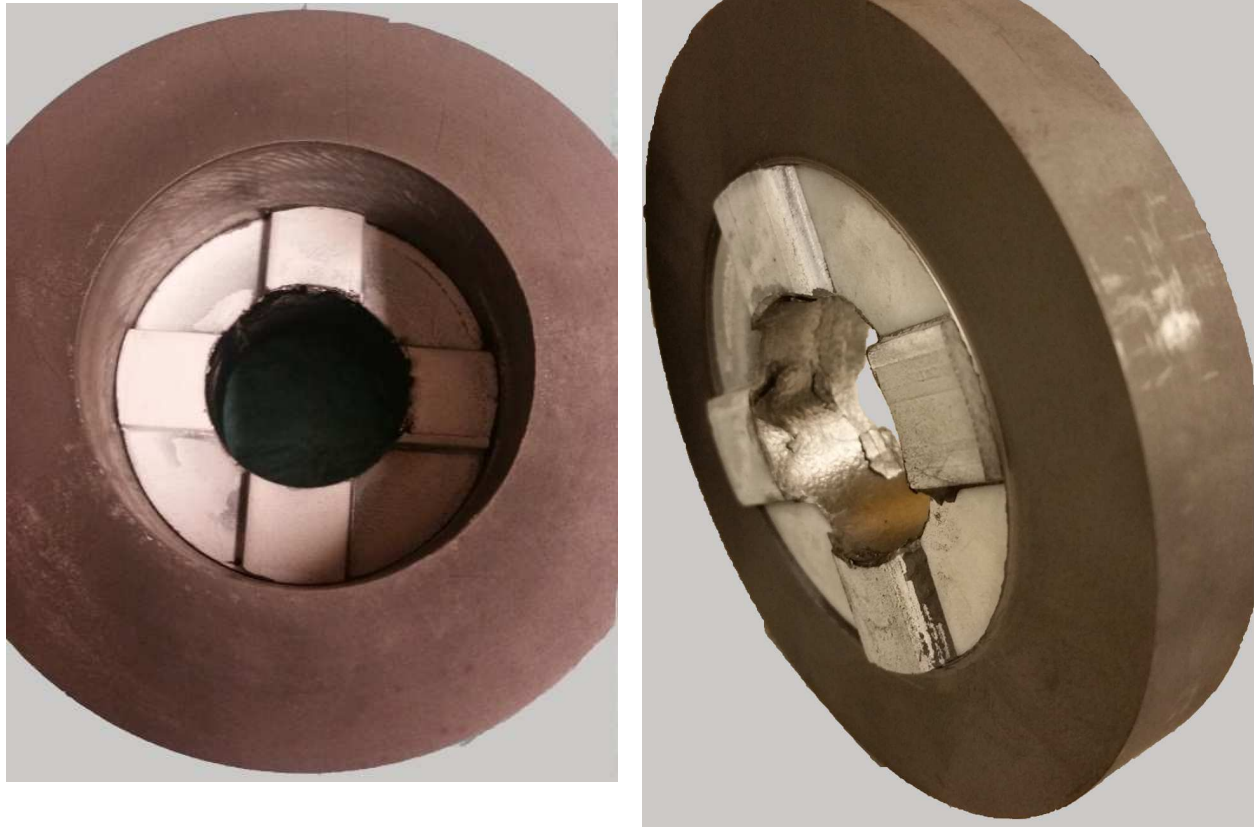


Figure 4.18: Upper CEFAS roller wheel before and after machining. The hub thickness was controlled by the SPS tooling and the graphite was removed to be flush with its thickness.

The punches shown in red and yellow in 4.19 were machined to a tight slip fit with the ID of the die. The inverted drive dog profile was cut into the surface of the graphite punches contacting the powder. The punches were coated with a high temperature release spray so they would not bond to the alumina powder. Chamfers on the inverted drive dog profile in the punches ensured the matching steel would seat flush to the ceramic. The graphite plug shown in green prevented displacement beyond the desired hub thickness.

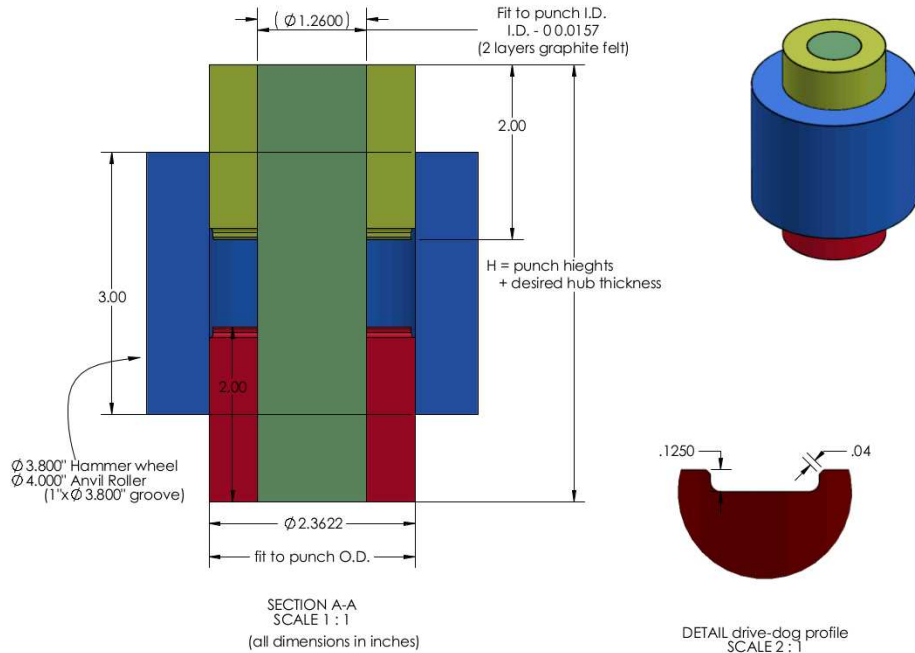


Figure 4.19: SPS tooling used to sinter the alumina hub inside the graphite rollers.

Electrodes

The electrodes delivered current to the rotating graphite wheels in the local area around the extruding material. This also created $\approx 2.5V/cm$ electric field over the 1.5mm thickness. The electric field produced over the sample (assuming the material is non-conductive) was mostly due to the sliding contact resistance of the electrodes and the voltage drop through the graphite. The wheels must be the same thickness in order to reach the same temperature.

The current pathway through the machine is symmetrical about the roller wheels and between top and bottom axle assemblies: Bus block \rightarrow Bus rod \rightarrow Electrode cap \rightarrow Roller wheel \rightarrow Electrode cap \rightarrow Bus rod \rightarrow Bus block \rightarrow etc...

A cross section of the final CEFAS electrode design is shown in figure 4.13 and the assembled rollers shown in figure 4.14 and 4.15.

The bus blocks are held in place by the Inner and Outer electrode collar. These were made from a machinable alumina-silicate in a green state. Typically this material is machined to a desired geometry then free sintered to full density. However, the material in its green state has low electrical and thermal conductivity and was capable of operating in the conditions required so it was left as is.

At operating temperatures, the electrodes had a tendency to separate from the graphite rollers. The Wave springs between the Bus blocks and the Outer electrode collar pressed the electrodes to the wheels regardless of this expansion. A gap between the Inner and Outer electrode collars allowed for this expansion. The Outer electrode collars were designed to compress the Wave springs so they would apply ≈ 100 kPa at room temperature, which is optimal balance between conductivity and friction of sliding contacts [36].

4.3 Conclusion and future improvements

Electric field assisted sintering can improve the material properties of sintered ceramics and Spark Plasma Sintering is a very useful tool for many applications. Constraining the Joule heat and limiting the heat flow nearest the material can help manufacturability, but these changes can be expensive and complicated. The continuous EFAS machine developed here may offer an alternative solution to some of the fundamental issues limiting SPS samples sizes.

Specific control variables for future CEFAS iterations should include: roller speed, automated power supply control, water cooled axles, and the surrounding atmosphere. The steady state temperature produced in each roller is dependent upon the roller thickness, so differing roller thicknesses could produce temperature gradients. The electrode circuit pathway could be modified to prevent the material acting as a short circuit.

Ideally, the CEFAS process would exist in a steady state where the pre-heated material is just conductive enough to conduct the current. This would be similar to Flash sintering, and could extrude materials very quickly. The electric field between the rollers would be tuned to the roller RPM and material conductivity.

Independent roller speed could impart a shear gradient on the material and densify one side faster than the other. Most of the cooling in this proof of concept machine was from the water cooled electric cables and convection to the air in the lab. Future iterations must dissipate the high temperatures to a water cooling loop either in the frame or through the axle. Water cooled axles would thermally isolate the machine components in a manner very similar to the SPS process.

The alumina hub sintered into the graphite die shown in 4.11 locates directly onto the steel axle. Stresses from the extrusion process are carried from the graphite wheel to radial ball bearings via the contact between the alumina hub and steel axle. That contact interface should be a reasonably tight slip once accommodating thermal expansion. To create a perfect slip fit between the axle and wheel, a graphite core should be sintered into the alumina powder prior to sintering. The core would be larger than the axle and have grooves in its OD that would fill with powder during sintering. Upon cooling, the graphite core could be bored out to a precise tolerance to match the steel axle OD.

The wheels produced for this CEFAS machine were cut to different thicknesses. The voltage drop in the thicker wheel is larger than the thinner wheel and therefore it becomes hotter. Future iterations of the CEFAS machine could have many wheels on hand to either extrude materials isothermally or with a temperature gradient to produce FGMs.

Bibliography

- [1] J. D. Hansen, R. P. Rusin, M. H. Teng, and D. L. Johnson, “Combined-Stage Sintering Model,” *Journal of the American Ceramic Society*, vol. 75, no. 5, pp. 1129–1135, 1992.
- [2] P. Drescher and H. Seitz, “Processability of an amorphous metal alloy powder by electron beam melting,” *RTeJournal - Fachforum für Rapid Technologie*, vol. 2015, no. 1, 2015.
- [3] H. Mehrer, *Diffusion in Solids: Fundamentals, Methods, Materials, Diffusion-Controlled Processes*. Springer Series in Solid-State Sciences, Berlin, Heidelberg: Springer, 2007.
- [4] H. Wang, Z. Z. Fang, and K. S. Hwang, “Kinetics of Initial Coarsening During Sintering of Nanosized Powders,” *Metallurgical and Materials Transactions A*, vol. 42, pp. 3534–3542, June 2011.
- [5] S. L. Dole, S. Prochazka, and R. H. Doremus, “Microstructural Coarsening During Sintering of Boron Carbide,” *Journal of American Ceramic Society*, vol. 72, pp. 958 – 966, Oct. 1988.
- [6] H. Su and D. L. Johnson, “Master Sintering Curve: A Practical Approach to Sintering,” *Journal of the American Ceramic Society*, vol. 79, no. 12, pp. 3211–3217, 1996.
- [7] K. An and D. L. Johnson, “The pressure-assisted master sintering surface,” *Journal of Materials Science*, vol. 37, pp. 4555–4559, Nov. 2002.
- [8] O. Guillon and J. Langer, “Master sintering curve applied to the Field-Assisted Sintering Technique,” *Journal of Materials Science*, vol. 45, pp. 5191–5195, Oct. 2010.

- [9] E. A. Olevsky, S. Kandukuri, and L. Froyen, "Consolidation enhancement in spark-plasma sintering: Impact of high heating rates," *Journal of Applied Physics*, vol. 102, no. 11, p. 114913, 2007.
- [10] T. B. Holland, T. B. Tran, D. V. Quach, U. Anselmi-Tamburini, J. R. Groza, and A. K. Mukherjee, "Athermal and thermal mechanisms of sintering at high heating rates in the presence and absence of an externally applied field," *Journal of the European Ceramic Society*, vol. 32, pp. 3675–3683, Nov. 2012.
- [11] S. Ghosh, A. H. Chokshi, P. Lee, and R. Raj, "A Huge Effect of Weak dc Electrical Fields on Grain Growth in Zirconia," *Journal of the American Ceramic Society*, vol. 92, pp. 1856–1859, Aug. 2009.
- [12] J. W. Jeong, J. H. Han, and D. Y. Kim, "Effect of electric field on the migration of grain boundaries in alumina," *Journal of the American Ceramic Society*, vol. 83, no. 4, pp. 915–918, 2000.
- [13] K. J. Mackenzie and M. J. Ryan, "Effect of electric fields on solid-state reactions between oxides," *Journal of Materials Science*, vol. 16, no. 3, pp. 579–588, 1981.
- [14] D. M. Hulbert, D. Jiang, U. Anselmi-Tamburini, C. Unuvar, and A. K. Mukherjee, "Experiments and modeling of spark plasma sintered, functionally graded boron carbide–aluminum composites," *Materials Science and Engineering: A*, vol. 488, pp. 333–338, Aug. 2008.
- [15] D. M. Hulbert, D. Jiang, U. Anselmi-Tamburini, C. Unuvar, and A. K. Mukherjee, "Experiments and modeling of spark plasma sintered, functionally graded boron carbide–aluminum composites," *Materials Science and Engineering: A*, vol. 488, pp. 333–338, Aug. 2008.

- minum composites,” *Materials Science and Engineering: A*, vol. 488, pp. 333–338, Aug. 2008.
- [16] R. Raj and A. Rehman, “Can Die Configuration Influence Field-Assisted Sintering of Oxides in the SPS Process?,” *Journal of the American Ceramic Society*, vol. 96, no. 12, pp. 3697–3700, 2013.
- [17] E. A. Olevsky, W. L. Bradbury, C. D. Haines, D. G. Martin, and D. Kapoor, “Fundamental Aspects of Spark Plasma Sintering: I. Experimental Analysis of Scalability,” *Journal of the American Ceramic Society*, 2012.
- [18] Y. Song, Y. Li, Z. Zhou, Y. Lai, and Y. Ye, “A multi-field coupled FEM model for one-step-forming process of spark plasma sintering considering local densification of powder material,” *Journal of Materials Science*, vol. 46, pp. 5645–5656, Apr. 2011.
- [19] S. Wei, Z.-H. Zhang, X.-B. Shen, F.-C. Wang, M.-Y. Sun, R. Yang, and S.-K. Lee, “Simulation of temperature and stress distributions in functionally graded materials synthesized by a spark plasma sintering process,” *Computational Materials Science*, vol. 60, pp. 168–175, July 2012.
- [20] X. Wei, D. Giuntini, A. L. Maximenko, C. D. Haines, and E. A. Olevsky, “Experimental Investigation of Electric Contact Resistance in Spark Plasma Sintering Tooling Setup,” *Journal of the American Ceramic Society*, pp. n/a–n/a, May 2015.
- [21] K. Vanmeensel, A. Laptev, J. Hennicke, J. Vleugels, and O. Van der Biest, “Modelling of the temperature distribution during field assisted sintering,” *Acta Materialia*, vol. 53, pp. 4379–4388, Sept. 2005.

- [22] R. Raj and A. Rehman, "Can Die Configuration Influence Field-Assisted Sintering of Oxides in the SPS Process?," *Journal of the American Ceramic Society*, vol. 96, no. 12, pp. 3697–3700, 2013.
- [23] X. Wang, S. Casolco, G. Xu, and J. Garay, "Finite element modeling of electric current-activated sintering: The effect of coupled electrical potential, temperature and stress," *Acta Materialia*, vol. 55, pp. 3611–3622, June 2007.
- [24] U. Anselmi-Tamburini, J. E. Garay, and Z. A. Munir, "Fundamental investigations on the spark plasma sintering/synthesis process III. Current effect on reactivity," *Materials Science & Engineering A*, vol. 407, no. 1-2, pp. 24–30, 2005.
- [25] A. Abbasian, Mohammad Rahimipour, and Zohreh Hamnabard, "Activation Energies for Initial and Intermediate Stage Sintering of Li_2TiO_3 Determined by a Two-Stage Master Sintering Curve Approach," *Advances in Engineering Mechanics and Materials ISBN: 978-1-61804-241-5 291*, pp. 291–296, 2014.
- [26] M. Mazaheri, A. Simchi, M. Dourandish, and F. Golestani-Fard, "Master sintering curves of a nanoscale 3y-TZP powder compacts," *Ceramics International*, vol. 35, pp. 547–554, Mar. 2009.
- [27] K. G. Ewsuk, D. T. Ellerby, and C. B. DiAntonio, "Analysis of Nanocrystalline and Microcrystalline ZnO Sintering Using Master Sintering Curves," *Journal of the American Ceramic Society*, vol. 89, no. 6, pp. 2003–2009, 2006.
- [28] V. Pouchly and K. Maca, "curve: A practical approach to its construction," *Science of Sintering*, vol. 42, no. 1, pp. 25–32, 2010.

- [29] L. Wang, V. Pouchly, K. Maca, Z. Shen, and Y. Xiong, “Intensive particle rearrangement in the early stage of spark plasma sintering process,” *Journal of Asian Ceramic Societies*, vol. 3, no. 2, pp. 183 – 187, 2015.
- [30] P. S. H. F. Raether, “Investigation of sintering mechanisms of alumina using kinetic field and master sintering diagrams,” *Journal of the European Ceramic Society*, vol. 29, no. 11, pp. 2225 – 2234, 2009.
- [31] L. Wang, V. Pouchly, K. Maca, Z. Shen, and Y. Xiong, “Intensive particle rearrangement in the early stage of spark plasma sintering process,” *Journal of Asian Ceramic Societies*, vol. 3, pp. 183–187, June 2015.
- [32] D. V. Quach, H. Avila-Paredes, S. Kim, M. Martin, and Z. A. Munir, “Pressure effects and grain growth kinetics in the consolidation of nanostructured fully stabilized zirconia by pulsed electric current sintering,” *Acta Materialia*, vol. 58, no. 15, pp. 5022–5030, 2010.
- [33] G. Randall, *Sintering Theory and Practice*. Wiley-Interscience, 1996.
- [34] K. M. H. Y. K. H. Haibin Zhang, Byung-Nam Kim and Y. Sakka, “Effect of sintering temperature on optical properties and microstructure of translucent zirconia prepared by high-pressure spark plasma sintering,” *Sci Technol Adv Mater*, vol. 12, no. 5, 2011.
- [35] D. Giuntini, J. Raethel, M. Herrmann, A. Michaelis, and E. A. Olevsky, “Advancement of tooling for spark plasma sintering,” *Journal of the American Ceramic Society*, vol. 98, no. 11, pp. 3529–3537, 2015.

- [36] I. Yasar, A. Canakci, and F. Arslan, “The effect of brush spring pressure on the wear behaviour of copper-graphite brushes with electrical current,” *Tribology International*, vol. 40, pp. 1381–1386, Sept. 2007.

Appendix A

Master sintering curve MATLAB script

The user inputs a range of Q_{MSC} , the density range, low temperature cut off, and cooling curves. The main program is "error_reduction_MSC.m" which formats data from user input data. The data goes into three matrix: dens, temp, and time where each column is from a different data set. Due to the numerical approach, the shortest dataset needs to be the first dataset column in each of the three matrix. Density is in relative percent, time is in seconds and the temperature in $^{\circ}C$.

Main: error_reduction_MSC.m

```
1 clearvars -except time temp dens cooling comsolat
2 clf
3
4 n=40; %number of iterations between min and max
   Q_msc
5 Qmax=120*10^3; %maximum activation energy
6 Qmin=60*10^3; %minimum activation energy
7 N=size(dens,2); %number of heating schedules
8 maxD=97; %Maximum denisty
9 minD=50; %minimum denisty
10 minT=900+273; %minimum temperature where volume and
   grain boundary diffusion occur
11
12 lowT_theta=zeros(n,1);
13 %MRS=zeros(n,1);
14
15 for loop=1:n
16     Q(loop)=Qmin+(Qmax-Qmin)/n*loop;
17     for i=1:N
18         [reldens, theta, lowT_theta(loop)]=MSC(Q(loop),minD,
19         maxD,minT,dens(:,i),time(:,i),temp(:,i)+273);
20         data(i)=struct('D',reldens,'T',log(theta));
21     end
22     [MRS(loop), avg_theta, sum_theta_error]=MRS_MSC_FUNCTION(
23     data,minD,maxD);
24 %% Generate MSC curve
25     if loop == 1 %Compare the error from Q(loop) to
   the saved value
```

```

26     msc_curve(:,1)=avg_theta;      %initial value of theta
        value at the best Q_msc
27     msc_curve(:,2)=data(1).D;      %density of reference
        data set
28     weighted_err=sum_theta_error;
29     elseif MRS(loop) < MRS(loop-1)
30     msc_curve(:,1)=avg_theta;      %average theta value at
        the best Q_msc
31     weighted_err=sum_theta_error;  %weighted error sum
32     end
33
34 end
35
36 [~,idx]=min(MRS);
37 Q_msc=Q(idx);
38
39 %%
40
41 dTdt=100:10:150;
42
43 gmsc=zeros(size(msc_curve,1),4);
44 gmsc_data(length(dTdt))=struct('theta',[],'dens',[],'time'
        ,[],'temp',[],'adj_dens',[]);
45
46 for i=1:length(dTdt)
47
48     Tf=1400+273;
49     Ts=0+273;
50     t_hold=10; %min
51     t_ramp=(Tf-Ts)/dTdt(i); %min
52     t_study=(t_ramp+t_hold)*60;
53     gtemp(1)=Ts;
54     gtime=linspace(0,t_study,5000);
55     for j=2:5000
56         gtemp(j)=dTdt(i)/60*gtime(j)+gtemp(1);
57         if gtemp(j) >= Tf
58             gtemp(j)=Tf;
59         end
60     end
61
62     %[gmsc,adj_dens(:,i)]=generate_densityMSC(msc_curve, Q_msc,
        minT, comsoldat(:,1), comsoldat(:,1+i)+273,cooling);
63     [gmsc,intr_gmsc]=generate_densityMSC(msc_curve, Q_msc, minT,
        gtime, gtemp, cooling);
64

```

```

65 gmsc_data(i).time=gmsc(:,1);
66 gmsc_data(i).temp=gmsc(:,2)-273;
67 gmsc_data(i).theta=gmsc(:,3);
68 gmsc_data(i).dens=gmsc(:,4);
69
70 intr_gmsc_data(i).time=intr_gmsc(:,1);
71 intr_gmsc_data(i).temp=intr_gmsc(:,2)-273;
72 intr_gmsc_data(i).dens=intr_gmsc(:,3);
73
74 figure(2)
75 hold on
76 plot(gmsc_data(i).time(:)/60,gmsc_data(i).dens(:),'.-');
77 %scatter(intr_gmsc_data(i).time(:),intr_gmsc_data(i).dens(:))
78 ;
79 %xlabel('temp')
80
81 ylabel('density (%)')
82 end
83 %plot(time(:,1),dens(:,1),'r',time(:,2),dens(:,2),'b',time
84 (:,3),dens(:,3),'g')
85 hold off

```

Function: MSC.m

```
1 function [MSC_dens , summed_theta , lowT_theta ] = MSC(Q, minD , maxD ,
    minT , dens , time , temp )
2 %Time should be in seconds
3 %temperature should be in Kelvin
4
5 for i=1:length(dens)
6     if dens(i) >= minD && dens(i)~=0;
7         %nothing
8     elseif dens(i)~=0
9         idx_dens_start=i;          %find the last density under
    the limit
10    end
11
12    if dens(i) >= maxD && dens(i)~=0;
13        idx_dens_stop=i; %find the first density over the
    limit
14        break;
15    end
16 end
17
18 %% %%%%%%%%%%%
19 % Low temperature contribution to the sum %
20 %% %%%%%%%%%%%
21
22 [~, idx_Tt_start]=min(abs(temp(1:idx_dens_start)-minT));
23
24 lowT_MSC_temp=temp(idx_Tt_start:idx_dens_start);
25 lowT_MSC_time=time(idx_Tt_start:idx_dens_start);
26
27 lowT_theta = THETA_INTEGRAL(Q, lowT_MSC_time , lowT_MSC_temp);
28 lowT_theta=lowT_theta(end);          %integral sum
29
30 %% ^^^^^^^^^^^^^^^^^^^^^^^^^^^^^^^^^^^^^^^^^^^^^^^^^^^^^^^^^^^^^%%
31
32 MSC_dens=dens(idx_dens_start:idx_dens_stop);
33 MSC_temp=temp(idx_dens_start:idx_dens_stop);
34 MSC_time=time(idx_dens_start:idx_dens_stop);
35
36 summed_theta=THETA_INTEGRAL(Q, MSC_time , MSC_temp)+lowT_theta;
37
38 return
```

Function: MRS_MSC_FUNCTION.m

```
1 function [ MRS_sum, avg_theta , sum_theta_error ] =
   MRS_MSC_FUNCTION( data , minD , maxD)
2 %input data structure of the heating schedules with density
   This section
3 %calculates the MRS between heating schedules length of 1st
   data struct
4 %must the shortest of all the sintering schedules the
   function returns the
5 %total MRS and the average theta at each density
6
7 maxD=maxD/100;
8 minD=minD/100;
9
10 N=size( data ,2); %number of heating schedules
11 theta_mat=zeros( size( data(1) .D,1) ,N);
12 theta_error=zeros( size( data(1) .D,1) ,N);
13
14 %% find index of the theta value that matches reference theta
   value at each density
15 for row=1:size( data(1) .D,1) %length of the first density
   struct vector
16     theta_mat(row ,1)=data(1) .T(row);
17     for col=2:N
18         [~, idx_dens_match]=min( abs( data( col) .D-data(1) .D(row))
   );
19         theta_mat(row , col)=data( col) .T( idx_dens_match );
20     end
21 end
22 %% difference of each theta value from the average theta
   value at that density
23 avg_theta=mean( theta_mat ,2);
24
25 for col=1:N
26     theta_error( : , col)=(theta_mat( : , col) ./ avg_theta -1).^2/N;
27 end
28
29
30 sum_theta_error=sum( theta_error ,2); %add together weighted
   errors
31 MRS_sum=sqrt( 1/(maxD-minD) * trapz( data(1) .D, sum_theta_error) );
32 end
```

Function: generate_densityMSC.m

```
1
2 function [gmsc, adj_gmsc] = generate_densityMSC(msc_data, Q_msc
   , minT, time, temp, cooling)
3 %%msc_data is nx2 MSC matrix. Column #1 is log(theta) Column#2
   is density
4 %% generate_densityMSC() returns generated master stinerig
   curve data
5 %% "gmsc" data in an nx4 matrix: [theta, density, time, temp]
6
7     n=length(msc_data);           %number of elements in
   MSC
8     theta_start=msc_data(1,1);    %starting log(theta)
   value of MSC
9
10    integral_theta=THETA_INTEGRAL(Q_msc,time,temp);
11    log_integral_theta=log(integral_theta);
12
13 %%    LOW TEMPERATURE THETA CONTRIBUTION
14    [~,idx_T_low]=min(abs(temp-minT));
15    [~,idx_MSC_start]=min(abs(log_integral_theta-theta_start)
   );
16
17    lowT_MSC_temp=temp(idx_T_low:idx_MSC_start);
18    lowT_MSC_time=time(idx_T_low:idx_MSC_start);
19
20    lowT_theta=THETA_INTEGRAL(Q_msc,lowT_MSC_time,
   lowT_MSC_temp);
21    lowT_theta=lowT_theta(end);
22 %%    Create the MSC curve
23
24    [~,idx_MSC_stop]=min(abs(log_integral_theta-msc_data(n,1)
   ));
25
26 %%build gmsc time and temperature columns:
27    gmsc(:,3)=linspace(time(idx_MSC_start),time(idx_MSC_stop)
   ,n);
28    gmsc(:,4)=interp1(time(idx_MSC_start:idx_MSC_stop),temp(
   idx_MSC_start:idx_MSC_stop),gmsc(:,3));
29
30 %%Build over the applicable density range with low T theta
   contribution
```

```

31     gmsc(:,1)=log(THETA_INTEGRAL(Q_msc ,gmsc(:,3),gmsc(:,4))+
        lowT_theta);
32
33 %Fit density from this gmsc theta to the MSC theta
34     for i=1:n
35         [~,idx]=min(abs(gmsc(i,1)-msc_data(:,1)));
36         gmsc(i,2)=msc_data(idx,2);
37     end
38
39 %% adjust densification curves to include Cooling
        contribution.
40
41     adj_dens=zeros(size(msc_data,1),1);
42     adj_theta=zeros(size(msc_data,1),1);
43
44     for i=1:size(msc_data,1)
45         idx_theta_interrupt=i;
46         Tmsc=exp(msc_data(idx_theta_interrupt,1));           %theta
        at which to interrupt heating
47         [~,idx_T_low]=min(abs(cooling(:,2)-minT));
48
49         [~,hT_idx_interupt]=min(abs(integral_theta-Tmsc)); %index
        to interrupt heating schedule
50         hT=integral_theta(hT_idx_interupt);
51
52         [~,cool_idx_start]=min(abs(temp(hT_idx_interupt)-cooling
        (:,2))); %index matching interrupt temperature
53         t_cool=cooling(cool_idx_start:idx_T_low,1)+time(
        hT_idx_interupt)-cool_idx_start;           % offset
        cooling profile time to interrupt time
54         cT=THETA_INTEGRAL(82750,t_cool,cooling(cool_idx_start:
        idx_T_low,2));
55         cT=cT(end);
56
57         adj_theta(i)=(log(cT+hT));           %total theta value for
        heating and cooling
58         [~,idx]=min(abs(msc_data(:,1)-adj_theta(i)));       %index
        where adjust theta matches MSC
59         adj_dens(i)=msc_data(idx,2);
60     end
61
62     adj_gmsc(:,1)=adj_dens;
63     end

```

Function: THETA_INTEGRAL.m

```
1 function [ integral_theta ] = THETA_INTEGRAL( Q, time , temp)
2 %calculate_theta_FCN calculate and return theta integral
3 % time should be in seconds , temperature should be in
   kelvin , Q should be
4 % in J/mol K
5
6 n=length(temp);
7 eta=zeros(n,1);
8 integral_theta=zeros(n,1);
9 integral_theta(1)=0;
10
11 for i=1:n
12     eta(i)=1/(temp(i))*exp(-Q/(8.314*(temp(i))));
13     if i ~= 1
14         integral_theta(i)=integral_theta(i-1)+(eta(i-1)+eta(i)
           )/2*(time(i)-time(i-1));
15     end
16 end
17
18 end
```

Appendix B

Thermocouple measurement

In some SOD punches, the cross-sectional area is smaller in the horizontal plane inside the alumina sleeve than on the hot side punch - die interface. This produces a hot spot inside the punch that the axial thermocouple traverses. Heat flux from the hot spot into the tungsten wire may produce error, as well as the hot spots often being very near the melting temperature of the wire. Also the ceramic insulators on the type-C thermocouples would melt, causing a short.

To avoid this problem some FGM samples were sintered using a thermocouple drilled radially into the hot side punch. The two configurations are shown in figure B.1.

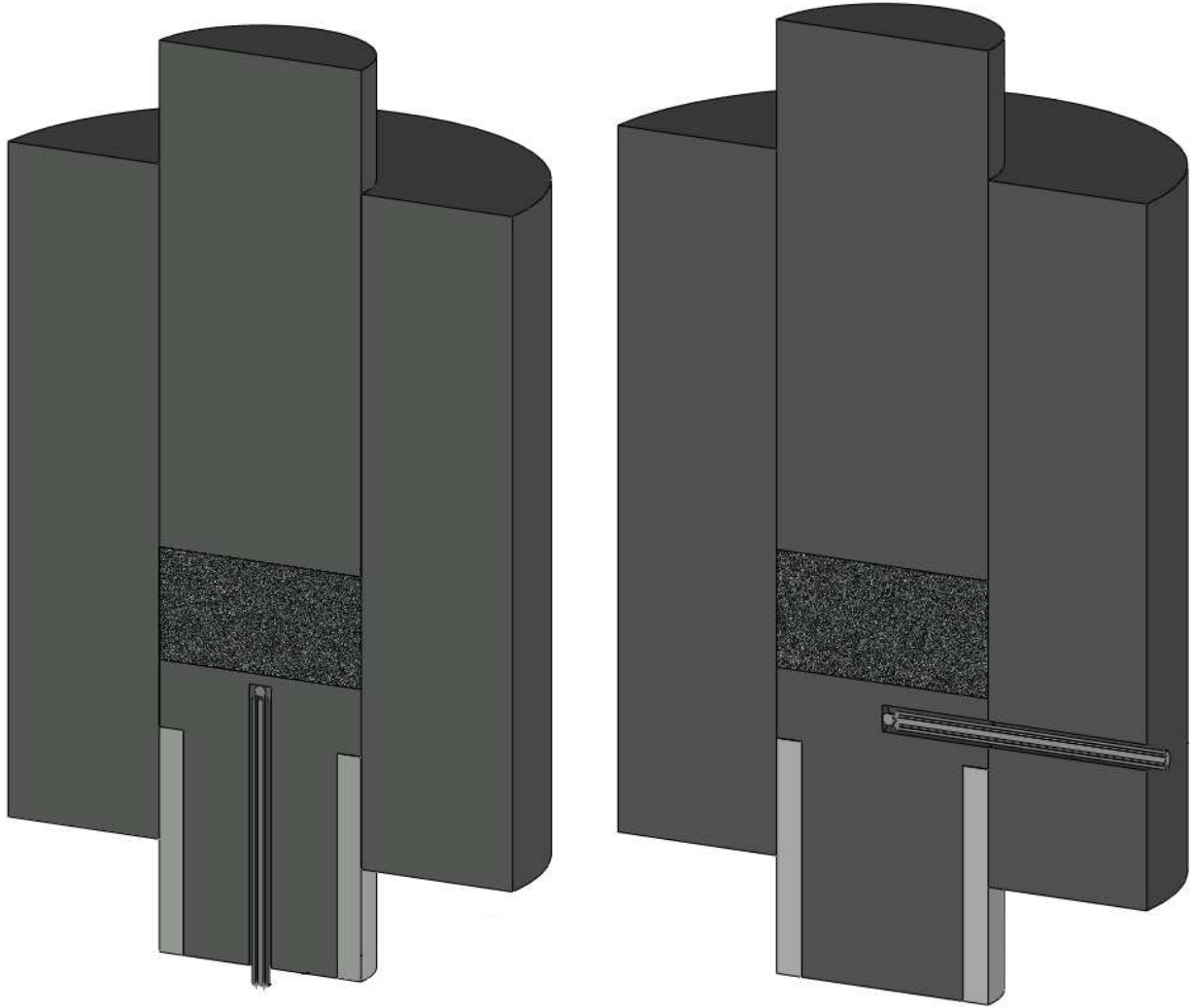


Figure B.1: Axial (left) and radial (right) thermocouple placement

Accurately locating the radial thermocouple hole is critical. It must be close to the powder (within 2 mm of the surface) to minimize error while far enough away to maintain structural integrity. The tooling was assembled with the powder and loaded in a press with the drill jig around the SOD punch shown in figure B.2. The jig nominally aligns the thermocouple hole for a 6mm SOD punch. Shims allowed the jig to be compatible with a wide range of SOD punches.



Figure B.2: Radial thermocouple drill jig

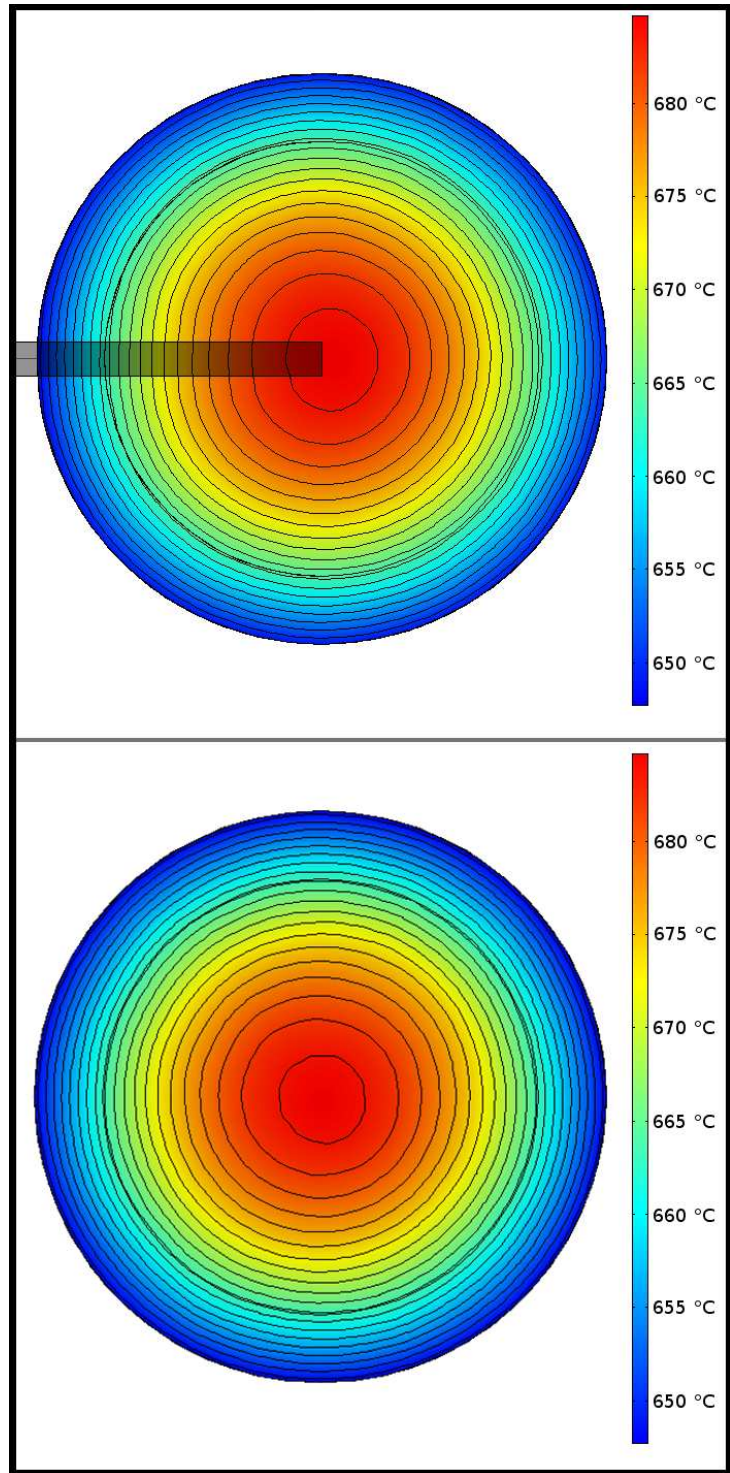


Figure B.3: Radial temperature distribution on the powder contacting surface of a SOD punch with (top) and without (bottom) the radial hole

The high temperature fidelity of the tungsten wires necessitated repairs to the SPS vacuum system. Maximum vacuum pressure was approximately 0.5 Pa during the study which increased the life from the expensive type-C tungsten wire. The sintering machine top ram feed through was reverse engineered and replacement components were produced in house. The seal (shown in figure B.4) maintains tight sliding contact with the steel ram and electrically isolates the electrode from the frame of the machine.

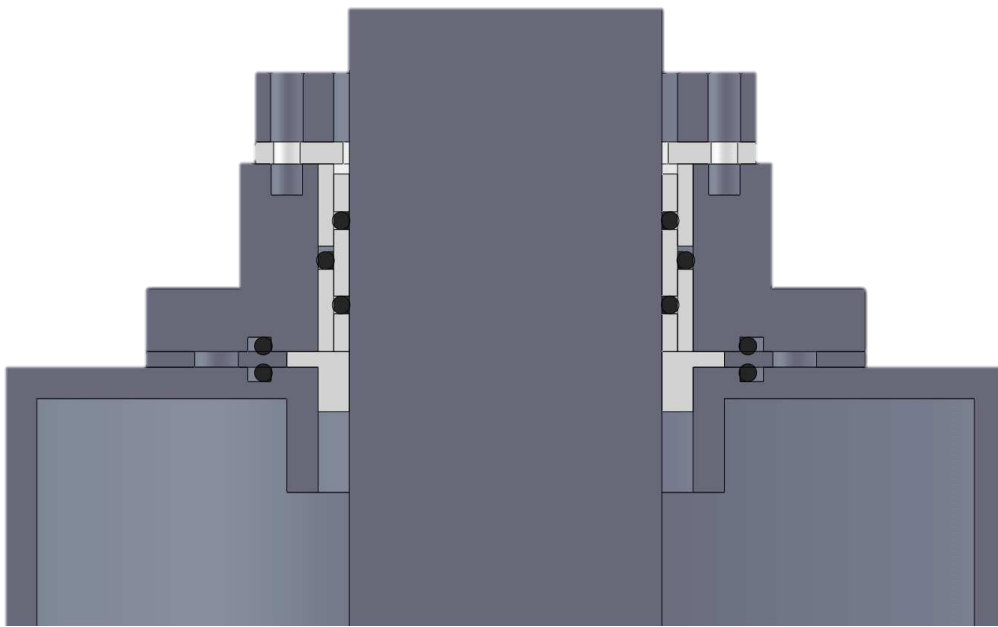


Figure B.4: Cross-section of top ram vacuum feed through. White components are Teflon, black circles are O-rings, gray is steel of the machine.

Appendix C

CEFAS design

C.1 CEFAS thermal modeling

Thermal models made from simplified CAD geometry were performed to gain insight into the heating characteristics. To simply model Joule heat the following assumptions are made:

- roller motion is ignored and all interfaces have perfect electrical and thermal contact
- Cooling by natural convection ($10W/m^2K$) and radiation to ambient $20^\circ C$
- No surface to surface radiation
- Extruded material uses fully dense material properties (over estimation of thermal and electrical conductivity)

The material between the rollers contacts the graphite along a 13mm arc length of the rollers over the 10mm width of the material. The copper electrode components are identical. The gray block on left hand side of the configuration bridges the circuit between the rollers and is modeled with copper material properties.

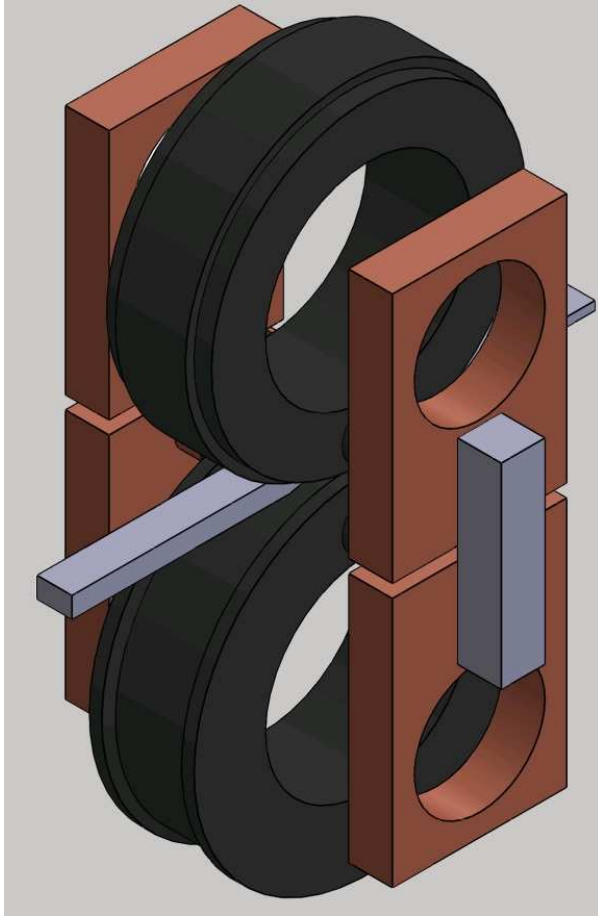


Figure C.1: CEFAS simplified CAD isometric view

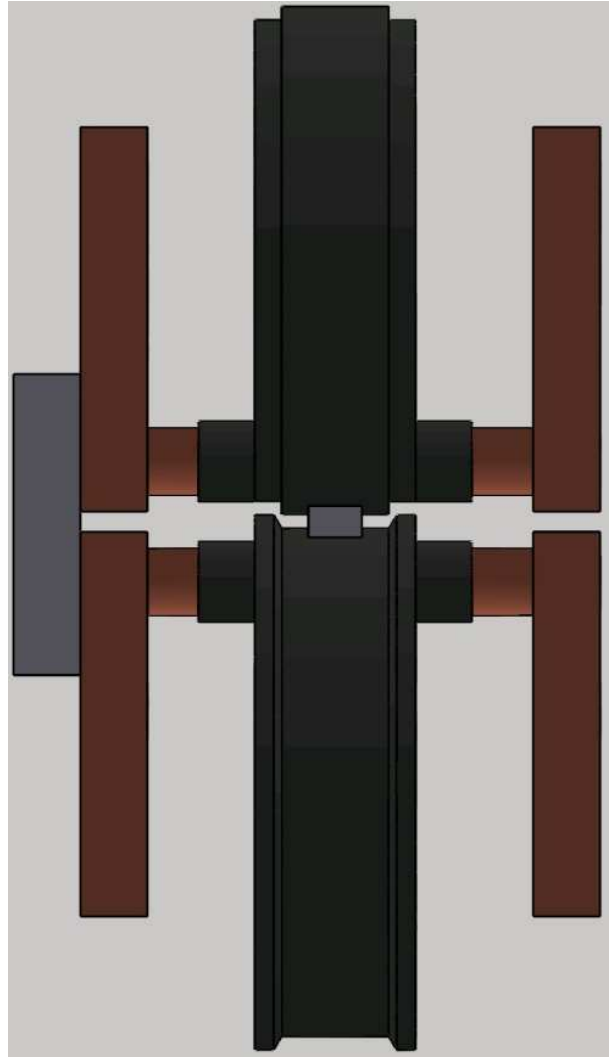


Figure C.2: simplified CAD model used for CEFAS thermal analysis

C.2 CEFAS design iterations

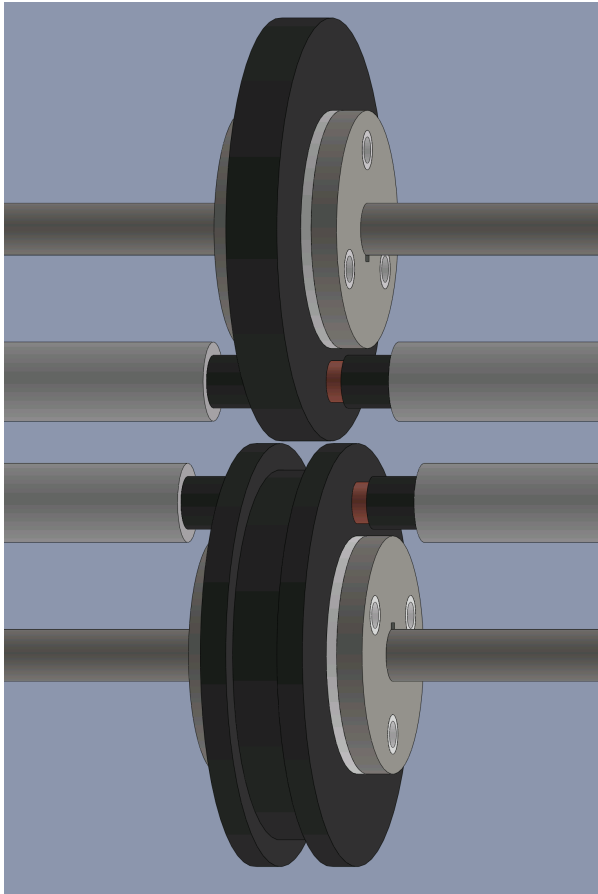


Figure C.3: CEFAS design v.1.II from June 6, 2016

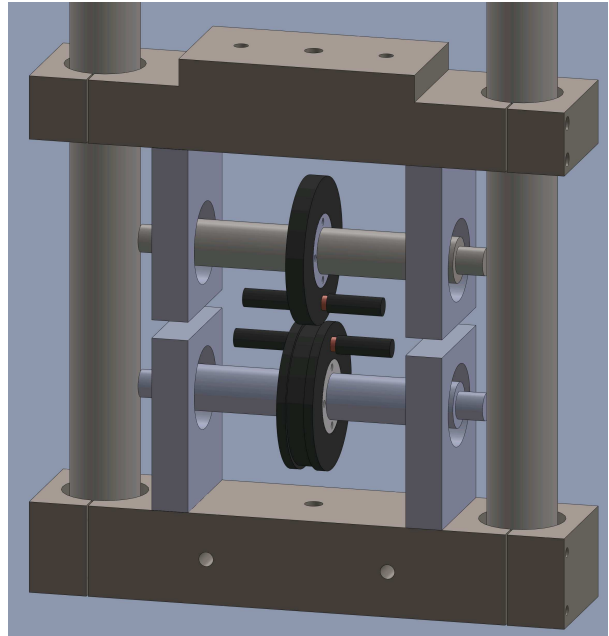


Figure C.4: CEFAS design v.1.III from June 12, 2016

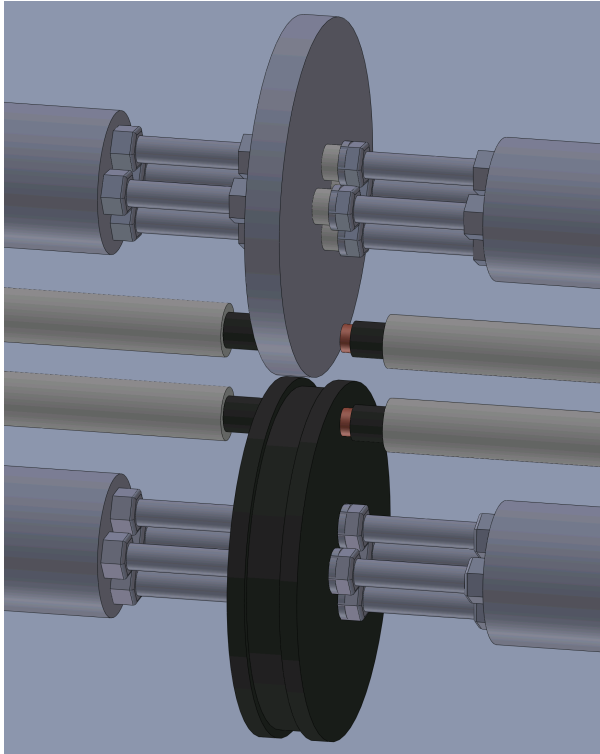


Figure C.5: CEFAS design v.2 from June 14, 2016

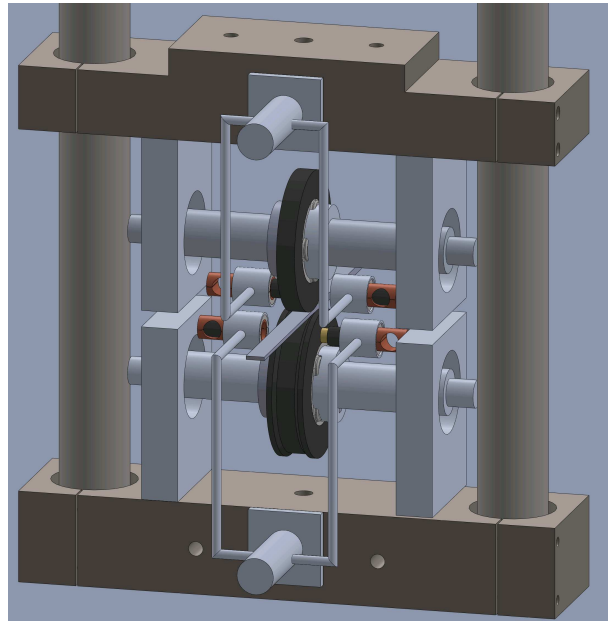


Figure C.6: CEFAS design v.5 from June 28, 2016

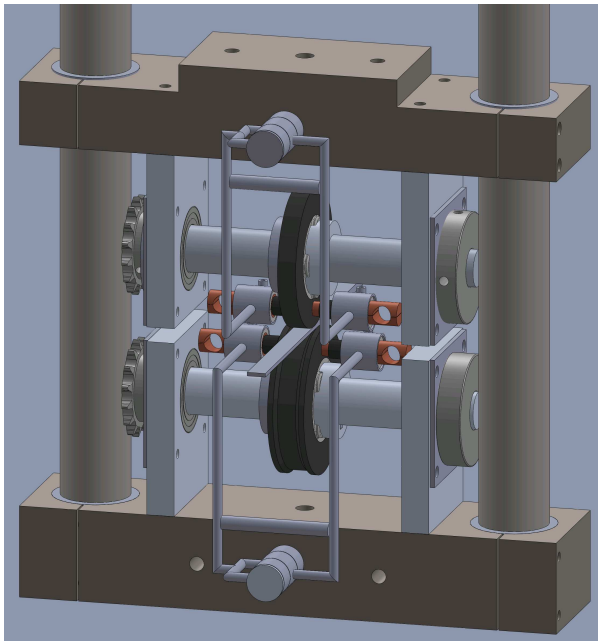


Figure C.7: CEFAS design v.8 from July 13, 2016

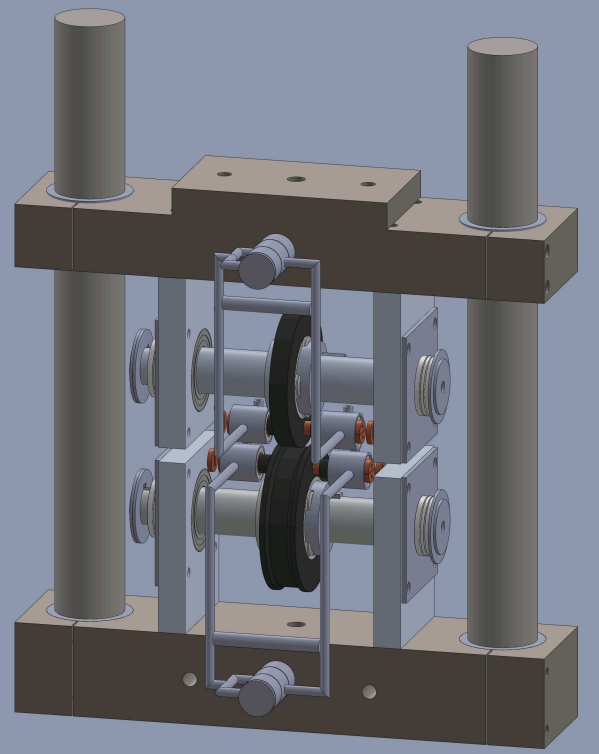


Figure C.8: CEFAS design v.9 from July 13, 2016

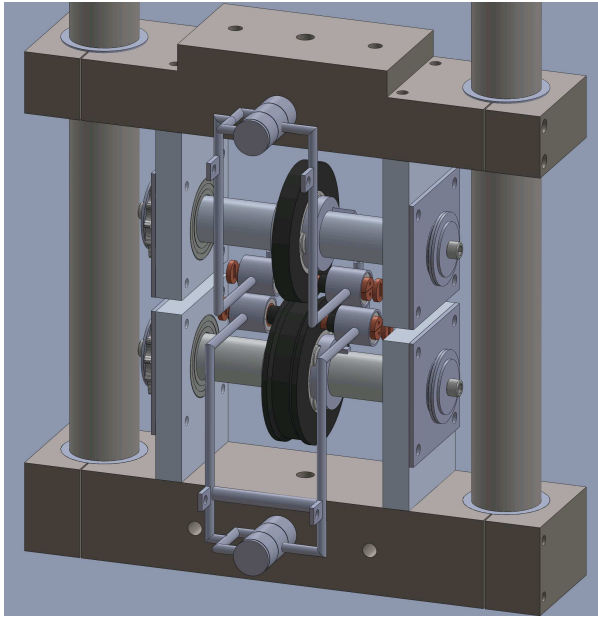


Figure C.9: CEFAS design v.10 from July 18, 2016

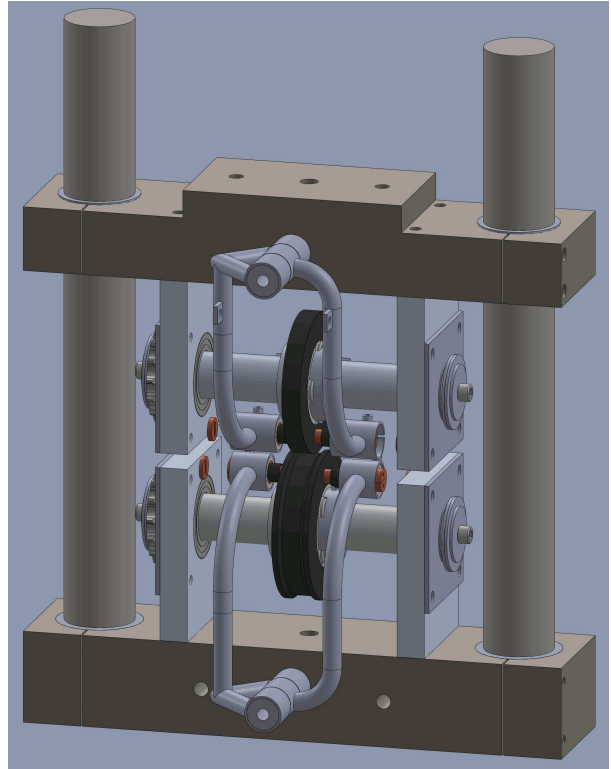


Figure C.10: CEFAS design v.16 from August 17, 2016

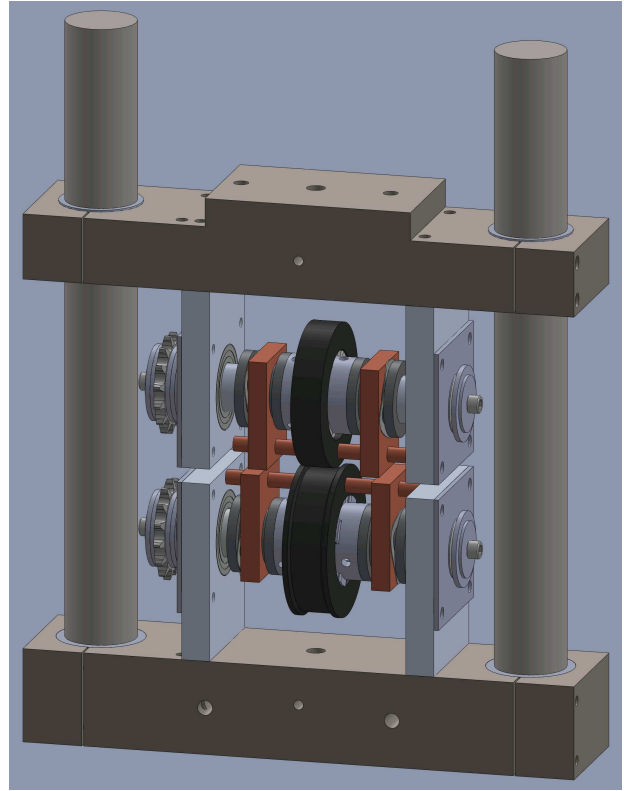
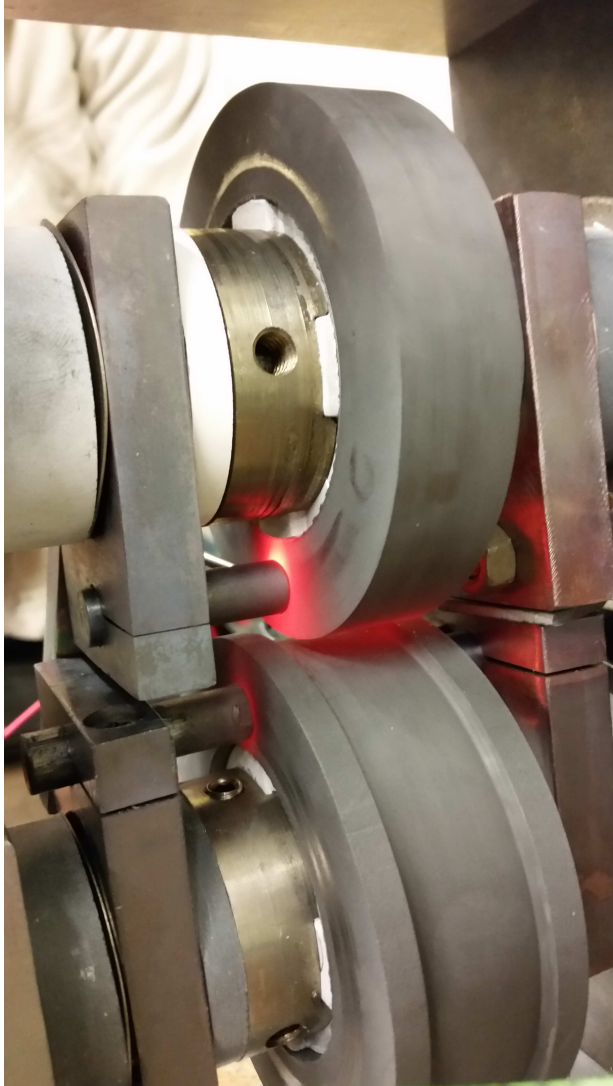


Figure C.11: CEFAS design v.21 from November 17, 2016

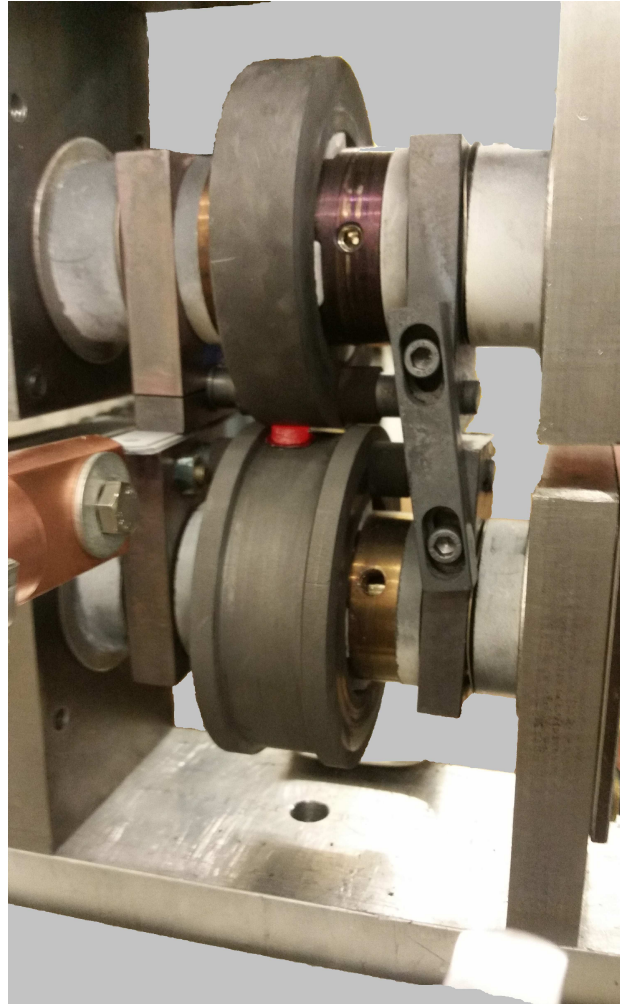
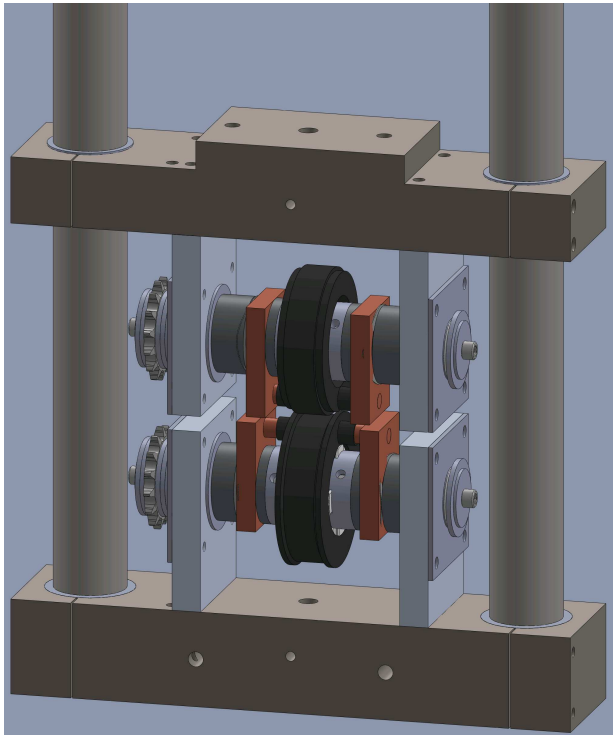


Figure C.12: CEFAS design v.25 from December 27, 2016